TÉCNICO LISBOA

Concurrent design study: Venus Atmosphere Sample Analysis mission

Girolamo Musso

Thesis to obtain the Master of Science Degree in Aerospace Engineering

Supervisors: Prof. Mário António Prazeres Lino da Silva
Prof. Lionel Marraffa

Examination Committee

Chairperson:	Prof. Fernando José Parracho Lau
Supervisor:	Prof. Mário António Prazeres Lino da Silva
Member of the Committee:	Prof. Duarte Manuel Salvador Freire Silva de Albuquerque

December 2022

Acknowledgements

First and foremost, I would like to thank my supervisors Lionel and Mario for all the help and support they provided me with during the development of this thesis with their wisdom and dedication.

I would like to thank as well the CDF team, without which nothing of this would have been possible: Hugo, Mariana, Yauanah, Marco and Vlad. A big thanks to the IPFN for believing in the project and providing everything was necessary for its realization.

To my family, ”Grazie di tutto” for all the affection and the help during this long journey. A special thanks to my brother.

To Costanza, thank you for your love and for always being there, supporting and guiding me in all the difficult moments along this path, always making me a better version of myself.

To Wendy Worrols, thank you for your friendship and closeness, despite the distance. A huge thanks to Haze, for all the adventures and moments we have shared together. To my friend Ginevra, for the support and affection you have always showed me.

Thanks to Niko, for having cheered up my study sessions.

Thank you to all the people, family, friends, and colleagues that contributed to my growth and made me the person I am today.

Abstract

Many unknowns are still present today to the most similar planet to ours in the Solar System: Venus. Although their similarities, the two planets present very different atmospheres, and it is still not clear why. Among the unknowns, many planetary evolution theories could be improved through the comparison between Venus and the other terrestrial planets, helping to create models for exoplanets. Noble gases can help investigate these theories, as they keep a trace of the planets' histories not reacting easily with other species or the surface. This however results in the impossibility of their detection by remote sensing from Earth or from a satellite, therefore making necessary their sampling. In order to assess the feasibility of a mission to collect and analyse a sample of noble gases, a mission concept involving an aerocapture manoeuvre with in-situ analysis has been proposed and studied in the Concurrent Design Facility "Laica". This thesis will cover the identification of the targets and their relative constraints, the trade-offs between various possible concepts, and the mission analysis. An interplanetary trajectory will be obtained through numerical implementation of theoretical inputs. The development of an atmospheric flights propagator ATP for the CDF will be illustrated, as well as its validation against NASA's software GMAT. Using engineering correlations and parametric studies a simplified design will be proposed.

Keywords: Venus atmospheric sample, Noble gases, Concurrent Design, Mission analysis, Trajectories

Resumo

Ainda existem muitas incógnitas sobre o planeta mais parecido com o nosso no Sistema Solar: Vénus. Mesmo com as suas semelhanças, as atmosferas dos dois planetas são muito diferentes e ainda não está claro o porquê. Entre as incógnitas, muitas teorias de evolução planetária poderiam ser melhoradas através da comparação entre Vénus e os outros planetas terráqueos, ajudando a criar modelos para exoplanetas. Os gases nobres podem ajudar a investigar estas teorias, uma vez que não reagem facilmente com outras espécies ou com a superfície, estes mantêm vestígios das histórias dos planetas. No entanto, isso os torna indetetáveis por sensores remotos na Terra ou em satélites, tornado assim necessário obter amostras físicas. De modo a avaliar a viabilidade de uma missão de recolha e análise de uma amostra de gases nobres, foi proposta e estudada uma missão conceptual que envolveu uma manobra de aerocaptura com análise in-sitiu na Concurrent Design Facility ”Laica”. Esta dissertação irá abranger a identificação dos alvos e os seus constrangimentos relativos, a análise de compromisso entre os vários conceitos possíveis, e a análise da missão. Uma trajetória interplanetária irá ser obtido através da implementação numérica dos dados teóricos. O desenvolvimento de um propagador de voos ATP para a CDF será ilustrado, bem como a sua validação com o software da **NASA!** GMAT. Utilizando correlações de engenharia e estudos paramétricos, será proposto um projeto simplificado.

Keywords: Amostra atmosférica de Vênus, Gases nobres, Engenharia concorrente, Análise de missão, Trajetórias

Contents

List of Tables

List of Figures

Acronyms

AOCS	Attitude and Orbit Control System
ATP	Atmospheric Trajectories propagator
AU	Astronomical Unit
CDF	Concurrent Design Facility
D/H	Deuterium/Hydrogen
DC	Differential Corrector
DoF	Degrees of Freedom
DSMC	Direct Simulation Monte Carlo
GCMs	Global Circulation Models
GMAT	General Mission Analysis Tool
IPFN	Institute for Plasmas and Nuclear Fusion
IST	Instituto Superior Técnico
JGM-2	Joint Gravity Model 2
JPL	Jet Propulsion Lab
LoS	Line of Sight
NASA	National Aeronautics and Space Administration
QITMS	Quadruple Ion Trap Mass Spectrometer
RK	Runge-Kutta
SoI	Sphere of Influence
SQP	Sequential Quadratic Programming
SZA	Solar Zenith Angle
ToF	Time of flight
TPS	Thermal Protection System
UA	Unknown Absorber

List of Symbols

Latin letters

C_D	Drag coefficient	[]
C_L	Lift coefficient	[]
G	Universal Gravitational constant	[m^3/kg s^2]
HL	Heat load	[kJ/m^2]
J	Julian epoch	[]
J_2	Second order gravitational correction term	[]
L_c	Characteristic length	[m]
M or m	mass	[kg]
MF	Mass fraction	[%]
R	Base radius	[m]
R_a	Apoapsis distance	[km]
R_{eqB}	Body's equatorial radius	[km]
R_{extra}	Extra distance for shadow projection	[km]
R_i	Rotation matrix around the i axis	[]
R_s	Skirt radius	[m]
Ra	Ratio R over r_n	[]
S	Reference surface	[m^2]
SoI_p	Planet's Sphere of Influence	[km]
T	Orbital period	[s]
V	Volume	[m^3]
V_{BF}	Back-face Volume	[m^3]
X_n	Dependent variable	[]
a	Orbit's semi-major axis	[km]
acc	Acceleration	[g]
e	Orbit's eccentricity	[]
h	Time step	[s]
h_c	Spherical cap height	[m]
i	Orbit's inclination	[°]

q	Orbit's periapsis distance	[km]
$\dot{q_c}$	Convective heat flux	[kW/m^2]
$\dot{q_r}$	Radiative heat flux	[kW/m^2]
r_b	Back radius	[m]
r_n	Nose radius	[m]
r_p	Radius of the parking orbit	[km]
r_{sh}	Shadow projected radius	[km]
t	TPS Thickness	[m]
t_b	Back-face TPS Thickness	[m]
t_h	Hohmann transfer's Time of flight	[s]
t_s	Skirt TPS Thickness	[m]
v	Velocity	[km/s]
v_∞	Asymptote velocity	[km/s]
v_0	Entry velocity	[km/s]
v_a	Apoapsis velocity	[km/s]
v_N	Impulse's perpendicular component	[km/s]
v_p	Periapsis velocity	[km/s]
v_{rot}	Tangential atmosphere velocity	[km/s]
v_V	Impulse's longitudinal component	[km/s]

Greek letters

ΔV	Impulse	[km/s]
ΔV_{pl}	Hohmann's impulse planar component	[km/s]
ΔV_z	Hohmann's impulse vertical component	[km/s]
Ω	Orbit's longitude of the ascending node	[°]
α_h	Hohmann transfer's angle	[°]
β	Ballistic coefficient	[kg/m^2]
β_{pc}	Angle for patched conic approximation	[°]
β_{pl}	Extra angle for patched conic approximation	[°]
γ	Flight path angle	[°]
δ	Plane change angle	[°]
ϵ	Tolerance	[]
θ	Orbit's true anomaly	[°]
θ_b	Back angle	[°]
θ_{pl}	Angle difference of Hohmann's transfer impulse	[°]
θ_{SC}	Sphere-cone angle	[°]
θ_{ij}	Position/velocity vector's angle on the ij plane	[°]
λ	Latitude	[°]
μ	Gravitational parameter	[km^2/s^3]
ρ	Density	[kg/m^3]
ρ_{SC}	Spacecraft density	[kg/m^3]
ρ_{TPS}	TPS density	[kg/m^3]
ω	Orbit's argument of periapsis	[°]
ω_{rot}	Angular velocity	[rad/s]

Chapter 1

Introduction

Venus, Earth's evil sister, has always fascinated humans and, among them, the scientists as well. However, our knowledge of the nearest and most similar planet in size and mass to ours is actually poor, and many unknowns are still present today.

Indeed, although the similarities between the planets, one has oceans of liquid water and hosts a multitude of life forms, while the other is often described as a hellscape. And it is still not clear why.

Nowadays, it is more or less known how the solar system has formed and which are the main steps that brought the small particles around our proto-Sun to become the planets we know today, however a lot of uncertainties are present on the various mechanisms going on during these steps, and their influence on the evolution of the planets.

Since its beginning, space exploration has helped the scientific community to answer many of these questions and, in particular, the exploration of extraterrestrial planets has been extremely useful to understand the histories of evolution of the single bodies and of the solar system itself.

Venus' exploration has however always been making engineers' life difficult, due to the harsh environment it presents but, as engineers love challenges, it became the first planet to be explored, both from orbit, with Mariner 2 flyby, and from the surface, with Venera 7.

Indeed, the Venera program of USSR provided, during the years, a huge quantity of information on the planet, that allowed to understand better the complex atmosphere surrounding the planet and responsible for the climate near the surface. However after the end of the program, just orbiters or flybys were sent to the planet unable, given their nature and the particularities of the atmosphere, to provide comprehensive information.

In order to answer most of the questions left unanswered, samples of the atmosphere and their analysis with modern instruments are needed, justifying the focus of this work on a preliminary study of a mission to Venus' atmosphere in order to collect samples to be analysed in-situ or back to Earth through the Venus Atmospheric Sample Analysis mission VASA.

The mission design will be conducted in a Concurrent Design Facility (CDF), through concurrent engineering methods. More specifically, this thesis will describe the first steps of the process, as to say the identification of the targets and their relative constraints, and the mission analysis, with a system-

focused approach.

A literature review on the current knowledge on the planet's atmosphere and planets' evolution in wide terms has been done in order to understand which are the most relevant questions nowadays and how they could be answered; this process has led to the identification of some targets as objectives of the sample collection: of course the different targets will be located at different altitudes, thus leading to different possible mission concepts.

The objective of the study will be to assess the generic feasibility of the mission trying to reduce risks and complexity: preliminary trade-offs have been conducted in this optic, leading to the choice of a direct aerocapture manoeuvre with in-situ analysis of the samples.

The general design of the spacecraft and of the mission will be the result of the concurrent design process, and will not therefore be reported here.

The first step for the definition of a planetary mission is the interplanetary trajectory, that has been obtained through a theoretical method based on the Hohmann transfer and the patched conic approximation, and through the numerical propagation of the theoretical trajectory on NASA General Mission Analysis Tool.

In the frame of developing tools for the CDF, a numerical propagator for atmospheric flights has been developed during the study: the ATP code, to aid in the preliminary phases of the design as parametric studies and to take into account several design aspects related to the trajectory propagation as the shape optimization or the thermal design of the probe.

The code has been validated against GMAT in order to verify the correct implementation of the equations and to assess the expected degree of accuracy.

It has been then used, coupled with engineering correlations, to derive relations specific to this design to help manage the key parameters and their relations through a systemic view of the design where every subsystem interact with each other.

Setting several arbitrary constraints some design choices have been investigated leading to the derivation of a hypothetical design that would allow for an aerocapture manoeuvre able to collect the samples at the right altitude, and with good margins on the entry corridor.

Chapter 2

Literature Review

As in Larson J. W. (1999), the first step of a space mission analysis and design process is the definition of the objectives, the starting point to derive requirements and constraints that will help to broadly characterize the mission concept and identify drivers for each system.

This chapter will therefore offer an overview of the current knowledge regarding Venus' atmosphere and the possible ways to assess its unknowns, leading to a baseline for a proper concurrent design process, identifying sampling targets and mission concepts to collect and analyse them, comparing their advantages and problematics.

2.1 Atmospheric characteristics

Venus, the second rocky planet from the Sun, gained the epithet of Earth's 'sister planet' due to its similarity in size and mass with our planet (0.82 M_e and 0.95 r_e), its position near the Earth (0.72 Astronomical Unit (AU)) and some analogies between the conditions present today on the planet and the ones of the early Earth (Ghail et al., 2019).

In spite of these analogies, the two planets evolved in a very different way: Venus' atmosphere is dominated by CO_2 (96.5% by volume) and N_2 (3.5%), with smaller amounts of noble gases (He, Ne, Ar, Kr, Xe) and chemically reactive trace gases (SO_2, H_2O, CO, OCS, H_2S, HCl, SO, HF, and elemental sulphur vapour) (Fegley, 2004), that results in an extreme greenhouse effect, leading to an average surface temperature of 464 ℃. The dense atmosphere also results in a surface pressure of $\sim$ 93 bar (Ghail et al., 2019).

A global opaque cloud layer covers the surface from the sunlight at visible wavelengths and vertically extends from $\sim$ 47.5 to $\sim$ 70 km, composed mainly by liquid sulphuric acid (H_2SO_4) and water (Titov et al., 2018). High values of Deuterium/Hydrogen (D/H) ratio were found, suggesting a possible loss of atmospheric water. Highly variable atmospheric conditions are present through this layer that also comprises a possible habitable zone (Ghail et al., 2019).

Among the most recent discoveries regarding Venus' atmosphere there are: evidences for polar vortices, confirmation of lightnings, evidence of recent volcanic activity and discovery of large gravity

waves at the cloud-top level. Venus does not present a planetary magnetic field (Ghail et al., 2019).

2.2 Planets' evolution hypotheses

Immediately, a question arises: why the two planets, so similar, and in the same zone of the solar system, evolved in such a different way? To understand it, the state of the art of the theories regarding planets' formation and their early evolution will be presented.

2.2.1 Protoplanets' formation

The prevailing theory upon planets' formation is the so-called solar nebula disk model: the solar system formed from a gaseous cloud where the Sun, who formed before the planets, flattened the remaining gas into a disk, called "nebula disk", "protoplanetary disk", "solar disk", etc (Woolfson, 1993).

Of course, the solids available for planet formation were not the same at every position of the disk: only the solids whose melting/sublimation temperatures were above the local temperature could exist as solids (Grossman and Larimer 1974, as cited in Izidoro and Raymond 2018). The disk however kept cooling in time, therefore the locations of condensation fronts were constantly moving inward (Martin and Livio 2012, and others as cited in Izidoro and Raymond 2018). Iron and silicates were abundant in the inner regions of the disk, while the outer regions were rich in ice and other volatiles (Lodders 2003, as cited in Izidoro and Raymond 2018).

It is generally accepted that collisional growth of micrometer-sized dust grains is efficient to form pebbles up to mm to cm range in regions of protoplanetary disk dense enough (Izidoro and Raymond, 2018). The next phase, that sees the mm-to-cm bodies becoming planetesimals with radii between 1 and 1000 km is still not totally explained. The so called 'bouncing barrier' limits, at this scale, the efficiency of the collisional mechanism: the bodies might now bounce off of each other instead of growing (Zsom et al. 2010; Birnstiel et al. 2011; Testi et al. 2014, as cited in Izidoro and Raymond 2018).

Although growing collisions may still occur according to the sizes and velocities of the bodies, another problem arises: due to the velocity of the disk's gas, bodies of this size will suffer a tremendous drag force that would make them fall into the Sun very quickly. A 1 meter size object at 1 AU in a typical disk falls toward the star in 100 years (Weidenschilling 1977, as cited in Izidoro and Raymond 2018). A gas drag assisted mechanism, called "streaming instability", that could explain the transition to planetesimals through mechanisms of concentration of material in certain regions has been modelled and is still object of study (Izidoro and Raymond, 2018).

Once formed, planetesimals' mutual gravity starts now to play an important role and has to be taken into account. They now grow by collision between each other or accreting the remaining grains in the disk: three different regimes are present (Izidoro and Raymond, 2018).

In the so-called "Runaway growth" regime, larger planetesimals grow faster than smaller ones accreting them and thus forming the first planetary embryos, large enough to not be affected by the gas drag. (Kokubo and Ida 1996; Ormel et al. 2010b, as cited in Izidoro and Raymond 2018).

The embryos gravitational perturbations start to dominate, modifying the velocities of the planetesimals: the "Oligarchic growth" regime begins (Tanaka and Ida 1997, as cited in Izidoro and Raymond 2018) creating a bimodal population of embryos and planetesimals where the first ones still grow slightly faster of the second ones.

Lastly, when the embryos reach a mass $\sim$ 100 times the planetesimals ones, the "Orderly growth" regime begins. In this stage the growth is roughly the same for both embryos and planetesimals and the collisions between them become the predominant mechanism. The gas disk has probably now dissipated, and the system evolves chaotically with collisions, scattering, and ejection of planetesimals and embryos until the population of planetesimals decreases drastically and just few large embryos remain (Izidoro and Raymond, 2018).

The late stage of accretion to proto-planets is still uncertain and a current problem in the description of our Solar system's evolution. Three main models exist and among them the most accepted one is the so-called "Grand Tack" scenario, according to which Jupiter's inward-then-outward phase of migration had a key role in the evolution of the terrestrial planet region. It is able to solve many of the problems of the classic theories as the formation of Mars and asteroid belt in agreement with observations, albeit leading to criticisms that require further studies (Izidoro and Raymond, 2018).

After the solar nebula stage, two processes could still produce chemical compositional changes: collisional erosion and post-nebula volatilization (Lammer et al., 2018). The latter affects "moderately volatile elements", as the radiogenic Potassium (^{40}K). Collisional erosion is caused by large impactors such as that which was involved in the Moon-forming event and could add the three heat-producing elements (Th, U and K) (O'Neill and Palme 2008; Campbell and O'Neill 2012; Jellinek and Jackson 2015; O'Brien et al. 2017 as cited in Lammer et al. 2018) and alter the metal-silicate ratio of the protoplanets (Bonsor et al. 2014; Carter et al. 2015, as cited in Lammer et al. 2018).

2.2.2 H/He envelope

If the protoplanets accreted most of their final mass within the solar nebula, they would have then captured a thin H/He envelope from the disk's gases trapping as well primordial noble gases (Owen et al., 2020).

However, while "local" studies suggest that the protoplanets captured just a thin atmosphere while growing, afterwards lost, the direct observations of exoplanets have shown the opposite. This however should not be possible due to the impossibility, given the size of the resulting captured envelope, to get rid of it (Owen et al., 2020).

This problem might not exist and could be given by biases in the exoplanets data analysis and in the models used, able to characterize well just exoplanets around Mercury's orbits and in system with Sun-like stars; those questions will be hopefully answered by the data collected by PLATO mission (Owen et al., 2020).

A phenomenon associated with such atmosphere and in general present in the initial stages of the solar system is the hydrodynamic escape: through this process light gases as Hydrogen or Helium that

escape the atmosphere overcoming the planet's gravity field due to their lightness might drag through viscous forces even heavier elements (Albarede et al., 2011).

2.2.3 Steam atmosphere

Whether this envelope was present or not, a critical stage that led to the modern atmospheres was the so-called "steam atmosphere" or "outgassed atmosphere" (note that the word steam is used even though water is not the main component).

The energy released by the decay of short-lived radiogenic isotopes, as the ones cited before, present in the protoplanets' inventory, the gravitational potential and the powerful impacts between the bodies can create magma ponds or oceans on the protoplanets (Lammer et al., 2018).

While solidifying, magma oceans tend to undergo compositional fractionation. In particular, volatile elements that are incompatible in mantle minerals being created, are delivered to the liquid phase that becomes more and more enriched in them until their respective solubility is reached. If such occurs, they are outgassed (Elkins-Tanton 2008; Lebrun et al. 2013; Salvador et al. 2017, as cited in Lammer et al. 2018).

The presence of this atmosphere and its composition controls itself the lifetime of the magma oceans, due to the greenhouse effect that might exert on the surface, delaying therefore the solidification. A magma ocean that simply cool radiating heat into space would complete its solidification in a few thousand years (Monteux et al. 2016, as cited in Lammer et al. 2018) however, if such an atmosphere is present, the situation could be very different and depends on the radial distance from the Sun. Water vapour outgassed from a magma ocean would condense in $\sim$ 0.1 Myr at 1.5 AU on Mars, in $\sim$ 1 Myr at 1 AU on Earth and in $\sim$ 10 Myr or even longer at 0.7 AU on Venus, whose orbit is too close to the Sun to allow the steam atmosphere's condensation (Hamano et al. 2013; Lebrun et al. 2013; Massol et al. 2016; Salvador et al. 2017, as cited in Lammer et al. 2018).

Venus' position is indeed close to a critical value below which magma oceans could stay liquid for even 100 Myr, time during which the water would be dissociated by Sun's radiation and escape to space through hydrodynamic escape (Lammer et al., 2018). In this scenario, water oceans may have formed on the early Earth and Mars after condensation of outgassed water present in their volatile inventory. This is in agreement with oxygen-isotope evidence indicating presence of liquid water as early as 4.3-4.4 Gyr ago (Mojzsis et al. 2001; Wilde et al. 2001, as cited in Lammer et al. 2018).

2.3 "Moist" Venus hypothesis

Moreover, the hypothesis of an initial "wet" Venus, with an H_2O inventory close to the present Earth's one, is not totally accepted and present some uncertainties.

An initial "dry" Venus is indeed predicted by the equilibrium condensation model, that uses plausible values of temperatures and pressures within the solar nebula to understand the chemical composition of the gas in function of the radial distance (Lewis and Prinn 1984; Kerridge and Matthews 1988, as cited

in Fegley 2004).

According to the model hydrous minerals were unstable where Venus formed, but stable where Earth formed, leading to a "wet" Earth; however the accretion zones for Venus and the Earth present significant overlapping zones and therefore a real separation of their accretion zones should not be possible making the two water inventories at least similar (Weidenschilling 1976, as cited in Fegley 2004). Another argument regards the impossibly slow formation of these minerals at the temperatures necessary for them to be thermodynamically stable in the gas disk (Fegley 2000, as cited in Fegley 2004).

Considering the scenario of Venus dessicating under greenhouse effect maintaining liquid its magma oceans, the hydrodynamic escape cited before could remove $\sim$ 470 m of water from Venus in 100 Myr and produce the elevated D/H ratio observed on Venus today through decomposition of water and hydrogen loss to space with a flux of $\sim 10^{12}$ H/cm^{2}s (Donahue et al. 1997, as cited in Fegley 2004).

However, one must consider that Sun's visible radiation was 25-30% smaller than the present one in the considered period, thus the greenhouse effect might have started some time after. Considering that current Venus' hydrogen loss rate is $\sim 10^7$ H/cm^{2}s, that Sun's UV radiation, contrarily to the visible spectrum, was higher in the past and has decreased in time (Micela, 2002) and that hydrogen loss through non-thermal processes is $\sim$ 100 times slower, an initially "moist" Venus may be more likely than an initially "wet" Venus (Fegley, 2004).

Beside the hydrogen loss' problem, also huge amounts of O_2 should be left after losing such a big ocean. For instance, considering the loss of 2.7 km of water from Venus, equivalent to Earth's oceans, $\sim 1.1 \cdot 10^{21}$ kg of O_2 would be produced that, considering modern Venus' atmosphere, should have been disposed (Fegley, 2004).

Considering current oxygen loss rates to space, $\sim$ 30% of that amount should be left in water. On Earth, 96% of all O_2 produced over time was consumed through oxidation of reduced carbon, iron, and sulphur. Carbon oxidation happened on Venus probably during impact devolatilization, leaving iron and sulphur as the only possible sinks (Fegley, 2004).

Removing all this O_2 through these chemical reactions requires an incredible exposure of lithosphere to the atmosphere and therefore an eruption rate of $\sim$ 140 km^3/yr; current Earth's volcanism rate is $\sim$ 20 km^3/yr, and the estimated rate on Venus is 1 km^3/yr. Again, the possibility of a "moist" Venus is indeed more plausible than a "wet" scenario (Fegley, 2004).

A recent study proposed however the resurfacing events that have taken place in the last 1000 Myr on Venus as viable O_2 sinks, thus possibly solving this problem (Way et al., 2020).

2.4 Volatiles' loss and late accretion

After this outgassing stage, H_2O molecules in the upper atmosphere will be dissociated and H_2 molecules and H atoms, that will be the most abundant species, will efficiently hydrodynamically escape dragging with them heavier volatiles making the atmosphere of the protoplanets less volatile rich while growing. This stage's escape is nowadays supported by many studies (Watson et al. 1981; Chassefiére 1996a, 1996b; Tian et al. 2005; Lammer et al. 2013, 2014; Erkaev et al. 2013, 2014; Odert et al. 2018,

as cited in Lammer et al. 2018) and it is thought that a loss of $\sim$ 40% of the steam atmosphere of the protoplanets occurred during their growth (Hin et al. 2017, as cited in Lammer et al. 2018).

What happened next, that brought the proto-planets to their final mass is still not very well explained and many theories and events have been proposed to explain different questions, the main scenarios are: late veneer, late accretion and late heavy bombardment. However, the same names are often used to explain different processes and even in different periods. The first one should describe the delivery of chondritic material during the planet's growth, the second one is instead related to the accretion after the last giant impact while the third one is used to describe a probable period of heavy bombardments after the Moon's formation, however it is often used to describe a bigger phase including as well the late accretion (Morbidelli and Wood, 2015).

The H_2O dissociation would not of course happen in the outer solar system due to the much smaller Sun's radiation and, in agreement with planetary dynamics model based on the "Grand Tack" theory and meteorites observations, it is now expected that volatile-rich carbonaceous chondritic bodies travelled from the outer into the inner Solar System during the protoplanets' accretion phase, hitting directly the growing terrestrial protoplanets and that most volatiles, including a few Earth oceans, could have been delivered through collisions (Lammer et al., 2018).

The heavier non-radiogenic noble gases in Venus' atmosphere are not so different from their primordial stages and hydrodynamic escape models can reproduce the observed Venus ^{20}Ne/^{22}Ne and ^{36}Ar/^{38}Ar isotope ratios, considering that proto-Venus grew to a mass greater than 0.6 M_e inside the gas disk, thus capturing a solar-like noble gas rich H_2-envelope. Combined H_2-envelope mixed with outgassed steam atmosphere scenarios manage to reproduce the observed ratios. These scenarios are also in agreement with the "Grand Tack" hypothesis (Cameron 1983; Pepin 1991, 1997; Odert et al. 2018, as cited in Lammer et al. 2018).

However, on Earth the atmospheric isotope ratios represent solar rates that are modified by a contribution from carbonaceous chondritic material although direct observations (Dixon et al. 2000; Porcelli et al. 2001; Yokochi and Marty 2004, 2006, as cited in Lammer et al. 2018) based on ^{20}Ne/^{22}Ne fractionations showed how remnants of the solar nebula are still present in the mantle, thus supporting the theory of the capture of a thin H_2-envelope by the proto-Earth (Lammer et al., 2018). This is also in agreement with the so-called U-Xe composition found on Earth (Pepin 2000, as cited in Lammer et al. 2018).

As said before the volatiles' delivery, although considered realistic, is not well characterized in terms of delivered mass and its origins: simulations based on the "Grand Tack" showed how the delivery of water and other volatiles should be nearly the same for Venus and Earth (Marov and Ipatov, 2018), while Jacobson et al. (2017) argue that Venus might have avoided large impacts at the end of its accretion as the hypothetical Moon-forming event. Moreover, Gillmann et al. (2016) analysed the effects of different possible impact histories on Venus reaching the conclusion that the period and dimensions of the impactors play a very important role into the long-term consequences and showed how a sufficiently big impact during the late veneer might have even removed water from the planet through atmosphere volatilization.

It is now clear how Venusian atmospheric samples might have several implications on these research

fields and help in the understanding of planetary formation and early evolutionary processes, allowing to discriminate between the theories (Baines et al., 2013).

2.5 Open questions about present atmosphere

Beside the interest in planetary formation and atmosphere evolution, many other scientific questions are still open regarding Venus' atmosphere.

2.5.1 Dynamics

One of the open questions regarding Venus is why the planet rotates so slowly and why its atmosphere rotates 40 to 60 times faster than it: the so-called superrotation. This phenomenon is also present on Jupiter, Saturn, Saturn's moon Titan and some exoplanets; it might be present, with a very low magnitude, in the Earth's upper atmosphere, although modern studies' results showed how it should not and suggest the reanalysis of past data (Gaposchkin, 2003).

Many Global Circulation Models (GCMs) have been developed during the last decades to describe the atmosphere dynamics on Venus, however with a lot of discrepancies with empirical data. The most recent models are able to solve many of the past problems and to develop and maintain the superrotation through a balance of the angular momentum transport between thermal tides and gravity waves from the interaction of the atmosphere with the topography; however the respective roles of each term, as well as the importance of small-scale waves have to be assessed yet (Imamura et al., 2020).

The comparison with Titan is indeed interesting in the study of this phenomenon due to the extreme differences between the two bodies. Thermal tides, appearing to play a central role in Venusian models, are instead not relevant for Titan's atmosphere. A common feature to the two atmospheres is instead the absorption of solar radiation within the atmosphere and not near the surface, not been proved yet to be crucial in the superrotation description, although it is known that atmospheric circulation is driven by radiation's absorption (Imamura et al., 2020).

A complete understanding of the various phenomena related to angular momentum transport and of the role of solar radiation absorption could help Earth's GCMs and could provide better models for future explorations (Imamura et al., 2020).

Indeed, one of the unknowns of Venus' atmosphere is the so-called Unknown Absorber (UA): a chemical species that efficiently absorbs solar radiation, with maximum at a wavelength of 340 nm, decreasing at lower wavelengths where it overlaps with the absorption of SO_2 (Lee et al., 2021). It could be poly-sulphur (S_2, S_3, S_4), iron chloride, or various other possibilities (Wilson et al., 2021). It is responsible for $\sim$ 50% of the total solar heating at cloud top level, and its increment by a factor of 2 during the last decade has been observed. This could affect of course the thermal tides cited before and therefore the superrotation of the atmosphere, justifying long-term variations observed in the winds (Lee, Jessup, et al. 2019, as cited in Lee et al. 2021).

The vertical distribution of the UA is poorly constrained and even a recent study on Akatsuki's data

was unable to constrain it better, concluding how it might exist both within all the upper layer of clouds or confined in a thin layer; the study however found out that sufficient absorption must be present within the 4 km immediately below the cloud top (Lee et al., 2021).

Moreover, this leads to further problems in the wind characterization being the UA the main way to measure wind velocities. Indeed, most of the knowledge upon Venus' winds is derived by tracking cloud movements in different wavelengths to see the contrast between different cloud elements. However on the night side their motion is derived by the differences in thermal emission or, in the polar regions, as excess of emission with respect to the background, therefore with different wavelengths resulting in observations at different altitudes: global averages of the wind fields cannot be obtained with these methods (Sánchez-Lavega et al., 2017).

Lastly, the role of the polar vortices, present at both poles and characterized by low altitude clouds and high temperatures, on the superrotation has to be assessed yet (Sánchez-Lavega et al., 2017).

2.5.2 Chemistry

The atmosphere of Venus has many complex chemistry processes that control its enormous and particular atmosphere; three major cycles have been identified: the carbon dioxide cycle, the sulphur oxidation and the poly-sulphur one. The first two have been observed directly, while the third one is still speculative (Marcq et al., 2019).

The carbon dioxide cycle includes CO_2 dissociation in CO and O and its transport to the night side with subsequent production of O_2 and combination of CO and O in CO_2 through chlorine catalysed pathways, however the standard models fail to explain how CO_2 is stabilized over geologic time, predicting abundances even an order of magnitude greater than the observed upper limits (Marcq et al., 2019).

Some models had speculated, based on the observations of HCl in the upper atmosphere, that a ClO_x based catalysis is able to stabilize the CO_2, however no chlorine radicals had ever been observed in the past. The recent observation of ClO in the upper atmosphere gave the first empirical confirmation of those models that still require further studies and the direct identification of other species as ClC(O)OO or ClCO (Sandor and Todd Clancy, 2018).

The sulphur oxidation cycle is for sure the most important cycle, it comprises the upward transport of OCS, SO_2, and H_2O, and the oxidation to H_2SO_4, that condensate to form the cloud layers and the sulphuric acid droplets; the poly-sulphur cycle involves the upward transport of OCS and SO_2 and the downward transport of S_x (x $=$ 2-8) (Marcq et al., 2019).

The main unknowns regarding the sulphur cycle are: the standard models' prediction of an abundance of SO_2 and the complete depletion of water vapour, although observations has shown how SO_2 is depleted in the clouds and above them, while H_2O is still present above the clouds, and the inversion layer present in the vertical profile of SO_2 that might imply the presence of another sulphur reservoir yet unidentified. Observations suggest that the complex dynamics of the atmosphere might play a role in the inversion layer, but this hypothesis requires further studies (Vandaele et al., 2017).

The abundances of SO_2 and H_2O still represent a "puzzle for which there is no successful solution

in the literature consistent with observations" that implies either possible wrong observations in the abundances of those species in the lower atmosphere, or the existence of unknown processes based as well on unknown chemicals (Rimmer et al., 2021).

A possible pathway is the one based on NH_3, a base that, if present within the right abundance, could perfectly solve the problem depleting the SO_2 and, at the same time, allowing the presence of H_2O above the clouds. This model is based on the attempt of observation of NH_3 by Venera 8 that however has been discounted along the years due to the related inconsistencies with the processes supposed in the atmosphere at the time, confuted by the authors that also propose a biological origin of the ammonia (Bains et al., 2021a). The possible habitability of the clouds and the possible presence of phosphine will be discussed further on in section 2.5.3.

The hypothesis of wrong observations is however understandable, considering the ignorance on the detailed composition of the clouds and hazes. Indeed, the major species can be studied from orbit, but many minor species can not. The thick absorbing atmosphere makes impossible the use of remote sensing to detect the many minor species that as discussed might play important catalytic or intermediate roles in the major cycles. Moreover, all the previous falling descent probes had time to analyse just small numbers of samples, leading to poor knowledge on the clouds layer and, even more, on the sub-cloud hazes and on the near-surface part of the atmosphere (Wilson et al., 2021).

2.5.3 Habitability and phosphine debate

The poisonous atmosphere of CO_2, the extreme temperatures and pressures and the corrosive amounts of sulphuric acid make Venus actually not suitable for life on its surface, therefore making its study helpful to understand better Earth-sized exoplanet and their possible habitability.

There is however a range of altitudes in the atmosphere that might host some life forms present on the Earth, called habitable zone.

At altitudes comprised between 48 km and 62 km the temperature varies between 100 °C, temperature of evaporation of liquid water, and -20 °C, limits for the cell growth (Patel et al., 2022). At an altitude of 51 km (65 °C) extremophiles known on the Earth could survive the combination of high temperatures and acidity (Dartnell et al., 2015).

At an altitude slightly above 50 km the pressure is equal to the Earth's one (1 bar), and decrease to $\sim$ 0.1 bar at 60 km (Landis, 2003).

Studies have shown how the absence of a planetary magnetic field might however not be a problem for life thanks to the absorption of radiations by the thick cloud layer. More specifically: the direct ionizing radiation flux from cosmic rays or extreme solar particle events are unlikely to be a treat to the possible Venusian life even at the top of the habitable zone (Dartnell et al., 2015); the UV radiation penetration is though greater and might limit this zone: at an altitude of 59 km the radiation environment is less intense than the one of the Archean Earth while at an altitude of 54 km the radiations reach levels lower than the present Earth's surface ones (Patel et al., 2022).

A possible biosignature of such life forms could have already been detected with the apparent pres-

ence of phosphine (PH_3) gas with peaks of $\sim$ 20 parts-per-billion (ppb) and a planetary average of $\sim$ 7 ppb in Venus' atmosphere, where any phosphorus should be in oxidized forms (Greaves et al., 2020b).

According to the study, the presence of phosphine is unexplained through steady-state chemistry or photochemical pathways, leading to no currently-known abiotic production routes in Venus' atmosphere, clouds, surface and subsurface, or from lightning, volcanic or meteoritic delivery. It could however originate from unknown photochemistry or geochemistry (Greaves et al., 2020b).

By analogy with biological production of phosphine on Earth, thus the hypothesis of life as phosphine's source has been proposed (Greaves et al., 2020b).

The temperate but hyper-acidic Venusian clouds have been proposed for decades as potentially habitable, because biological production of phosphine is favoured by cool, acid conditions and because initial modelling based on terrestrial biochemistry suggested that biochemical reduction of phosphate to phosphine is thermodynamically feasible under Venus cloud conditions (Greaves et al., 2020b).

Villanueva et al. (2021) debated how the same results could be obtained by a reasonable presence of sulphur dioxide (SO_2) and, even considering PH_3 to be the source, it should have been present at an altitude greater than 75 km to be detected through the means used by (Greaves et al., 2020b), concluding that the phosphine detection on Venus was not supported.

A reanalysis of the data by Greaves et al. followed this work, and concluded how SO_2 could not explain the features present in the data even if present in amounts not suitable for the Venusian environment and how the altitude was not a real limitation to the phosphine's presence (Greaves et al., 2020a).

However, the new calibration of the data showed localized abundance to peak at $\sim$ 5-10 ppb, with suggestions of spatial variation. Advanced data-products suggest a planet-averaged PH_3 abundance of $\sim$ 1-4 ppb (Greaves et al., 2020a). Independent PH_3 measurements suggest as well a possible altitude dependence: under $\sim$ 5 ppb at 60+ km, up to $\sim$ 100 ppb at 50+ km (Greaves et al., 2020a).

On the other hand, at the same time, other studies focused on possible different abiotic paths to phosphine. Considering the much more different environment on Venus in respect to Earth, the same volcanic rate producing 1–5 ppb of phosphine in Venusian atmosphere could only generate about 0.6–30 ppq of phosphine on Earth, where the lowest concentration usually detected in the atmosphere is $\sim$ 10 ppq.

According to the authors, if the phosphine is present, it might point to a modestly elevated plume volcanism activity with magma originating deep in the mantle (Bains et al., 2021b).

2.6 Sampling Targets

The previous section gave an insight of the current unknowns regarding Venus' atmosphere and the possible implications deriving by the study of its samples on many scientific areas.

Noble gases are of extreme importance in the study of the evolution of planets and atmospheres because they do not react with the surface or other gases, keeping a trace of cataclysms such as impacts or interior degassing, thus leaving a trace of the planets' histories (Baines et al., 2013).

However, this ability to resist to chemical interactions, creates a problem in terms of their identification, because it results as well in a very weak coupling to electromagnetic radiation, therefore not providing them of a strong spectral feature making thus impossible to detect them through remote sensing methods: only in-situ sampling can measure their abundances (Baines et al., 2013).

More specifically, the interest of the scientists fell over the Xenon and its isotopes, never measured precisely on Venus. According to Baines et al. (2013) a precision of at least 5% (even $\sim$3% to discriminate better) on the measurements is needed to discriminate among different scenarios that take into account the various volatiles-related mechanisms cited before such as: trapping of solar nebula noble gases in the mantle and its subsequent degassing, hydrodynamic escape, impact erosion, delivery from comets or icy planetesimals, etc. (Baines et al., 2013).

As well as Xenon, also the Krypton measurements are not precise enough and differ by more than one order of magnitude. The ratio Ar/Kr that derives from these measurements stands indeed in a range too wide to allow for discrimination between the various hypothesis: the higher estimate resembles Jupiter's atmosphere and the solar wind leading to the hypothesis of a large impact with a cold comet, while the lower one resembles the Earth, Mars, and some meteorites, strengthening the hypothesis of accretion from the solar nebula during the protoplanets' formation (Baines et al., 2013).

Moreover, also the isotopes of Ne and O can be used to investigate the evolution of the planets. It is believed that Ne escaped from Earth leaving just its heavier isotopes, creating the low Ne/Ar ratios observed on Earth and Mars, not recognized anywhere else in the Solar System (Baines et al., 2013). However, its lighter isotopes are still present in our atmosphere and the measurement of their ratios on Venus and its comparison with Earth's ratios could help understand whether the protoplanets accreted them from the same reservoir or not (Baines et al., 2013).

The same process can be applied to O isotopes, as has been done for the Earth and the Moon, that share the same isotopic composition, inconsistent with all the observed composition of any observed meteorites (Baines et al., 2013).

Regarding Ne, isotopic ratios with an accuracy of at least 5% are needed to discriminate between early evolution models. For O instead, the required accuracy is 0.02% for the $^{17}O/^{16}O$ ratio (Baines et al., 2013).

Venus' homopause, the limit below which the atmosphere gases are well mixed, is in the literature in the range 124-134 km (Mahieux et al., 2012) or 120–132 km for CO_2, most abundant species in the atmosphere (de Pater and Lissauer, 2001 as cited in Gruchola et al. 2019).

According to Nikolić et al. (2019) two scaling laws can be derived for day side and night side, giving very different scale heights between each other. Using the equations of the article, applied to all the noble gases and using the densities of Justh et al. (2021), the minimum found homopause levels were: 113 km for the day side and 101 km for the night side.

As discussed in section 2.5.3 the possible habitable zone is set between 48 and 62 km optimistically, while a range comprised between 51 and 54 km is indeed more realistic and can be set as well as altitude target for phosphine detection after the reanalysis made by Greaves et al. (2020a) that enlightened a vertical distribution of PH_3 with the highest concentrations around 50 km.

Another possible target may also be set to the upper layer of the clouds to obtain a precise evaluation of the clouds' composition and the chemistry processes happening within them; the UA could also potentially be identified within the 4 km below the cloud top, set to 70 km.

Three main targets can be defined in terms of altitude for the mission :

Table 2.1: Targets and altitudes.

Target	Altitude (km)
Noble gases (day)	$<$113
Noble gases (night)	$<$101
Cloud composition and chemistry	66-70
Phosphine and habitable zone (wide)	51-62
Phosphine and habitable zone (precise)	51-54

2.7 Sampling process and trade-offs

Once the targets have been established, some concerns regarding the sampling process and the analysis of the collected samples have to be considered to guarantee a proper scientific value of the sample and thus justify the mission.

First, one must consider the state of the collected sample and its representative value in regard to the real atmosphere composition.

An atmospheric entry is characterized by hypersonic speeds and related high enthalpy flows, where complex thermodynamic and transport processes happen, as ionization and dissociation (Rabinovitch et al., 2019b). This might result in alterations of the sample relative to the atmosphere, and therefore in biases during the samples' analysis, in case the sample is collected through an atmospheric passage.

Moreover, the heat fluxes that result from the atmospheric drag during the reentry may require the adoption of an ablative Thermal Protection System (TPS). Such a shield will start to ablate, thus injecting external species in the flow that might contaminate the sample. In that case the recombination of the dissociated atmospheric species with the shield's material must be considered; in case the species of interest cannot recombine with the ablate material, then just the dilution of the original mixture has to be taken into account.

Regarding the analysis, the samples might be returned to Earth, where much more powerful instruments are available, or can be analysed in-situ.

In case the analysis has to be performed on Earth, then several aspects must be considered. The first one is to exit the planet's atmosphere, not relevant in case of a single passage but important in case of a balloon or a descent capsule. Then the return transfer has to be performed, therefore enough propellant must be stored and a Thermal Protection System for the terrestrial reentry has to be designed. Lastly, the sample conditions must be preserved during the reentry and the landing location prediction must be accurate enough to allow for the samples' recovery.

A simpler solution could be the in-situ analysis: given the possibility to carry an instrument that is able to perform the desired analysis with the required precision, the only additional constraints would be on the time to carry on the analysis, relevant in case of a balloon or a descent capsule, and on the data transfer to Earth.

Lastly, a mixed approach could be useful to investigate all the altitudes and to solve some problems listed above: one can imagine a main capsule skimming the atmosphere and sampling it at the higher altitudes while sending a descent capsule or a balloon deeper inside the atmosphere. If the trajectory is such that the major capsule is captured by the planet and starts orbiting around it, then it could serve as a relay satellite between the inner capsule and the Earth or could recover the samples to be brought back to Earth.

A first trade-off has been made between an Earth return capsule and an in-situ analysis: if the required precision for the samples' analysis can be granted by an onboard instrument, then the Earth's return would add just complexity, mass, risks, and costs.

For both cases, three options have been identified for the sampling: an entry capsule, a floating balloon or an atmospheric skimming.

An entry capsule would allow for the sampling of all parts of the atmosphere however an in-situ analysis would be limited by the descent time and the communication with Earth would require a relay satellite; in case of a sample return a rocket would be needed to exit the atmosphere and a return capsule should intercept it to return back to Earth.

A floating balloon could reach the habitable zone sampling it in a subsonic regime and allowing for the measurement of winds, however for the sample return the same problem of exiting the atmosphere would arise. Regarding the in-situ analysis, much more time would be available compared with the descent capsule, but a relay satellite might be needed anyway.

Lastly, an atmospheric skimmer would be limited to the upper part of the atmosphere but would allow for a simpler sample return and would have plenty of time to analyse in-situ the samples: the major risks would be related to the manoeuvre itself and to the hypersonic sampling. The atmospheric passage could be done from a spacecraft already orbiting the planet or directly from the interplanetary trajectory through an aerocapture manoeuvre.

Of course, the mixed approach could investigate all the options, but the complexity would be huge.

As the noble gases have been identified as a very important target and would allow for the simplest concept that is the atmospheric passage with in-situ analysis, they have been chosen as candidate targets for this study and a more precise investigation on their analyses and required precision has been carried out.

A possible payload configuration for the in-situ analysis is proposed in (Nikolić et al., 2019): an inlet valve is opened below the homopause, connected to an inlet capillary tube to collect the sample, getter pumps clean it and a miniaturized Quadruple Ion Trap Mass Spectrometer (QITMS) analyses it, granting the required precision and resolution.

As the precision of the analysis is based on the partial pressure of each noble gas inside the holding tank a simplified approach is proposed assuming every minor species is dissolved in CO_2 to simulate the

flow inside the capillary tube and therefore to quantify the amount of sample entering the tank in a given time, helping to dimension the inlet tube's length and diameter, as well as the tank volume. Moreover, to have a clean sample the getter pumps must not saturate. A more detailed list of the required precision can be found in (Chassefière et al., 2012) and the payload can therefore be dimensioned to ensure them.

The problematics of hypersonic sampling are detailed in the works of Rabinovitch et al. (2019b, 2019a) whose scope is to develop a numerical simulation able to model the sampling phase of a National Aeronautics and Space Administration (NASA) proposed mission concept called "Cupid's Arrow" whose objective is to sample the upper atmosphere of Venus to measure noble gases' abundances and their isotopic ratios. It should be achieved, according to their design, through a single passage at an altitude comprised between 100 and 110 km where the capsule will capture a sample at the stagnation point to be analysed in-situ with a miniaturized QITMS, a similar concept to the one chosen for this study.

The author used the Direct Simulation Monte Carlo (DSMC) method to simulate numerically the transport of the various species at the aforementioned altitude with a velocity of $\sim$ 10.5 km/s. The study is still at an early phase and just few species have been considered so far; moreover, sensitivity studies on the influence of the ratio of simulated to real molecules are being performed to minimize the numerical errors of the model.

As in Rabinovitch et al. (2019a): 'preliminary results show that there is no significant fractionation for Xe or Ar isotopes, the total ratio of Ar to Xe does change from the Venus atmosphere to the sampling tanks. The tank is enriched in Ar and Xe relative to the amount in Venus atmosphere. The enrichment is larger for Xe that is denser... The isotopes ratios are much less affected.'. Although the model is still under study and presents some numerical errors, it shows the feasibility to simulate numerically the sampling process and thus the possibility to create a transfer function able to link the composition of the sample to the one of the real atmosphere.

If one uses an ablative TPS without traces of noble gases, then its ablated material will not alter the noble gas ratios; the dilution of the samples however should be taken into account as the getter pumps could now saturate and let major species inside the QITMS, thus invalidating the analysis' results. As in the "Cupid's Arrow" concept the capsule's nose could be covered with a ceramic TPS to avoid contamination, however dynamic studies of the trajectory should be needed to ensure the stagnation point is always inside the ceramic nose.

The selected concept is therefore to perform an aerocapture manoeuvre directly from the interplanetary trajectory with a periapsis lower than the homopause level, to collect a sample of noble gases that will be then cleaned of all the major species and analysed through a miniaturized QITMS while orbiting the planet after the atmospheric passage; the collected data will be then sent back to Earth by the same spacecraft. It is assumed that the hypersonic sampling and the dilution of the ablated material can be quantified to dimension the payload with margins to ensure the required precision for scientific purposes and that a full ablative TPS can be used.

Chapter 3

Materials and Methods

This chapter will present the methodologies used along the development of the thesis and the mathematical formulations behind the development of the tools used to obtain the results reported in the next chapter.

3.1 Concurrent Design Facility CDF

This study has been conducted in a CDF following the ideas of concurrent engineering. Its approach is based on five key elements (Bandecchi et al.):

- An iterative process starting with the identification of the mission requirements, constraints, drivers, and outline of the basic mission concept, followed by a number of sessions in which the team builds together the design, exchanging ideas and collectively taking choices to take into account several aspects of the design at the same time.
- A multidisciplinary team where each member has an attributed discipline, providing the team with deep knowledge on it and helping to have different opinions on the interactions between the subsystems. A team leader is present to help coordinate the various members.
- An integrated design model, based on key parameters that are available to every member of the team using them as inputs for their discipline, deriving output parameters to be updated on the model in an iterative process.
- A facility where the specialists can meet and easily exchange ideas and interact between each other.
- A software infrastructure with tools to generate and update the model (COMET CDP4 (COMET, 2018)), a set of tools for each discipline and a document support and storage system to exchange and save bibliography, documents, and other useful files.

A new Concurrent Design Facility ”Laica” has been newly implemented at Instituto Superior Técnico this year and the mission VASA has been used as an example study mission using the CDF infrastucture.

It allowed to develop useful knowledge and software to be used for the facility, serving as proof for the feasibility of developing analogous studies in the facility (Lino da Silva et al., 2022).

This thesis focuses on the first steps of the process, namely, the identification of the targets and constraints, derived between the team leader and the customer, and the Mission Analysis. The team participating in the CDF was composed of five members, whose main disciplines were: System, Thermal and Power, Command and Data Handling, Telecommunications, Mission Analysis/Trajectories and Aerothermodynamics. All the other disciplines were divided equally among the team.

The scientific justification of the mission, given in the previous chapter, represented the first part of the process and helped to outline the basic concept of the mission and the major design choices.

Mission analysis is the main focus of the thesis and involved the derivation of the interplanetary trajectory, and the simulation of atmospheric flights, that required the development of a specific tool. A series of analyses and parametric studies provided elements to support and guide the preliminary phases of the design, keeping a systemic view of the spacecraft.

Further in this section, the theoretical basis used to derive the interplanetary trajectory and to develop the Atmospheric Trajectories propagator code will be reported.

3.2 Reference frames and Euler angles

To provide a clearer idea of the concept presented below, a small introduction on reference frames and Euler angles must be given.

A distinction should be done between fixed and inertial reference frames.

In an inertial reference frame, the axes are fixed, and the planet is rotating with its atmosphere: therefore a body on the surface rotates with the planet and has a non-null velocity thus, to compute drag, heat fluxes and so on, the velocity relative to the atmosphere (null at the ground) must be used. In inertial reference frames, Newton's laws of motion are valid in their original form.

In a fixed reference frame, the central body is fixed with respect to the coordinates axes, however, the whole system is rotating. Although the velocity in this reference frame is the one relative to the atmosphere, to apply Newton's laws one should take into account fictitious force due to the rotating axes (Curtis, 2008).

The reference frames used in this work are inertial, more specifically, the $BodyInertial$ system of GMAT is defined with the z-axis aligned with the axis of rotation of the planet, the x-axis pointing along the line formed by the intersection of the planet's equator and earth's mean equator at J2000 and the y-axis completing the right-handed set (GMAT, 2020).

Although the latitude is computed in the same way as it is on the Earth since the z-axis is coincident with the rotation axis and the xy-plane is coincident with the equator, a quick note should be done on the longitude: the used reference frame is inertial thus the coordinates of the point having null longitude will vary with the epoch, rotating with a period equal to the duration of a Venusian day. Outputting from GMAT the longitude of a point with coordinates $[R_v, 0, 0]$ at different epochs, the following expression can be obtained:

$$Lon_{x=0} = 1.48136879977861 \cdot (J - 21896.16133722298) - 2n\pi \qquad \text{n = 1, 2, 3...} \qquad (3.1)$$

where J is the Julian epoch.

Lastly, note that in the way the reference frame is created, the longitude will increase with a positive angle measured as in Figure 3.2.

The state of a body in a reference frame is defined through the so-called state vector, in which the first three elements are the $[x, y, z]$ coordinates and the last three are the velocity components $[v_x, v_y, v_z]$.

It is convenient to introduce the notion of Euler angles: according to Euler's rotation theorem, every rotation can be described using three rotations. One can describe the rotations around each axis by the rotation matrices below (Curtis, 2008):

$$R_x(\alpha_x) = \begin{bmatrix} 1 & 0 & 0 \\ 0 & cos(\alpha_x) & sin(\alpha_x) \\ 0 & -sin(\alpha_x) & cos(\alpha_x) \end{bmatrix} \qquad (3.2)$$

$$R_y(\alpha_y) = \begin{bmatrix} cos(\alpha_y) & 0 & sin(\alpha_y) \\ 0 & 1 & 0 \\ -sin(\alpha_y) & 0 & cos(\alpha_y) \end{bmatrix} \qquad (3.3)$$

$$R_z(\alpha_z) = \begin{bmatrix} cos(\alpha_z) & sin(\alpha_z) & 0 \\ -sin(\alpha_z) & cos(\alpha_z) & 0 \\ 0 & 0 & 1 \end{bmatrix} \qquad (3.4)$$

Twelve possible sequences of rotation axes exist to perform the three rotations, and it is a matter of the used convention. In Figure 3.1, the order $z - y' - z''$ is used (Curtis, 2008).

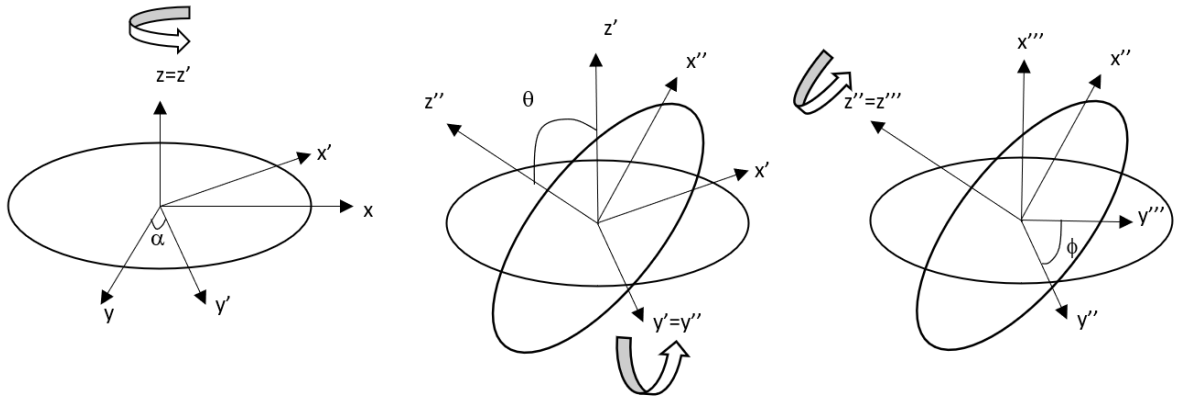

Figure 3.1: Example of a full rotation using Euler's angles through the order $z - y' - z''$.

One of the most important parameters in atmospheric flights is the flight path angle γ: it can be defined as the angle between the velocity vector and the plane perpendicular to the position vector

(Curtis, 2008), however it might seem complicated to identify and modify it in a three-dimensional space. Using the notions presented above, it will be easy to understand Figure 3.2:

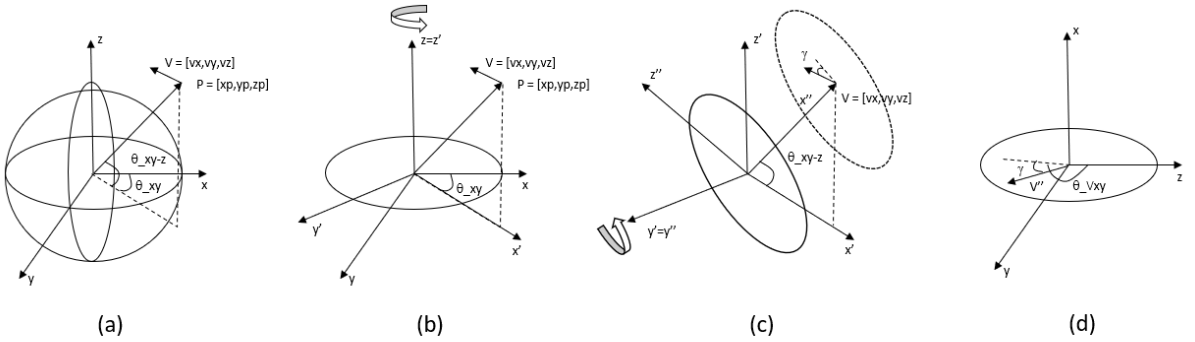

Figure 3.2: Flight path angle determination using Euler's angles.

Although three rotations are needed to completely orient a body in space, if one wants to target a point with one of the axes, just two rotations are needed. A point with coordinates $[x, y, z]$ can be described by two angles (a):

$$\theta_{xy} = arctan(\frac{y}{x}) \tag{3.5a}$$

$$\theta_{xy-z} = arctan(\frac{z}{\sqrt{x^2 + y^2}}) \tag{3.5b}$$

Rotating around the z-axis of θ_{xy} (b) and then around y' of θ_{xy-z} (c), the point will be on the x"-axis, now coincident with the position vector, thus making γ the angle between v and the plane containing the y and z-axes (d).

Applying the opposite rotations to the vector v, minding the direction of the rotations and the way the angles are computed, the vector v'' will be obtained: looking at the xy-plane the angle θ_{xy} is computed clockwise, while the rotation around the z-axis is counterclockwise; the angle θ_{xy-z} is instead computed counterclockwise, as the rotation around the y' axis. Therefore, to apply the opposite rotations, one can write:

$$\begin{bmatrix} v''_x \\ v''_y \\ v''_z \end{bmatrix}_{3D} = \begin{bmatrix} v_x \\ v_y \\ v_z \end{bmatrix}_{2D} \cdot R_z(\theta_{xy}) \cdot R_y(-\theta_{xy-z}) \tag{3.6}$$

At this point, in the same way described above, the two angle θ_{vxy} and $\theta_{vxy-z} = \gamma$ can be computed with respect to the new coordinate system (d) in Figure 3.2. The angle γ is comprised between 0 and -90° for entry trajectories (it is positive for a climbing aircraft), while θ_{vxy} is comprised between 0 and 360°: it is 0 on the positive z-axis (increasing latitude), $\frac{\pi}{2}$ on the positive y-axis (increasing longitude) and so on.

Again, to modify the two angles, the same rotations can be applied in the new reference frame. Note

that, if such modifications are done, to obtain the vector in the original reference frame, the applied rotations must be done again with the opposite angles and in the opposite order, as to say, from the last applied one to the first one.

3.3 Interplanetary trajectory

The interplanetary trajectory has been determined in two steps: an analytic calculation of the trajectory through the approximation of a Hohmann transfer first and a patched conic approximation then. The obtained outputs have been used in the General Mission Analysis Tool of NASA to numerically solve the equations of motion with a high grade of accuracy.

The ephemeris of the planets have been obtained from the Horizon system of the Jet Propulsion Lab (JPL) (Horizon, 2022) and a third-party code GEGOUT (2022) has been used to download them in the form of Keplerian elements of the two orbits in a heliocentric reference frame. The system lets the user choose the initial day and hour, the number of subsequent days and the step size.

In the absence of constraints on the departure dates, the next ten years have been investigated with a time step of one day.

The downloaded Keplerian elements were: e, q, i, ω, Ω, θ and T, the first five terms are needed to completely determine the orbit, the sixth is needed to know the position at a given time and the seventh is redundant as it could have been determined from the previous ones.

The semi-major axis a has been determined and the position and velocity on the ecliptic plane have been obtained through (Curtis, 2008):

$$a = \frac{q}{1-e} \tag{3.7a}$$

$$[x, y, z]_{2D} = \frac{a(1-e^2)}{1 + e \cdot cos(\theta)}[cos(\theta), sin(\theta), 0] \tag{3.7b}$$

$$[v_x, v_y, v_z]_{2D} = \sqrt{\frac{\mu}{a(1-e^2)}}[-sin(\theta), e + cos(\theta), 0] \tag{3.7c}$$

The gravitational parameters of the two planets are reported in Table 3.2. Lastly, the following relations can be applied using the rotation matrices described in the previous section:

$$\begin{bmatrix} x \\ y \\ z \end{bmatrix}_{3D} = \begin{bmatrix} x \\ y \\ z \end{bmatrix}_{2D} \cdot R_z(-\Omega) \cdot R_x(-i) \cdot R_z(-\omega) \tag{3.8a}$$

$$\begin{bmatrix} v_x \\ v_y \\ v_z \end{bmatrix}_{3D} = \begin{bmatrix} v_x \\ v_y \\ v_z \end{bmatrix}_{2D} \cdot R_z(-\Omega) \cdot R_x(-i) \cdot R_z(-\omega) \tag{3.8b}$$

Through the exact position of the planets, the angles on the ecliptic plane can be computed at any time.

3.3.1 Hohmann transfer

In a first approximation the Hohmann transfer theory has been applied considering two circular coplanar orbits for the two planets, and the Sun as central body. The mass of the two planets and of the spacecraft have been considered null.

To intercept the second body, whose period will be longer or shorter depending on its proximity to the Sun, this transfer requires a precise angle α_h between the planets at the departure date:

$$t_h = \pi \sqrt{\frac{(r_1 + r_2)^3}{8\mu}} \tag{3.9a}$$

$$\alpha_h = \pi - \omega_{rot2} t_h \tag{3.9b}$$

Where r_i are the radii of the orbits, and μ is the gravitational parameter of the central body, in this case the Sun (Table 3.2) (Curtis, 2008); ω_{rot} is the angular velocity. The subscript 1 is referring to the starting body and 2 to the ending body. The angular velocity can be computed as:

$$\omega_{rot} = \frac{\sqrt{\frac{\mu}{r_i}}}{r_i} \tag{3.10}$$

Once the angle α_h has been determined one can find, within the selected time interval, the days in which the two bodies will make that angle on the plane and therefore find a possible launch window.

Moreover, Lambert's problem can be solved to determine an orbit between two points around a central body within a given Time of flight (ToF) giving as outputs initial and final velocities on the transfer orbit (Curtis, 2008).

Finally, knowing the velocities of the bodies and the velocities of the transfer orbit, the needed impulses can be computed as the difference between the two.

3.3.2 Three-dimensional orbits

When considering the real orbits, two problems arise: the non-circularity and the non-coplanarity.

The non-circularity of the orbits is easily taken into account when the Lambert's problem is solved for the real positions (on the ecliptic plane) of the bodies, however of course the values computed before for circular orbits will not be the optimal values any more.

To find the minimum value of ΔV for the transfer, to compare the possible launch windows, the days before and after the found departure date can be investigated, as well as ToF slightly greater or lower than the theoretical value.

Lambert's problem has been solved multiple times with different departure dates and for each of them different ToF, searching for the minimum ΔV.

The non-coplanarity of the orbits must instead be accounted for in terms of plane change: an impulse performed right before the first one and perpendicular to it, to place the trajectory in the plane containing the second body at the selected arrival time.

A composite impulse can be done as in the (a) of Figure 3.3: in this case, the formula to compute the ΔV is (Curtis, 2008):

$$\Delta V = \sqrt{v_1^2 + v_2^2 - 2v_1 v_2 cos(\delta)} \tag{3.11}$$

where v_1 is the planet's velocity, v_2 is the velocity needed to enter the transfer orbit on the plane, obtained from the solution of the Lambert's problem, and δ is the required angle of plane change (Curtis, 2008).

However, as can be seen in the picture, this is valid just in the case where the initial velocity and the required velocity are aligned, valid just for the theoretical Hohmann transfer, and for sure not valid within the range of days and ToF selected.

In this case, as can be seen in (b) the insertion velocity will make an angle θ_{pl} with the planet's velocity: to compute the total ΔV one must compute first what is called ΔV_{pl} in (c).

This can be easily obtained applying Equation 3.11 between v_1, $v_2 cos(\delta)$ and with angle θ_{pl}. The Pythagorean theorem can be then applied to the obtained value and the other component of the insertion velocity: $v_2 sin(\delta)$, thus obtaining the total ΔV.

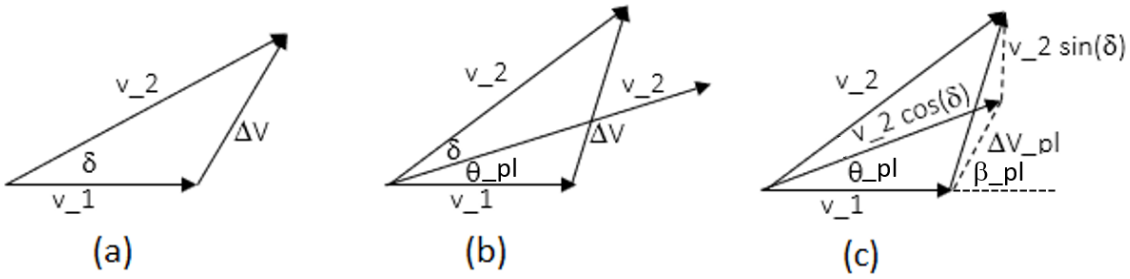

Figure 3.3: Vector compositions for plane change

3.3.3 Patched conic approximation

This method is used in order to take into account the gravity of the three bodies. The overall transfer is divided in three parts: the first one inside the Sphere of Influence (SoI) of the Earth, considered as the only body exerting a gravitational force on the spacecraft, the second one where the influence of the Sun is stronger than the ones of the other bodies, and the last one, inside the SoI of Venus. The used radii of the SoI come from (Curtis, 2008) and are: SoI_e 925000 km and SoI_v 616000 km.

Just the first part of the transfer will be accounted in this way, as its outputs will be implemented in GMAT to propagate the trajectory with much more precision.

To apply this method, a circular parking orbit must be defined around the initial body: it was arbitrarily set to r_p 15000 km from the Earth's centre. The real transfer however may be carried out using the last stage of the launcher, and therefore more precise calculations considering the selected launcher capabilities will be needed.

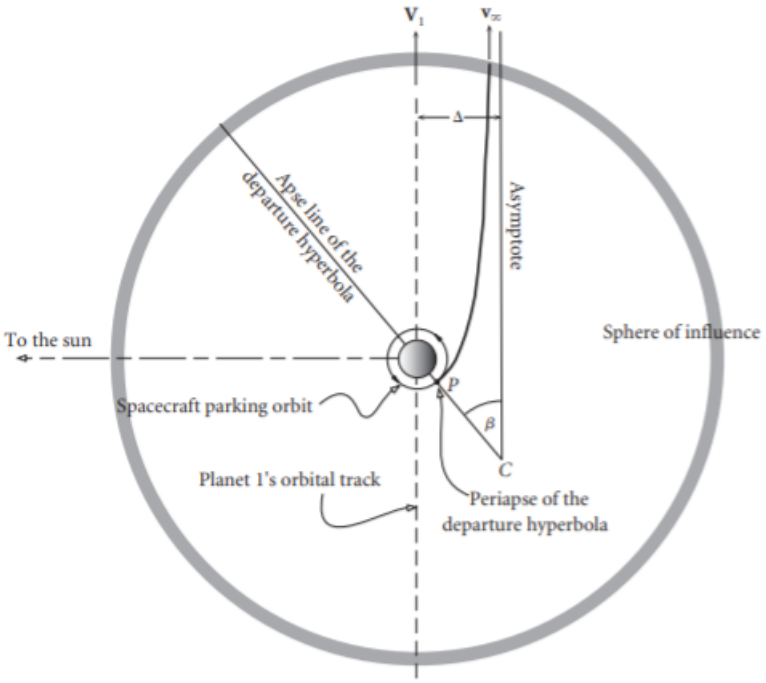

Figure 3.4: Departure trajectory using the patched conic approximation. Credit: (Curtis, 2008).

This approximation is needed for two reasons: the theoretical ΔV for the Hohmann transfer might not be enough to escape the sphere of influence of the body and, in order to increase or decrease the velocity of the spacecraft in the heliocentric reference frame, it must leave the sphere of influence in the right direction.

Indeed, the speed of the spacecraft in a heliocentric reference frame will be given by the vector sum of the spacecraft's speed in the geocentric reference frame and the speed of the Earth in the heliocentric one.

To maximize the gain, the spacecraft's speed at the asymptote must be aligned with the Earth's velocity; to accelerate the direction must be the same while to decelerate it must be the opposite. The velocity v_∞ in Figure 3.4 should indeed be given by the difference between the insertion velocity and the planet's velocity on the ecliptic plane. However, taking into account the discussion at the end of the previous section, this will now be ΔV_{pl}.

The velocity at the periapsis can be obtained through (Curtis, 2008):

$$v_p = \sqrt{v_\infty^2 + \frac{2\mu_e}{r_p}} \tag{3.12}$$

and therefore the periapsis ΔV is obtained by the difference between this and the circular orbit's velocity:

$$\Delta V = v_p - \sqrt{\frac{\mu_E}{r_p}} \tag{3.13}$$

In order to have an alignment between the asymptote and the body's velocity the impulse must be done at the angle β in the picture, computed as (Curtis, 2008):

$$\beta_{pc} = cos^{-1}(\frac{1}{1 + \frac{r_p v_\infty^2}{\mu_e}}) \tag{3.14}$$

Of course, in case of a deceleration, this angle must be shifted of 180°.

Moreover, considering Figure 3.3 in case of an unaligned ΔV_{pl} one must consider also the angle between v_1 and ΔV_{pl} itself, that can be called β_{pl}. This can be computed summing θ_{pl} and α_{pl}, computed through:

$$\alpha_{pl} = asin(\frac{v_1 sin(\theta_{pl})}{\Delta V_{pl}}) \tag{3.15}$$

The angle in a heliocentric reference frame will be given by the sum of β_{pc}, β_{pl} and the angle of the central body's velocity vector, plus eventual 180° in case of a deceleration.

Lastly, the plane change impulse is simply given by the difference between the component $v_2 sin(\delta)$ and the third component of the planet's velocity, considering that the parking orbit has been defined on the plane.

Launcher limitations and trajectory optimization

On a first approach, the Ariane 6 has been considered as a candidate launcher for the mission. According to the user manual (Laiger, 2021), the launcher is capable of providing a maximum excess velocity of 2.5 km/s with free declination.

Since the launcher can launch with free declination and the plane change is expensive in terms of ΔV the inclination i and the right ascension of the ascending Node Ω have been changed in order to have a burn aligned with the velocity and thus a null plane change. The true anomaly has been set null and all the other parameters have not been changed.

Being $v_1 = \sqrt{\frac{\mu_E}{r_p}}$ and v_V and v_N the components of the impulse respectively, aligned with v_1 and perpendicular to it ((a) in Figure 3.3) one can compute the new Keplerian elements and the new impulse as (right equations are for i $>$ 180°):

$$\Omega' = \theta \qquad \Omega' = \theta + 180 \tag{3.16a}$$

$$\theta' = 0 \qquad \theta' = 180 \tag{3.16b}$$

$$i' = arctan(\frac{v_N}{v_1 + v_V}) \qquad i' = 360 - arctan(\frac{v_N}{v_1 + v_V}) \tag{3.16c}$$

$$v'_V = \sqrt{(v_1 + v_V)^2 + v_N^2} - v_1 \qquad v'_V = \sqrt{(v_1 + v_V)^2 + v_N^2} - v_1 \tag{3.16d}$$

$$v'_N = 0 \qquad v'_N = 0 \tag{3.16e}$$

At this point, the only impulse will be aligned with the initial velocity and therefore reduced.

3.3.4 General Mission Analysis Tool implementation

Once all the previous values have been determined, they can be used as inputs for the propagation of the orbit in GMAT through the use of numerical propagators. Since no constraints were present on

the departure date, the first available launch window has been selected.

The default propagator has been used: it is an 8th-order Runge-Kutta method with a maximum step size of 2700 s and a minimum step size of 0.001 s. The error control is the $RSSStep$ and it is based on the relative error estimated through the root sum square method relative to the current state vector and at each step it must be, by default, lower than 10^{-11}; if the accuracy is violated the step width is decreased until this criterion is met (GMAT, 2020).

On the base of the default propagator, three different propagators have been created changing the central body, all of them were inertial with the central body and included all the terrestrial planets and the Moon as point masses: $Earth\_Prop$, Sun_Prop and $Venus\_Prop$.

For the Earth propagator, the Joint Gravity Model 2 (JGM-2) available within the software has been used, while for the others no gravity models have been adopted, spherical gravity potential has been assumed.

The initial parking orbit is defined through the date obtained from the Hohmann transfer theory as optimal date of departure, the parking orbit radius, arbitrarily chosen, and the values obtained through the equations of the previous section.

The impulse has been created as impulsive burn in the VNB reference frame, in which the x-axis is pointing in the spacecraft's velocity direction, the y-axis is in the direction normal to the orbit's plane and the z-axis is perpendicular to the previous ones to complete a right-handed coordinate system. The ΔV obtained above has been then assigned to the x component.

The mission has then been defined through four steps: the initial burn, the propagation inside the SoI of the Earth through$Earth_Prop$ until the radial distance from the planet was higher than SoI_e, the propagation through Sun_Prop until the radial distance from Venus was lower than SoI_v and the final propagation inside the SoI of Venus through the $Venus\_Prop$ until the periapsis around the planet.

Although the theoretical basis of the previous sections supported the inputs of the simulation, they were of course approximations: indeed as expected the first attempt did not reach the SoI of Venus, therefore it was necessary to add another stop condition to the Sun_Prop in order to make it stop whenever the periapsis around Venus was reached.

To correct the inputs to achieve an orbit which periapsis is inside Venus' atmosphere, a non-linear optimizer based on Sequential Quadratic Programming (SQP) called $Yukon$ has been used to modify the parameters of interest, minimizing the radial distance from the planet.

Once a value close to the planet's atmosphere has been reached, a Differential Corrector (DC) - based on the Newton-Raphson method – has been used to slightly correct the parameters to achieve a precise value of the periapsis, thus concluding the process of trajectory's determination.

The last propagation's stopping criterion has been modified to end the propagation at 20000 km from the planet in order to output, in the inertial reference frame, the spacecraft's position and velocity components to be used as initial conditions in an external atmospheric flight propagator.

Lastly, to obtain a reference value for the ΔV needed to achieve an orbit around the Planet the DC has been used with a second burn at the periapsis and a subsequent propagation up to the apoapsis of the planet, imposing a final distance lower than the SoI radius.

3.4 Atmospheric trajectories propagator ATP

In order to model the atmospheric flight, an external propagator has been created on Octave/Matlab based on the Runge-Kutta method: a numerical integration technique that allows to determine the value of the dependent variables at a future time through a weighted summation formula (Cappellari et al., 1976).

The code has been created to let the user choose between three propagators, a 4th order one and an 8th order one with fixed step sizes, or a 5th order embedded method to use adaptive step sizes.

3.4.1 Runge-Kutta methods

Given the time step h and the value of the dependent variable at the present time X_n, one can compute the increment of such variable in the time step as (James et al., 2008):

$$X_{n+1} = X_n + Ah \sum_{i=1}^{Ord} c_i k_i \tag{3.17}$$

Where k_i are the evaluations of the dependent variable at certain fractions of the time step and A and c_i are coefficients that depend on the order of the propagator. The values of k_i can be determined as (James et al., 2008):

$$k_i = F(t_n + a_i h, X_n + \sum_{j=1}^{i-1} b_{ij} k_j) \tag{3.18}$$

The coefficients A, a, b and c are reported in the tables called Butcher's tableau. The 4^{th} order one is reported below in Table 3.1, while the 8^{th} order one and the 4-5^{th} embedded one are reported in Appendix A, respectively in Table A.1 and Table A.2.

Table 3.1: Coefficients for the 4th order RK propagator (James et al., 2008).

i	a	b_{i1}	b_{i2}	b_{i3}	
1	0				
2	1/2	1/2			
3	1/2	0	1/2		
4	1	0	0	1	
	A	c_1	c_2	c_3	c_4
	1/6	1	2	2	1

These numerical methods can work in two ways: with a fixed number of steps to be performed, or with some stopping conditions to be met.

Although the first approach is computationally better because it allows for the pre-allocation of memory, one should know a priori the ToF to compute the number of steps. However, this is not possible in parametric studies, where the different initial conditions will result in different trajectories and, therefore,

at different times of flight. Lastly, changing the steps' dimensions to capture better certain parts of the trajectory would require the continuous adjustment of the total number of steps.

The imposed stopping conditions relate to to the altitude and the velocity. The altitude should be comprised between 0 km and the upper limit of the atmosphere, however, since the steps are finite, numerical errors might occur when the parameter of interest changes its sign if the steps are too wide, therefore the lower limit should be set to 5-10 km or more. To avoid stopping the propagator some steps before the actual atmosphere upper limit, again due to the discrete steps, the upper limit should be raised of 5/10 km as well.

The same numerical errors might occur for the velocity in case of a complete stop of the spacecraft by the atmospheric drag, therefore the lower limit of the velocity should be set to a minimum of 10 m/s. The stopping conditions can however be changed by the user, as, for instance, there is no need to propagate up to 5 km if the study is on an aerocapture and entry trajectories are not desired.

The last stopping condition is trivial and just imposes that if one of the evaluations of the variable at some fractions of the step had failed, none of the next ones will be computed and that increment will not be computed, thus stopping the propagation.

Dormand-Prince method

The Dormand-Prince method is an embedded method that allows monitoring the local truncation error to use adaptive step size (Dormand and Prince, 1980).

As can be seen from the tableau in Table A.2 the intermediate steps can be used to compute a 4th order solution and a 5th order solution, which will have an error, respectively of the 5th order and the 6th order, as these are the higher terms excluded from the series.

Subtracting the two solutions, the local truncation error can be estimated: it will depend on the step size used, in this case, to the power of 5, neglecting higher-order errors.

Introducing an allowed tolerance ϵ, the local truncation error can be compared to the tolerance to check if the used step size was small enough and, in case it was not, to adjust it and repeat the calculations; in case the step size is small enough, the next one is increased as well to speed up the calculations.

To adjust the step size, the following formula is used:

$$h_{n+1} = Kh(\frac{\epsilon}{E})^{1/5} \tag{3.19}$$

where K is a margin taken to avoid repeating the calculations (usually K = 0.9), and E is the local truncation error computed as mentioned above. In this case, the relative error to the 5th-order solution is used.

3.4.2 Set of equations

The propagator accounts for three Degrees of Freedom (DoF), thus the capsule will be modelled as a point mass where all the forces are applied; the moments will not be considered.

The equation of motion can be written as (Curtis, 2008):

$$\ddot{x} = \vec{a_G} + \vec{a_A} \tag{3.20}$$

where the term a_G is the gravitational acceleration and the term a_A is the term given by aerodynamic forces.

Since a numerical integration is performed, at each step the accelerations will give the increment in velocity and the velocity will give the increment in position.

Gravity term

In this model the influences of Venus, the Sun and the Earth have been considered, however while the Sun and the Earth have been modelled as point masses, the J_2 term has been used to correct the oblacity of Venus, although minimal.

The gravitational force between two point masses is given by Newton's law of universal gravitation as (Curtis, 2008):

$$\vec{F_G} = \frac{GM_1M_2}{|r|^3}\vec{r} \tag{3.21}$$

where G is the universal gravitational constant, M_1 and M_2 are the masses of the two bodies and $\vec{r}$ is the distance between them. Through Newton's first law, one can obtain the acceleration of one body as:

$$\vec{a_{G1}} = \frac{\vec{F_N}}{M_1} = \frac{GM_2}{|r|^3}\vec{r} = \frac{\mu_2}{|r|^3}\vec{r} \tag{3.22}$$

The non-sphericity has been modelled through the J_2 term; the gravity potential U including this extra term can be written as (Van Der Hilst, 2004):

$$U = -\frac{GM}{r} + \frac{GJ_2MR_{eq}^2}{r^3}(\frac{3}{2}sin^2\lambda - \frac{1}{2}) \tag{3.23}$$

The first term is the one discussed above, while the second one is the correction given by the term J_2; R_{eq} is the body's equatorial radius and λ is the latitude. The gravitational potential is the ratio between the potential energy and the mass; as the derivative of the energy will give the force, the derivative of its ratio over the mass will give the gravity acceleration.

From its definition:

$$sin^2\lambda = \frac{z^2}{x^2+y^2+z^2} \tag{3.24}$$

Clearly, the potential cannot be expressed as function of r only because of the latitude, therefore the partial derivatives of the potential in terms of x, y and z have to be done. Considering $r = \sqrt{x^2+y^2+z^2}$, one can write:

$$U_{J2} = \frac{3}{2}\mu J_2R^2(\frac{z^2}{(x^2+y^2+z^2)^{\frac{5}{2}}} - \frac{1}{3(x^2+y^2+z^2)^{\frac{3}{2}}}) \tag{3.25}$$

$$\begin{bmatrix} a_{xJ_2} \\ a_{yJ_2} \\ a_{zJ_2} \end{bmatrix} = \begin{cases} \frac{\partial U_{J2}}{\partial x} = K\frac{x(x^2+y^2-4z^2)}{(x^2+y^2+z^2)^{\frac{7}{2}}} \\ \frac{\partial U_{J2}}{\partial y} = K\frac{y(x^2+y^2-4z^2)}{(x^2+y^2+z^2)^{\frac{7}{2}}} \\ \frac{\partial U_{J2}}{\partial z} = K\frac{z(3x^2+3y^2-2z^2)}{(x^2+y^2+z^2)^{\frac{7}{2}}} \end{cases} \tag{3.26}$$

where K is the constant term $\frac{3}{2}\mu J_2 R^2$.

Regarding the Sun's and Earth's influence, considering both as external bodies, not influencing each other, the acceleration term is given by (Cook, 1962):

$$R = \mu_d(\frac{1}{\Delta} - \frac{xx_d + yy_d + zz_d}{r_d^3}) \tag{3.27}$$

$$\begin{bmatrix} a_{x_G ex} \\ a_{y_G ex} \\ a_{z_G ex} \end{bmatrix} = \begin{cases} \frac{\partial R}{\partial x} = -\mu_d(\frac{x-x_d}{\Delta^3} + \frac{x_d}{r_d^3}) \\ \frac{\partial R}{\partial y} = -\mu_d(\frac{y-y_d}{\Delta^3} + \frac{y_d}{r_d^3}) \\ \frac{\partial R}{\partial z} = -\mu_d(\frac{z-z_d}{\Delta^3} + \frac{z_d}{r_d^3}) \end{cases} \tag{3.28}$$

with $[x_d, y_d, z_d]$ the position of the external body and:

$$\Delta^2 = (x - x_d)^2 + (y - y_d)^2 + (z - z_d)^2 \tag{3.29}$$

Summing up all the components – Sun, Earth, and Venus as point masses and J_2 correction – the gravity term is obtained.

Aerodynamic term

The presence of the atmosphere will result in the appearance of the aerodynamic forces which the body will be subjected to: lift and drag.

The drag, much more relevant in an atmospheric entry, can be written as:

$$\vec{D} = \frac{1}{2}\rho S C_D |v| \vec{v} \tag{3.30}$$

where ρ is the density, S is the reference area, C_D is the drag coefficient and $\vec{v}$ is the velocity relative to the atmosphere.

Using again Newton's first law, one can obtain the deceleration as:

$$\vec{a_D} = \frac{\vec{D}}{m} = \frac{1}{2}\rho\frac{SC_D}{m}|v|\vec{v} = \frac{1}{2}\rho\beta^{-1}|v|\vec{v} \tag{3.31}$$

where the ballistic coefficient $\beta = \frac{m}{SC_D}$ has been introduced.

The lift can be easily computed knowing the ratio $\frac{C_L}{C_D}$ multiplying it by the drag; the vector however must be rotated in order to be perpendicular to the plane containing the drag vector.

Since the chosen reference frame is inertial, the relative velocity can be obtained from the difference

between the body's velocity vector and the tangential velocity of the planet in that point, computed as:

$$\vec{v_{rot}} = \vec{\omega_{rot}} \times \vec{r} \tag{3.32}$$

where $\vec{\omega_{rot}}$ has the form $[0, 0, \omega_{rot}]$ in which ω_{rot} is the angular velocity of the planet.

3.4.3 Algorithm

A quick description of the algorithm itself shall be done.

As can be seen in Figure 3.5, the inputs are read and the code is initialized: the planet and shape properties are obtained, and the first outputs are saved to be updated at each further step.

The loop starts, and the modifications presented in section 3.4.5 are checked and applied if that is the case, then the stopping conditions are checked and, in case they have been met, the calculation is stopped at the end of the current step. If the propagator does not have automatic step size modulation, then the size is adjusted and the actual step is performed. In case the modulation is automatic, the step is performed and the tolerance is checked, the step size is adjusted and in case it was too wide the step is repeated.

To make the step forward as explained in section 3.4.1 the same set of equations are applied at different intermediate steps: if one of these steps meets the stopping conditions then the outputs are post-processed and saved, if not the outputs are updated, the new C_D is computed through $Freespace$ if a shape file is provided and the loop starts again.

In order to compute the deceleration, the equations are applied to the current state and only the deceleration term is saved.

Since the influence of the variations of atmospheric density is important, this parameter is computed at each intermediate step, while the C_D and the positions of the external bodies, are computed at each loop.

The dashed shapes are for optional passages, as the use of $Freespace$ that can be avoided using a fixed ballistic coefficient or the ephemeris file that can simply not be provided.

3.4.4 Auxiliary data and Freespace

Some auxiliary data are needed for the correct functioning of the ATP software or to add complexity and details to the solution.

Atmospheric models

To compute the density for the computation of the drag and the heat fluxes, an atmospheric model must be used reporting, at least, the density in function of the altitude. More detailed models can also include the composition of the atmosphere, the thermodynamics properties, winds, etc. Moreover, although the altitude variations are the most important ones, there exist variations of the atmospheric

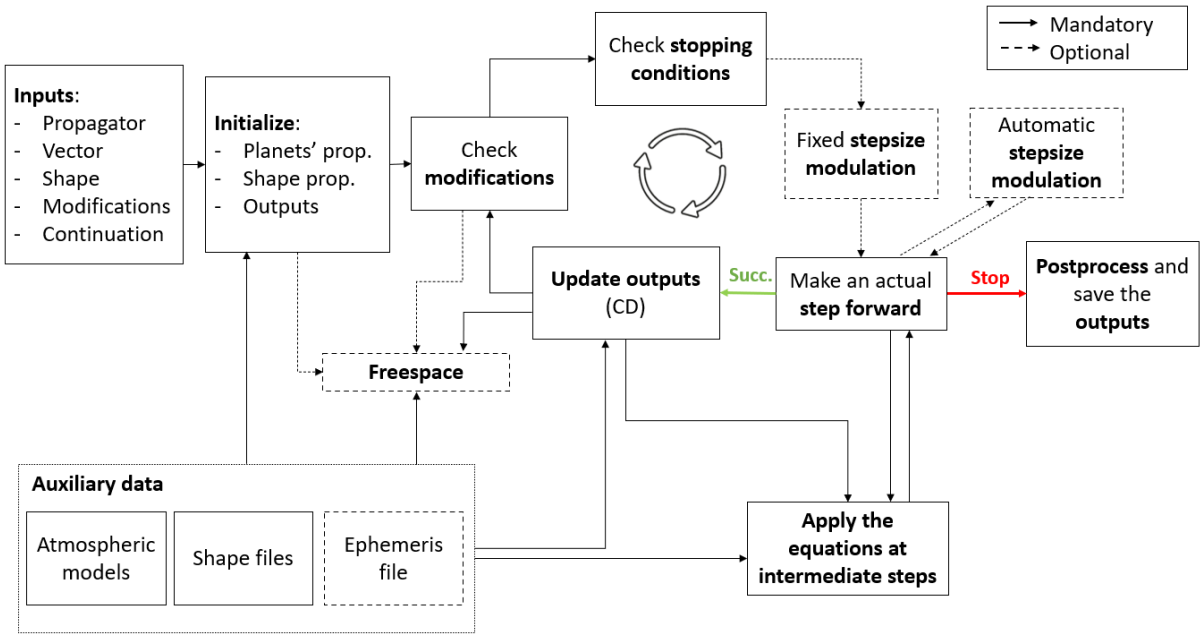

Figure 3.5: Algorithm workflow.

properties with respect to the position (latitude and longitude), time (time of the day, date), and solar activity.

For this study, two atmospheric models have been used, according to need: an atmospheric model with just altitude variations, but reporting every thermodynamics property and the major species atmospheric composition, and another one, with Solar Zenith Angle (SZA) variations between 250 km and 150 km, day/night variations between 150 and 100 km, and latitude variations below 100 km but reporting just the density.

The first one is part of $Freespace$ (section 3.4.4), while the other one is obtained by converting the data of Venus-GRAM into an octave file (Justh et al., 2021).

The SZA is defined as the angle between the vertical direction and the sun rays. In three dimensions it can be easily obtained by applying the same method used to find the flight path angle γ (section 3.2), but with respect to the vector between the spacecraft and the sun computed as the difference between the Sun's position vector and the spacecraft's one. Note that the used convention is different: this angle is measured from the vertical axis, and it is comprised between 0 and 180°.

To understand whether the spacecraft is on the day side or the night side, or if it has Line of Sight (LoS) with the Earth the following construction has been done considering the Sun, as it is representative of both cases:

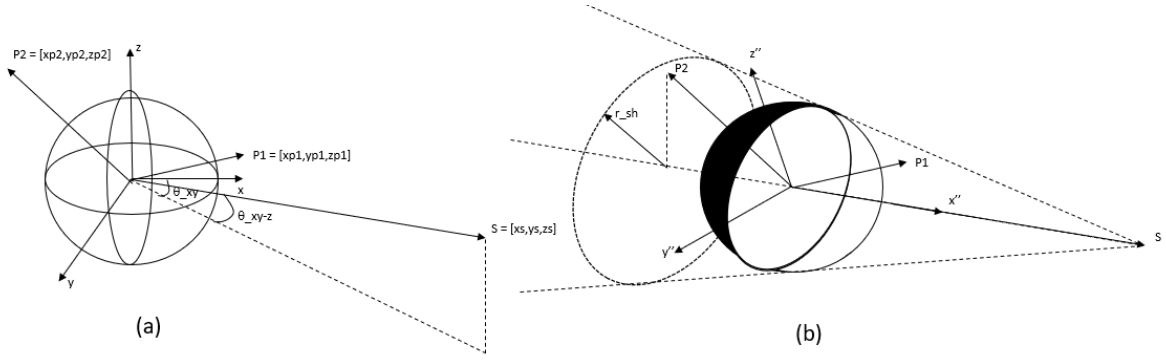

Figure 3.6: Day/Night determination.

As can be seen in (a) of Figure 3.6 there are two points P1 and P2, characterized by their position vectors, and the Sun with coordinates $[x_s, y_s, z_s]$; as already seen these can be described by the two angles in Equation 3.5a, Equation 3.5b and two rotations can be done in order to have the Sun's position on the x"-axis (b) (Figure 3.6).

Every point with positive x" coordinate will be on the day side, since the planet will always be behind him: this is the case of P1. If the x" coordinate is negative, then one must check if the position is inside the cone of shadow. Applying simple geometrical rules, the radius r_{sh} can be computed as:

$$r_{sh} = R_{eqV} \frac{\sqrt{x_s^2 + y_s^2 + z_s^2} + |x''_{P2}|}{\sqrt{x_s^2 + y_s^2 + z_s^2}} \tag{3.33}$$

If even only one between y''_{P2} and z''_{P2} is greater than r_{sh} then the point will be out of the shadow.

Note that theoretically the apex of the cone should not be the position of the external body as it is not a point.

If the radius of the external body is smaller than Venus' one (left side of Figure 3.7) then the apex is moved further from Venus of a distance:

$$R_{extra} = \frac{\sqrt{x_s^2 + y_s^2 + z_s^2}}{\frac{R_{eqV}}{R_{eqS}} - 1} \tag{3.34}$$

and equation Equation 3.36 can be used adding this to both the numerator and the denominator.

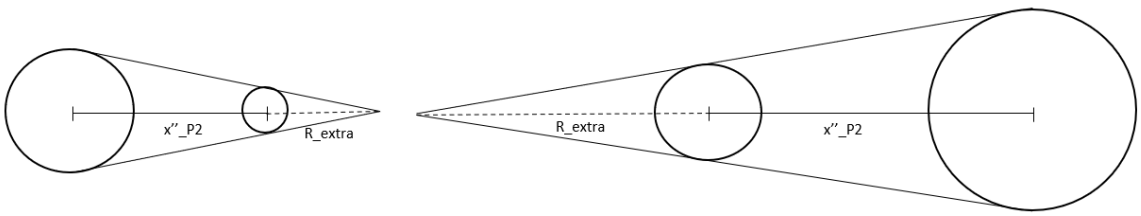

Figure 3.7: Day/Night determination, part 2.

If the radius of the external body is instead bigger than the central body (right side of Figure 3.7), the cone will be reversed, and the apex will now be behind it. The extra distance will now be computed as:

$$R_{extra} = \frac{\sqrt{x_s^2 + y_s^2 + z_s^2}}{\frac{R_{eqS}}{R_{eqV}} - 1} \tag{3.35}$$

and $r_s h$ will now be given simply by:

$$r_{sh} = R_{eqV}(1 - \frac{|x''_{P2}|}{R_{extra}}) \tag{3.36}$$

Ephemerides files

It is obvious that to compute the SZA or the day/night side, as well as the disturbing gravity of external bodies an ephemeris file with the position of the Sun and the Earth in the used reference frame must be given as auxiliary file. A transfer function should be achievable to transform the position vector in a sun-referenced frame to a Venus-referenced one through three rotations.

However, attempts to find the rotation angles between the two frames, revealed how these angles are not fixed but vary with the epoch; at the moment of writing this document no transfer function has yet been found. Further efforts are needed in this sense.

The Horizon system can be used to download the ephemeris files with custom centre and orientation of the axes, however one must be careful to avoid problems as the one discussed in section 4.2. Moreover, the application was not working with Earth-centred reference frames.

The method used for the Earth referenced ephemeris was to model an orbit around the planet, and propagate it with very small step sizes on GMAT, reporting the position of the Sun and the Moon on the wanted reference frame. Note that the step size control is referred to the orbit of the spacecraft and therefore using large step sizes and for long periods of time will result in inaccuracies on the position of the external bodies, therefore a propagation with small step sizes and for short periods of time is suggested. This issue is already reported in (GMAT, 2020).

The ephemeris files must report the position vectors of the Sun and the Earth (Sun and Moon if the central body is the Earth) varying with the Julian epoch.

Freespace

A powerful tool called $Freespace$ has been used to supplement the code in challenging areas as the computation of the aerodynamic coefficients, heat fluxes, wall temperatures, etc. and providing a big baseline of database containing lots of atmospheric models and vehicle shapes (Lino da Silva, 2020).

The code is based on Newtonian theory and uses a panels' method to discretize the surface and apply the hypersonic relations to each panel section (Anderson, 2006).

Although a 3D version exist, for this work the 2D axisymmetric version has been used.

The atmospheric properties are taken from the available atmospheric models and a geometry file must be given with the coordinates of the panels' extremesand some other parameters as the characteristic length L_c, the nose radius r_n, etc.

The regime of the flow is divided in free-molecular, transitional or continuum according to the Knudsen number Kn: for $Kn < 0.01$ the flow is continuum, $Kn > 10$ the flow is free molecular while in

between it is transitional.

In free-molecular, Schaaf and Chambre theory (Schaaf and Chambre, 1958) is used to compute surface pressure and skin friction coefficients C_p and C_τ, while Kemp and Ridell theory (Kemp and Riddell, 1957) is used for the stagnation point heat fluxes.

Modified Newtonian theory using Rayleigh Pitot tube formula is used for the C_p in continuum flow (Anderson, 2006), while a null C_τ is assumed; the 70% vacuum rule is used on the leeward side if present (Kinney et al., 2001). Sutton-Graves formula (Sutton and Graves, 1971) is used for stagnation convective heat fluxes and modified Lees theory is used to compute the heat fluxes along the surface (Lees, 1956; Fritsche et al., 2000).

Not being part of this work, the formulas have not been reported here and can be found in the manual (Lino da Silva, 2020), however it is worth reporting Sutton-Graves' formula, relevant for this work:

$$\dot{q_{max}} = K\sqrt{\frac{\rho}{r_n}}v^3 \tag{3.37}$$

The value of K depends on the atmospheric composition, and its value for different planets is reported in Table 3.2.

For the transitional regime, two bridging functions have been used: Wilmoth's one (Wilmoth et al., 1999) for the aerodynamic coefficients and Legge's one (Legge, 1987) for the heat fluxes.

Lastly, a thin or thick wall can be assumed. For the thin wall a balance is imposed between convective heating and radiative emission (using emissivity 0.8 as suggested in Redmond and Mastropietro (2015)) thus finding the wall temperature as function of the incoming heat fluxes; since Kemp and Ridell formula needs the wall temperature, some loops are needed to make the two values converge. For a thick wall the properties of the wall are needed as well and conduction is also taken into account. An isothermal wall can be assumed as well.

Shape files

The last type of auxiliary files are therefore the shape files needed by $Freespace$: the code already has its own database of vehicle shapes, but the user can define its own geometry.

For the purpose of this work, a generator of sphere-cone geometries has been implemented to let the user build easily the geometry that most suits its applications.

The sphere cone is divided in three parts: spherical cap, truncated cone and back shell, and it is completely defined by 5 parameters: nose radius r_n, base radius R, angle θ_{SC}, back radius r_b and back angle θ_b.

3.4.5 Inputs and mission elements

Although born to be used on Venus, the ATP code has been extended to the bodies whom atmospheric models were available on $Freespace$; their properties have been reported in Table 3.2:

Table 3.2: Planets' properties.

Properties	Venus	Earth	Mars	Neptune	Sun	Moon
μ [km$^3/s^2$]	324858.5988	398600.4415	42828.3143	6836534.0639	132712440017.99	4902.8006
J2 [$\cdot 10^{-6}$]	4.4044	1082.6267	1958.7442	3411		
R_{eq} [km]	6051.9	6378.1363	3397	25269	695990	1738.2
ω_{rot} [$\cdot 10^{-7}$ rad/s]	2.9924	729.2115	708.8218	1083.3825		
Atmosphere Limit [km]	250	999	250	4000		
Sutton-Graves K [$\cdot 10^{-4}$ m$\sqrt{kg}$]	1.8960	1.7623	1.8980	0.6719		

The first four rows are taken from GMAT and supplemented by NASA planetary fact sheets (Williams, 2016), where the rotational velocity is computed as 2π over the sidereal rotation period in seconds. The fifth row depends on the available atmospheric models, and the sixth row's values are from $Freespace$ that uses the values in (Samareh, 2009). For the Sun and the Moon just μ and R_{eq} has been reported since they are used only as external bodies or to project shadows. The first input is therefore the choice of the central body, followed by the selection of the propagator.

Propagator

In case the 4th- or 8th-order propagators are chosen the initial step size must be given; a size modulation is recommended in order to decrease it at certain altitudes to better capture certain parts of the trajectory, however, it will depend on the central body under study and several trials are needed at the beginning to minimize the errors. If the initial step size is smaller than the ones of the modulation, the smaller one is taken, allowing to propagate orbits with a fixed small step size.

As said above the 5th-order propagator has an automatic step size modulation, once the tolerance, minimum and maximum allowed step sizes are chosen, the step sizes will be adjusted automatically at each step.

Lastly, the stopping condition discussed above shall be provided. If they are lower than the limit values, then those will be used.

Initial conditions

The initial conditions of the spacecraft can be given in three different ways:

- R8th-order last vector of a GMAT report file.
- Writing the state vector to the input file.
- Providing entry altitude, velocity, and flight path angle. These can be supported by the longitude, latitude, and velocity angle θ_{vxy}.

If latitude and longitude are used, or if an ephemeris file is included, the Julian epoch must be given as well as input.

Once the initial setting is done, with a defined state vector around a given planet at a certain date, the mission parameters must be defined.

Shape

The first choice is whether to use a constant ballistic coefficient, or to use a specific shape file and compute the C_D at each step. The first choice is of course faster since it does not need to call $Freespace$ and is useful to compare with literature as constant ballistic coefficient is often assumed, the second one is slightly slower but adds an extra level of detail; in case the shape file is selected the spacecraft's mass must be provided as well. As said above, one can select a shape file already present on the database or create a sphere-cone geometry with custom properties.

Note that to compute heat fluxes the nose radius must be given even in the case a constant ballistic coefficient is chosen.

Trajectory corrections

A useful feature of the code is the option to make trajectory corrections or events at a specific altitude or at the periapsis:

- The entry angle and entry velocity can be changed at the atmosphere limit. (Entry correction).
- If used, the ballistic coefficient can be changed at a given point. (Drag modulation).
- The L/D ratio can be changed at a given point. (Lift modulation).
- The shape file can be changed at a given point. (Opening of a parachute).
- The spacecraft's mass can be changed at a given point. (Drop of a secondary capsule.)
- The flight path angle and the velocity can be changed at a given point. (Mid-term burn).

Orbit continuations

Lastly, the code allows choosing a finite number of orbits to propagate after the atmospheric passage in order to obtain information on the orbital period, eclipse times, communication windows and other useful parameters. The propagation can stop at a given apoapsis (first, second, etc.), at the entry or at the exit of the atmosphere after a certain number of apoapsises. If the number of apoapsises is zero, then the propagator will stop at the exit of the atmosphere.

In case of aerocapture or aerobraking, it might be useful to raise the periapsis performing a burn at the apoapsis, the amount of ΔV and the number of apoapsises at which to perform this burn can be given as inputs as well.

Another useful input is the density scale factor: it might be needed to introduce an uncertainty on the density (typically 20%) in order to account for uncertainties in the atmospheric model from old data collected by low accuracy instrumentation, local fluctuations and so on.

3.4.6 Outputs

The outputs are saved in an Excel file and can be divided in sections as follows. The outputs are also shown in form of charts at the end of the output file.

Shape

These outputs are computed automatically on Excel and therefore does not require running the code to obtain the results. These computations are not needed for the code. Moreover, it is only needed if the sphere-cone geometry is used and gives results on the geometrical properties of the created shape as wet and lateral areas, volume, and so on; a TPS thickness and a structure thickness can also be provided with their respective densities to compute the geometrical properties of these layers as well as their mass.

Trajectory and Data

This is the most important section, as it comprises most of the outputs needed for a mission analysis.

The entry conditions in terms of altitude, velocity, and angle are saved before and after the eventual entry corrections, and the state vectors are saved as well.

Then the most relevant parameters are shown as well, to be easily compared with other trajectories or eventual mission requirements (Table 3.3).

Table 3.3: Characteristic trajectory's parameters.

Periapsis altitude	Peak heat flux	Peak deceleration	Peak dynamic pressure	Delta-V

A lot of quantities are reported for each step: the time, altitude, and velocity are reported for the whole trajectory, even outside the atmosphere, as well as the eclipses' information, while the other ones are reported just for the atmospheric passage (Table 3.4).

Table 3.4: Trajectory's outputs.

Whole trajectory				
Step number	Time	Altitude	Velocity	
Earth LoS	Sun LoS	Earth distance		(Ephemeris needed)
Atmospheric flight				
Flight path angle	Convective, radiative and total heat fluxes	Heat load	Deceleration	Dynamic Pressure
Drag coefficient	Ballistic coefficient	Wall temperature		($Freespace$ needed)

The radiative heat fluxes are actually computed just for the case of Venus, and the following correlation is used, based on Pioneer Venus mission data (Tauber et al., 2012):

$$\dot{q_{rad}} = 8.497 \cdot 10^{-63} v^{18} \rho^{1.2} r_n^{0.49} \qquad 10.028 \text{ km/s} < v < 12 \text{ km/s} \tag{3.38a}$$

$$\dot{q_{rad}} = 2.195 \cdot 10^{-22} v^{7.9} \rho^{1.2} r_n^{0.49} \qquad v < 10.028 \text{ km/s} \tag{3.38b}$$

Correlations for the other celestial bodies should be implemented as well.

The convective heat fluxes, when $Freespace$ is not used, are computed using Equation 3.37, assuming continuum flow within the whole trajectory; although this is incorrect, the heat fluxes experienced during rarefied regime are expected to be much lower than the ones in continuum, and this assumption should not introduce errors in the design parameters. Lastly, the heat load, being the integral of the heat fluxes over time, is computed through numerical integration of the heat fluxes along the steps.

Atmospheric properties

In this section, the atmospheric properties are saved; these are:

Table 3.5: Atmospheric properties.

Density	Temperature	Pressure	Molar mass	Specific heat ratio	Knudsen number	Mach number

Vectors

The state vectors and the Julian epoch in the inertial reference frame are saved. The last vector of the whole trajectory is also saved to start another simulation from the last point or to use it as input on GMAT.

DeltaV ΔV

The ΔV needed for the entry correction, midterm correction and apoapsis burn are saved, and the total ΔV is computed.

Eclipses

This last section gives information regarding the eclipses from the Sun and the Earth, computing the times of eclipses and the average and maximum distance from the Earth.

3.4.7 Alternative versions

Once the ATP code has been developed two modified versions have been created: one in order to perform parametric studies, a key phase of the design of a space mission needed to understand the influence of the parameters of interest, and another one to perform Monte Carlo simulations to investigate the probability distribution of the outputs with variable inputs.

Parametric studies

Although the parameters that influence the trajectories are many, some of them cannot be really changed during the design phase or through small corrections as the Sun's position relative to the spacecraft or the geographical position of the spacecraft, on which the atmospheric properties, the gravity model and the atmosphere tangential velocity depend.

The three terms that mostly influence the trajectory and are relevant in the design phase are: the ballistic coefficient β, the entry velocity $|v|$ and the flight path angle γ.

While the entry velocity and the flight path angle are obtained from the interplanetary trajectory and can be just slightly adjusted using burns, the ballistic coefficient depends on the selected shape and the total mass of the spacecraft, thus it can be freely chosen during the design phase.

An input function has been therefore created to let the user perform an arbitrary number of iterations changing two of these three parameters, where the ballistic coefficient could be chosen freely while the entry velocity and the flight path angle are changed around the interplanetary values in the form of, respectively, a scale factor and extra rotations.

The different entry conditions will result in different trajectories, therefore to make an efficient comparison between them the key parameters in Table 3.3 will be plotted with respect to the range of selected parameters.

A post-processing script has been created to set limits to these quantities and derive frames of validity of the obtained trajectories.

Monte Carlo simulations

A Monte-Carlo version of the code has been developed as well, to perform uncertainties propagation: to perform a Monte Carlo analysis, the finite inputs are replaced by probability distributions from which random values are taken. In order to cover the whole distribution, a large amount of simulations should be done. The chosen inputs should be independent with respect to each other, and therefore should be selected carefully.

First, a statistical distribution should be taken for the entry conditions – velocity and angle – density and ballistic coefficient, as these are the parameters that affect the most in the trajectory. The density should be a scale factor as discussed above, and so should be the ballistic coefficient (again, usually 20%); for the entry velocity and entry angle one could set a range of values around the arrival one as for instance $\pm$ 10 m/s or $\pm$ 0.1° according to the needs. The user can choose between normal or uniform distribution for the inputs.

To account for the atmosphere variability and the influence of the planet's rotation, then one might have variations on the latitude, longitude, angle of the velocity and Julian epoch, however it is obvious that some combinations of latitude, longitude, entry velocity and angle would simply be impossible for certain interplanetary trajectory Moreover if such changes will result in simulations for both day and night sides, the differences could be big enough to result in a bimodal distribution. It is recommended to use reasonable variations around arrival conditions from an interplanetary trajectory.

Chapter 4

Results and discussion

4.1 Interplanetary trajectory

Once the ephemerides for the two planets were downloaded, the radii of the orbits were computed as the average of the semi-major axes and used to compute the angular velocity of the planets around the Sun, to compute t_h and α_h, reported in Table 4.1:

Table 4.1: Hohmann transfer values.

Planet	Radius r [km]	Angular velocity ω_{rot} [rad/s]
Earth	1.4960e+08	1.9910e-07
Venus	1.0821e+08	3.2364e-07
	Hohmann ToF t_h [s]/[d]	Hohmann angle α_h [rad]/[°]
Departure	1.2621e+07 / 146.08	-0.9431 / -54.036
Return	1.2621e+07 / 146.08	0.6288 / 36.028

The angles between the two planets on the ecliptic plane were computed for each day and imposed to be equal to the departure angle α_h; five launch windows were found.

As explained in section 3.3.2 several days before and after the departure were investigated, as well as different ToF: respectively 45 days before and after the departure date and 30% more or fewer ToF.

Iteratively, considering every combination of departure date and ToF, Lambert's problem was solved with the real planets' positions, giving the insertion and arrival velocity, as well as the plane change angle. Using these values and applying the method in Figure 3.3 has been applied with the obtained values and the values of ΔV_{pl} and ΔV_z have been found along the intervals.

Lastly, these values have been used to apply the patched conic approximation and the inclination optimization (section 3.3.3 and section 3.3.3) to find the minimum ΔV of the considered launch windows. In Table 4.2 are reported the computed values:

The launch windows can be represented in the so-called pork chop charts, representing the trend of the ΔV with respect to different departure and arrival dates; in Figure 4.1a, the pork chop of the first launch window is presented. After the optimal date has been found, the calculation has been repeated considering just $\pm$ 7 days from it and $\pm$ 10% of the optimal computed ToF (Figure 4.1b).

Table 4.2: Launch windows.

Window's number	1	2	3	4	5
Hohmann departure date	22-05-2023	25-12-2024	29-07-2026	09-03-2028	08-10-2029
Optimal departure date	20-05-2023	28-12-2024	05-08-2026	07-03-2028	03-10-2029
Optimal ToF [d]	157	140	133	169	155
ΔV [km/s]	2.4835	2.5383	2.5226	2.6561	2.5785
i [°]	2.1809	1.8796	4.8946	7.4073	4.5652
Ω [°]	180.4977	43.7538	71.0537	126.2007	155.9714
θ [°]	180	180	0	180	0

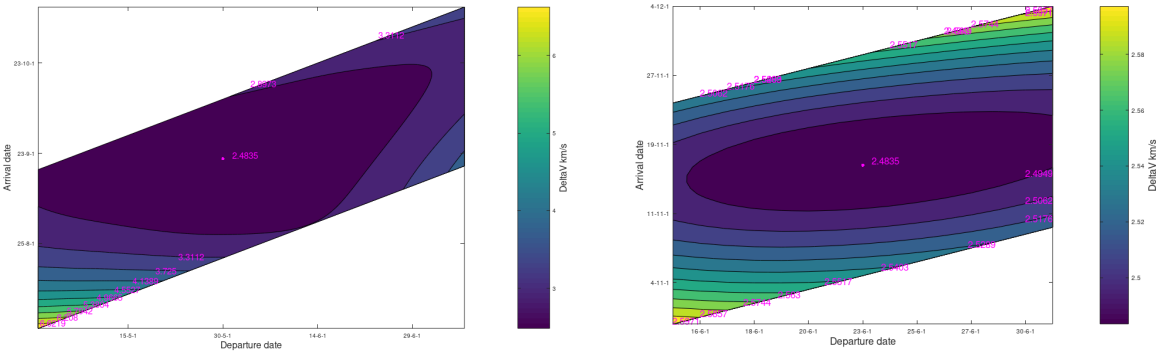

(a) Wide.

(b) Zoom-in.

Figure 4.1: First launch window's pork chop chart.

Lastly, these values have been used as inputs for the propagation in GMAT. In order to speed up the calculations at the beginning, just the Sun was considered in $Earth\_Prop$ and $Venus\_Prop$.

As expected, with these exact values the spacecraft did not manage to reach the SoI of Venus, and ended up with a periapsis of 192000000 km.

In 17 iterations using the $Yukon$ solver, modifying just the ΔV and Ω minimizing the distance from the planet, the periapsis has been lowered to 400000 km, inside the SoI.

At this point the DC has been used, modifying just Ω and the departure date with the objective of a periapsis lower than of 6155 km, i.e. an altitude of almost 105 km. Remember that GMAT has no atmospheric models for Venus and therefore the last part of propagation is useless, however, the real altitude will be near this value. In 50 iterations, the solver converged.

With the new values, all the terrestrial planets and the Moon were added to the propagators, resulting in a periapsis of 600000 km, still inside the SoI.

Then, the $Yukon$ solver was used again, reaching the planet in 25 iterations, however with a periapsis smaller than the planet's radius. In two iterations of the DC the periapsis of 6155 km was achieved through the following initial settings (the values are reported with greater accuracy to allow external comparisons):

In 94 iterations, divided in 4 different runs, a very detailed solution of the interplanetary trajectory was found. The outgoing energy was 6.1240151 km^2/s^2, giving an infinity velocity of 2.4746747 km/s, within the launcher capabilities; there was no need for further optimization of the trajectory.

Table 4.3: Analytical and GMAT solutions' comparison.

	Analytical solution	GMAT solution	Difference	Day side arrival
ΔV [km/s]	2.4835002	2.5438135	0.0603133	2.5438135
Julian epoch	30084.5	30084.2485566	-0.2514434 ($\sim$ -6 hours)	30085.0937192
i [°]	2.1809221	2.1809221	0	1.4374340
Ω [°]	180.4976952	182.8172370	2.3195418	182.2397908
θ [°]	180	180	0	180

Stopping the propagation at the atmosphere's top, the arrival Julian epoch is 30243.02248123: 158.77 days after the departure, near the computed value of 157 days (Figure 4.2)

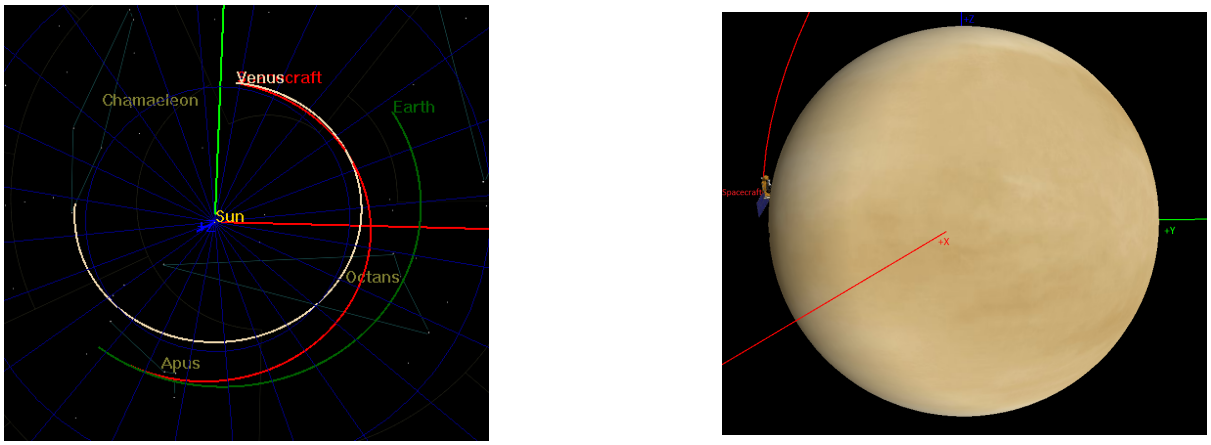

(a) Heliocentric reference frame.

(b) Close up of the periapsis.

Figure 4.2: Interplanetary trajectory on GMAT.

The arrival condition are summarized in the Table 4.4; the flight path angle is computed by the propagator as well as the latitude, longitude, and eclipses that have been successfully matched with GMAT outputs.

Imposing a burn at the periapsis to achieve an orbit around the planet, a ΔV of -0.7473937 km/s was found, resulting in an apoapsis of 600000 km, imposing it to -0.8 km/s gave an apoapsis of $\sim$ 292610 km.

The spacecraft arrives at the night side and its eclipse starts $\sim$ 542 seconds before reaching the top of the atmosphere; the LoS is possible until the top of the atmosphere, and it is lost $\sim$ 60 seconds after.

Fixing the latitude one can find which one is the longitude corresponding to the change between day and night side, and the same can be done fixing the longitude, in order to find how far the spacecraft is from the terminator. At the epoch in Table 4.4, fixing the latitude, the sun side is comprised between -71.57° and 109.48° therefore locating the spacecraft at 97.60° of longitude difference from the terminator, while fixing the longitude it will be comprised between -90.00° and -89.10°, with 58.47° of latitude difference between the spacecraft and the terminator.

Since the angular rotation of Venus is very low (a full rotation is completed in $\sim$ 243 Earth days) the values computed above will not change much within some days or even weeks; moreover, considering the low inclination of the planet, in order to obtain a trajectory arriving on the day side one can just target a longitude in the aforementioned range.

Looking at the plane containing the hyperbolic trajectory at the moment of the arrival, the arrival angle was iteratively changed in order to find a longitude in the day side range: the closest found value was -56.29°, very close to the terminator. The initial conditions needed to obtain this trajectory are reported in Table 4.3.

This means that in the way the trajectory approaches Venus, the side of the planet seen from the interplanetary trajectory, is almost completely in the day side, not achievable without crashing on the ground. The back side, where the spacecraft is redirected by the gravitational pull of the planet, is almost totally in the night side.

Again considering the slow rotation of Venus, in order to obtain a trajectory in the middle of the day-side a completely different trajectory should be obtained, however, the interplanetary trajectory was not the focus of this study, and it was just needed to have indicative entry values for the atmospheric flight: it is therefore believed to be acceptable within the scope of this thesis.

This value ensures a periapsis on the day side, however being very close to the terminator, the homopause level considered might be affected by the vicinity of the night side; the homopause altitude was averaged between day and night, thus making the limit altitude equal to 107 km. Moreover, note that the velocity angle is 251.83°, therefore going towards the night side as it was expected.

Table 4.4: Arrival conditions.

Night side J = 30243.0224812			Day side J = 30242.8910201		
X [km]	Y [km]	Z [km]	X [km]	Y [km]	Z [km]
2201.1195660	4955.8456447	-3210.4438451	-3514.3104123	-1602.2300108	-4983.4405187
Vx [km]	Vy [km]	Vz [km]	Vx [km]	Vy [km]	Vz [km]
-10.5773580	1.0902850	-2.1792268	-2.1991445	10.6233253	0.3343287
Altitude [km]	Velocity [km/s]	Flight path angle [°]	Altitude [km]	Velocity [km/s]	Flight path angle [°]
249.9612879	10.8542084	-9.1141858	249.9938794	10.8560770	-9.1154366
Latitude [°]	Longitude [°]	Velocity angle [°]	Latitude [°]	Longitude [°]	Velocity angle [°]
-169.17	-30.63	109.37	-52.25	-31.19	251.83

4.2 Atmospheric flight propagator ATP validation

In order to verify the used methods and their integration, a deep comparison between the developed code and GMAT has been carried out.

Although this thesis revolves around Venus, the absence of an atmospheric model on GMAT for the planet made necessary doing the comparison using the Earth as central body; moreover, the oblacity of the Earth made also easier to see the influence of J2 on the trajectory.

Since the inertial reference frame of GMAT is defined at a given epoch (J2000), it does not take into account the periodic variations of the spin axis: namely precession, nutation and polar motion.

From the picture at page 454 of (GMAT, 2020), one can understand which are the intermediate reference frames used to go from the J2000 inertial reference frame to the fixed reference frame at a given epoch. The intermediate reference frames as $MODEq$ or $TODEq$ are considered quasi-inertial because the axes change in time but, since they consider just nutation and precession, the changes

are considerable just over very long time scales and therefore can be considered inertial for short-term applications.

The geodetic latitude was obtained for a position vector of the form $[x, 0, 0]$ in different reference frames. The results are reported in Table 4.5 and show the differences discussed above: as all of them are referred to the equator they should have null latitude, however this is not the case:

Table 4.5: Latitude in different reference frames.

Reference frame	$MJ2000Eq$	$TODEq$	$MODEq$	$Equator$	$EarthFixed$	$ICRF$
Latitude [°]	0.0544	-0.0002	0.0014	-0.0002	3.1908e-15	0.0544

The $EarthFixed$ one is the only one taking into account polar motions as well, and therefore is the only one with a null latitude (beside numerical errors). $Equator$ and $TODEq$ are instead just updated for nutation and precession, thus have the nearest value to zero between all the quasi-inertial frames.

One must be careful on the selection of the reference frame because errors on the latitude might cause errors in the calculation of the J2 influence term or in the calculation of the local tangential velocity of the atmosphere and therefore in the computed drag vector.

The J2 perturbation is directly dependent on the latitude, while it might be more difficult to see the relation between latitude and relative velocity. A vector $[x, y, z]$ of magnitude r will have a latitude $atan(z, \sqrt{x^2 + y^2})$; an increase in latitude, keeping the same magnitude, will result in an increase in z and a decrease in $\sqrt{x^2 + y^2})$. The cross product in Equation 3.32 is between the position vector and a vector with the form $[0, 0, \omega_{rot}]$, resulting in a vector with magnitude $\omega_{rot}\sqrt{x^2 + y^2}$: an imprecision on the latitude will therefore result in errors on this magnitude.

A random vector of an entry trajectory at a random epoch has been chosen and used as input for the propagation in GMAT using the True of Date Equator $TODEq$ reference frame, and in the ATP code, as a state vector input.

For the used position vector, the geodetic latitude from GMAT was 19.016853523°, while computing it as in Equation 3.5b using the $EarthFixed$ coordinates gives 18.901929598°, this behaviour is however already reported in the documentation (GMAT, 2020).

4.2.1 Newton's law

The first comparison regarded just Newton's law of universal gravitation, and therefore all the other terms were set null. On GMAT the selected propagator was the $RungeKutta89$ with fixed steps of one second; the error control was disabled. The stopping condition has been set to a radius of 6400 km from Earth's centre and an output file with altitude, inertial velocity, fixed velocity and inertial acceleration has been created.

The 8th order propagator has been used on the ATP code with fixed steps of one seconds, with the same entry conditions and stop conditions.

The error was computed at each step for altitude, inertial and relative velocity and acceleration. The errors are computed relative to the GMAT solution and the maximum ones are reported in Appendix B,

in Table B.1.

In Table 4.6 the errors at the first step for altitude and velocities are reported, already giving useful information on the working of the two software:

Table 4.6: Initial relative errors.

Altitude	Fixed velocity	Inertial velocity	Acceleration
1.387e-15	-2.085e-08	1.261e-15	-9.365e-16

As can be seen, the errors on the altitude, inertial velocity and acceleration are in the order of 10^{-15} and, since they are computed from the same input state vector, they already show a difference between the two software in the way the values are saved. Since both of them use double-precision floating point, whose maximum digit is the fifteenth, it is normal to have errors of this order even starting from the same inputs.

The error on the inertial velocity is instead seven orders of magnitude greater, revealing some discrepancies in the computations as well.

This is due to the polar motion changes of spin axis position, resulting in latitude differences between the two reference frames, as seen above. Indeed, outputting the position in the used inertial reference frame and in the fixed one from GMAT.

In Figure 4.3 and Figure 4.4 the trend of the errors regarding altitude, velocities, and acceleration is shown:

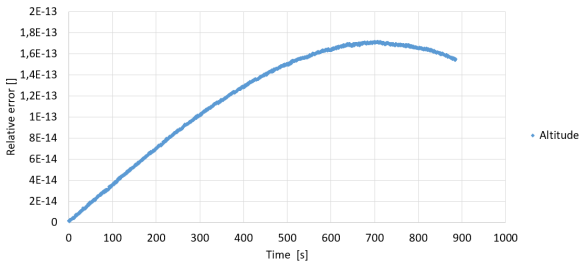

(a) Altitude relative error (Just Newton's law).

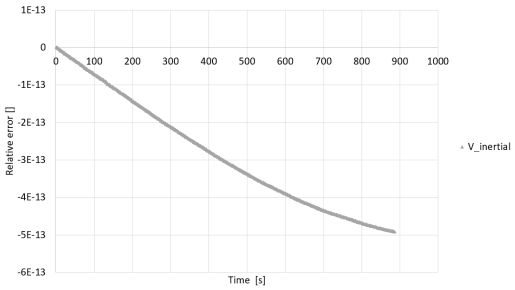

(b) Inertial velocity relative error (Just Newton's law).

Figure 4.3: Relative errors, (Part 1, just Newton's law).

The altitude chart shows an initially increasing trend and a late decreasing, however the order of magnitude is minimal for the whole trajectory, at a point accountable only to numerical differences.

The trend of the inertial velocity is instead just decreasing, with errors' magnitude going from 10^{-15} to 10^{-13} for both quantities.

Lastly, as already observed, the errors on the fixed velocity show how there is indeed a difference on its computation between the two software as the errors stay on the same order of magnitude, way higher than the ones of the other quantities.

The step size has been decreased to 0.1 s to see the influence on the propagation.

The maximum error decreased of two orders of magnitude, as it was expected, and the charts (Figure 4.5) show now trends that are more coherent with the hypothesis of numerical errors as, although an

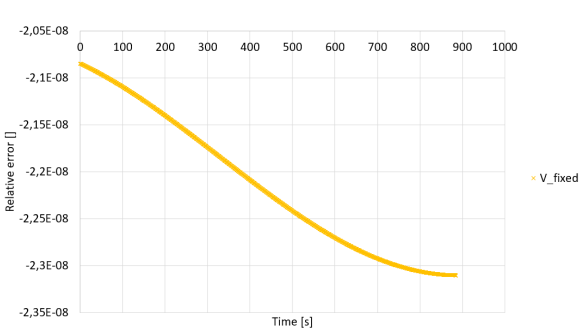

(a) Fixed velocity relative error (Just Newton's law).

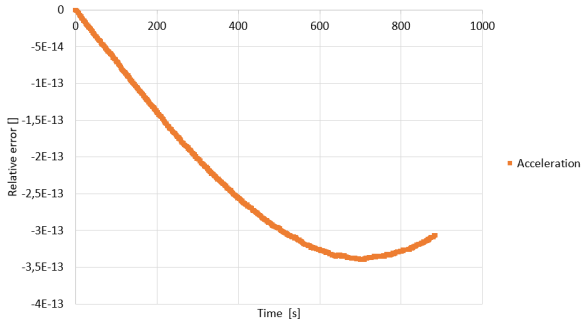

(b) Inertial acceleration relative error (Just Newton's law).

Figure 4.4: Relative errors (Part 2, just Newton's law).

overall increasing error is present, they present random fluctuations typical of these errors. Moreover, the orders of magnitude are always in the order of 10^{-15}, that is the last digit expressed by the double precision format, used both on GMAT and Octave, and present already on the first step.

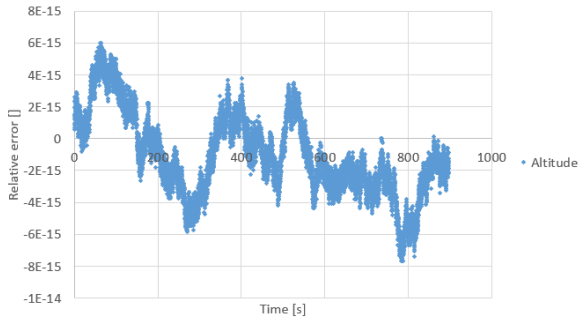

(a) Altitude relative error (Just Newton's law).

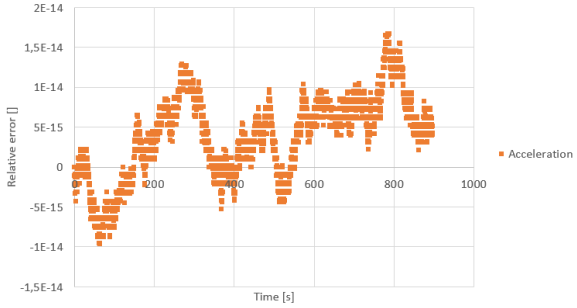

(b) Inertial acceleration relative error (Just Newton's law).

Figure 4.5: Relative errors with reduced step sizes, (Part 1, just Newton's law).

Although random fluctuations are present, the overall trend of the acceleration error is positive, and this is reflected on the velocity errors, that show again random fluctuations but with a more marked positive trend.

The errors have quantized values: the first error has a value of 1.2607e-15 and every other error is very close to a multiple of this value. Again, this is as well a typical behaviour of numerical errors of numerical integrations (Figure 4.6).

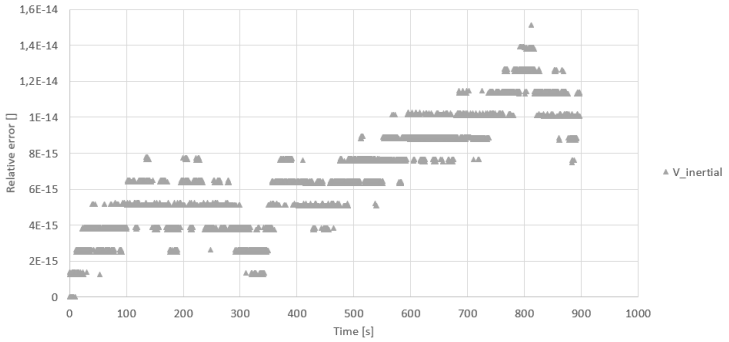

Figure 4.6: Relative errors with reduced step sizes, (Part 2, just Newton's law).

The fixed velocity had instead the same trend and with the same order of magnitude as before, and is therefore not reported.

4.2.2 J2 perturbation

As explained at the beginning of this section, the J2 perturbation is directly related to the latitude of the spacecraft and therefore some errors are already expected as the ones in the fixed velocity reported above.

On GMAT the propagator was updated imposing the earth as central body and not as point mass, giving it the JGM-2 gravitational model with degree 2 and order 0, to include just the J2 term.

Indeed, the maximum errors for altitude and inertial velocity increased of a factor of $\sim$ 4000 for altitude and velocity and of $\sim$ 16000 for the acceleration.

All the errors show now a similar trend to the fixed velocity one, with a different starting point, as the first errors have still a very low magnitude (Figure 4.7).

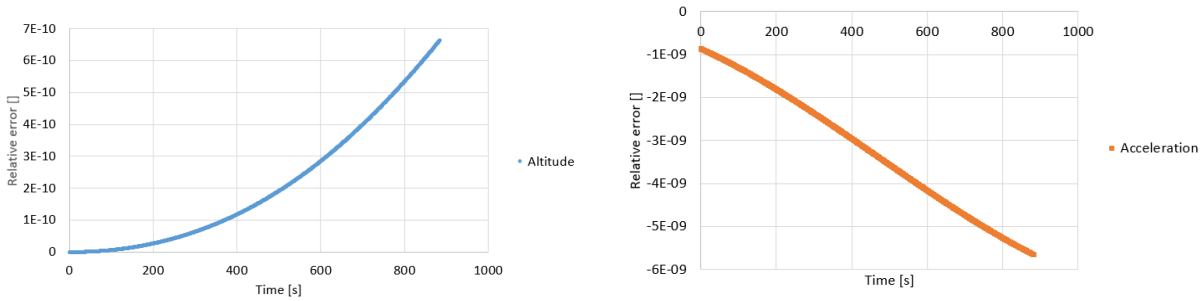

(a) Altitude relative error (Newton's law + J2).

(b) Inertial acceleration relative error (Newton's law + J2).

Figure 4.7: Relative errors (Newton's law + J2).

4.2.3 External bodies' perturbations

The influence of the Sun and the Moon on an entry trajectory is minimal due to the vicinity of the Earth that will predominate on the external bodies, however it is worth to see the effects of their presence on the

GMAT propagator was updated including the Moon and the Sun as point masses.

The effect on the maximum errors was more or less just a factor of 1.1, displaying the same trend on the acceleration and velocities, whose charts are therefore not reported.

The ephemeris file used has steps of 1 seconds, however, the earth's one has been obtained through GMAT itself, whose ephemerides have considerable numerical errors as also stated by their official documentation (GMAT, 2020).

Nevertheless, such a small change can definitely be accounted to numerical errors as the more computations are done with slightly different values, the more they add up giving different outputs.

Further in this section, a simulation with just external perturbations, without the J2 term, is reported for Venus.

4.2.4 Atmospheric model

During a reentry, the atmospheric drag is by far the most important term on the total deceleration, thus making the atmospheric model a key element of a propagator.

In GMAT the MSISE90 model is used, a model which comprises “all the major variations throughout the atmosphere including latitude, annual, semi-annual, and simplified local time and longitude variation” as in Hedin (1991).

The first comparison was made with the default earth model in $Freespace$, based on the MSISE00 model but at constant longitude, latitude, and time of the day. The errors on the accelerations were in the order of 10^0.

In order to decrease the error an ad-hoc atmospheric model has been derived from GMAT: a new output file with the atmospheric density at each step has been created and used to derive the density in function of the altitude for the propagator, specific for this entry trajectory. The used step size was 1 s.

The errors dropped of two orders of magnitude, but were still very high compared to the previous ones. Being the atmospheric density very sensitive to the altitude, its derivation from the model has been included in the intermediate steps of the propagator and not at each loop as it was before, leading to similar results.

The atmospheric model was refined simulating the trajectory with step sizes of 0.1 or 0.01 seconds and the comparison was run again giving almost the same results, suggesting how the errors did not arise from a poor atmospheric model.

The simulation was therefore repeated with fixed steps of 0.1 seconds both in GMAT and in the ATP code and the comparison was done again in the same way: the maximum errors were basically the same again; this behaviour was observed with every atmospheric model (1 s, 0.1 s, 0.01 s) and even decreasing further the step to 0.05 s.

It is likely that the error comes from a mixture of numerical and analytical errors. As said above there is a slight difference in latitude that will be reflected in small errors on the J2 perturbation and on the drag computation, however the entity of this error seemed, relative to the J2 term, negligible for short trajectories.

This is however not true for the drag term, but why? Plotting the relative error in density step by step and comparing it to the error in altitude reveals how they have the same exact trend but reversed: of course, since the atmospheric model returns the density in function of the altitude, an error on the altitude will result in an error on the density.

It is believed that there is a sort of “snowball effect” happening in which the numerical inconsistencies and the small error on the drag and J2 terms result in increasing errors in altitude, as already seen above, that in turn result in a bigger error on the density and therefore in even bigger errors on the accelerations and therefore on the altitude. This is confirmed also by the plots of the absolute error in altitude and inertial acceleration reported in Figure 4.8; the charts are relative to the simulations with 0.1 s step sizes and 0.01 s steps atmospheric model:

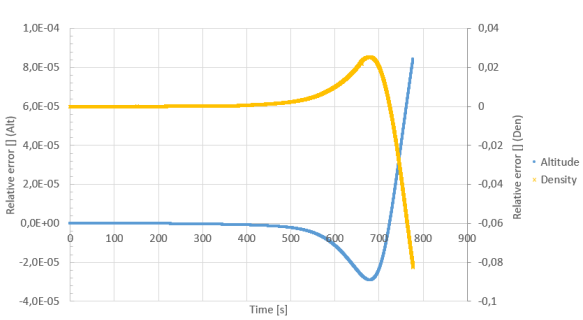

(a) Altitude and density relative errors (Every term).

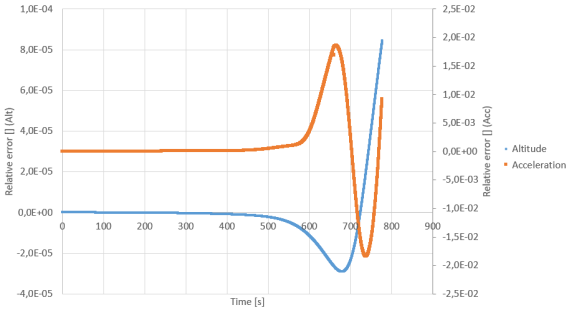

(b) Altitude and inertial acceleration absolute errors (Every term).

Figure 4.8: Influence of the atmospheric model.

Polar orbit

In order to verify if the reason behind these errors is the latitude error, a particular orbit was modelled on the two software: the only point where the inertial and fixed velocities are the same is along the spin axis. Assuming negligible movement of the axis within the time of an entry trajectory ($<$ 200 s for this specific one) and using a state vector of the form $[0, 0, Z, 0, 0, -v_z]$ the velocity will be the same between the two reference frames and, removing the J2 term, the trajectory should be completely vertical, thus removing every influence of the latitude on the trajectory.

Note that theoretically the J2 term should have influence just on the z-direction, therefore it could be included as well, however, since numerical errors could induce non-null x and y acceleration components, and therefore velocities and positions, it has been chosen to not include it to avoid further propagation of such errors.

The same state vector has been used in the two software, although this time the selected reference frame in GMAT was the $EarthFixed$ one; the step size was fixed to 0.1 s and the ad-hoc atmospheric model was created. The used state vector was: $[0, 0, 7000, 0, 0, -3]$ in km and km/s while the same Julian epoch was used.

The comparison of the two solutions showed how the difference at each step between inertial and fixed velocity was null for the ATP code while it oscillated between 7e-14 and 1e-13 for GMAT, thus confirming the hypothesis of null tangential velocity and therefore of null latitude influence. The initial error between the two fixed velocities gave a null difference at the first step.

Although the maximum errors on the quantities under study decreased by several orders of magnitude compared to the ones of the previous example, they were still considerable and showing the same trends even though the overall duration of the trajectory was much shorter (Figure 4.9a), confirming both hypothesis: the latitude plays a role in the errors, proved by the decrease in the maximum errors, and numerical errors increase exponentially when an atmospheric model is used. Moreover, the initial error on the acceleration was in the order of 10^{-11}, proving that there is no error in the calculations, but it is just a matter of numerical errors' accumulation.

Lastly the plot of the inertial acceleration absolute error versus the inertial velocity (Figure 4.9b) shows how of course once the velocity decreases, and so does the drag depending on the squared

velocity, the overall error on the acceleration starts decreasing being the drag less and less important.

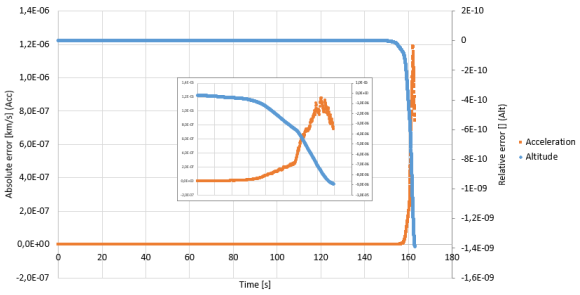

(a) Altitude and inertial acceleration absolute errors (Polar orbit without J2).

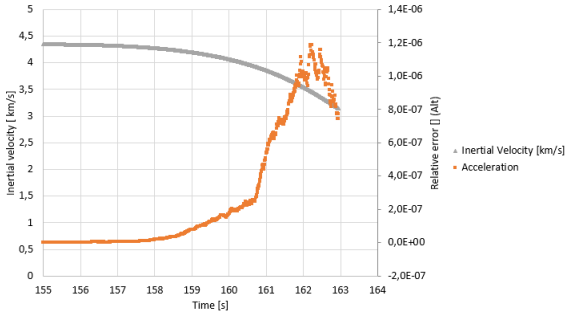

(b) Inertial acceleration absolute error versus inertial velocity (Polar orbit without J2).

Figure 4.9: Influence of the atmospheric model (Part 2).

It has been observed that, as with the step sizes, the initial position is always automatically changed by GMAT, including variations in the order of 10^{-13} to 10^{-16} to every component of the state vector, leading to slightly different trajectories. This influences as well the density model used, resulting in changes in the order of 10^{-8} on the density of the lowest part of the atmosphere that is likely contributing to the observed errors.

The maximum error on the acceleration, with step sizes of 0.01 s was in the order of 10^{-5} and therefore totally acceptable, thus confirming that the ATP code can be used alternatively to GMAT obtaining valid results.

4.2.5 Dormand-Prince method

Now that the ATP code has been validated in its analytical formulation, a validation of the adaptive step size using the Dormand-Prince method should be done.

This is a crucial part of the code as, with fixed step sizes of 0.01 seconds, it took more than 15 minutes to complete the simulation; the use of adaptive step sizes can help a lot reducing this time.

On GMAT the DormandPrince45 propagator has been chosen, and the error control $LargestState$ has been selected; the initial accuracy was set to $1e-10$. The same accuracy was set on the code, and both simulations were run using the conditions of the previous section. According to GMAT (2020) "$LargestState$ is the state vector component with the largest relative error measured with respect to the current state" therefore it should be computed as:

$$err_{GMAT} = max(\frac{|X_5 - X_4|}{|X_5 - X_{init}|}) \tag{4.1}$$

where X_5 and X_4 are the fifth and fourth order solutions and X_{init} is the current state vector. Note that GMAT (2020) talks about state vector component, and therefore suggests that the above equation is in vector form, and it is just the largest component of such vector to be used as error control.

This error control was found to be too much strict for the performance of the ATP code and therefore,

although mathematically incoherent, the following error control has been used:

$$err_{CODE} = max(\frac{|X_5 - X_4|}{|X_5|}) \tag{4.2}$$

Note that having adaptive step sizes and a different error control the comparison cannot be made step by step as in the previous sections, therefore the last step has been taken as testing point and a linear interpolation has been made on the ATP code solutions to be compared with the GMAT solutions at the same time. Moreover, the comparison of the step sizes revealed, as it was expected, how the selected error control was more loose than GMAT ones, having wider steps.

First the results of GMAT were compared to its own results using the fixed steps of 0.01 s showing relatively small errors with the same orders of magnitude as the ones obtained before, thus confirming again that errors of this order can come from numerical errors, even within the same software. Similar results were obtained for the comparison between the two adaptive solutions, with slightly lower errors, again reinforcing the hypothesis of numerical errors for the previous sections.

Lastly, the accuracy was reduced on the ATP code to 1e-8 making the computational time drop from more than 2 minutes to slightly more than 4 seconds; the solution was compared to the $1e-10$ GMAT one, showing errors just one order of magnitude higher than the $1e-10$ solution.

Comparisons between GMAT 1e-10 solution with 1e-12 solution gave similar results.

4.2.6 Venus trajectory

Lastly the validation has been made on Venus, using again a random entry trajectory, including the Earth's and the Sun's influences and the J2 term; the atmospheric model was not available on GMAT as already mentioned. The step sizes were set to 0.1 s.

The error on the acceleration was in the order of 10^{-6} at the first step, revealing the presence of errors in the computations.

The gravity model and the influence of external bodies were disabled, giving errors in the order of 10^{-12}, accountable to numerical errors. Then only the external bodies were enabled, leading to errors in the order of 10^{-10}, again reasonably accountable to numerical errors. The problem was therefore on the J2 perturbation.

The acceleration's components and the position vector were obtained from GMAT for each case in order to see the differences between the ones computed through the code's equations and the outputted ones.

The simulation with only Newton's law already showed discrepancies on the acceleration vector: it was not oriented as the position vector, although its magnitude was correct and the velocity vector at the following step was coherent with it being aligned with the position vector.

The acceleration vector was normalized, changed of sign and multiplied by the module of the position vector, thus obtaining the position vector $X_g^{'}$ theoretically used by GMAT to compute the acceleration

Including the J2 perturbation, the simulation was run again and the difference between the two acceleration vectors was obtained, giving the J2 perturbation vector.

As expected, trying to compute it with the real position vector gave considerable errors, while computing it with $X_g^{'}$ gave almost the same acceleration: it is now obvious that GMAT computes the acceleration using a vector in a different reference frame.

The used reference frame was the equatorial one, that is, for Venus, the same as the $BodyInertial$ one, and that has the same z position component as the body fixed one, resulting in the same latitude. This is also confirmed by the small errors in the fixed velocity, on the same order of the inertial one and from the output of the geodetic latitude, that coincides with the latitude computed as in Equation 3.5b.

Trying all the available GMAT reference frames, it was noticed how the $ICRF$ reference presents the same vector $X_g^{'}$ obtained before, showing how this is the reference frame used for the calculation of the acceleration vector. However, this reference is defined in a way that "the axes are close to the mean Earth equator and pole at the J2000 epoch" according to (GMAT, 2020) and therefore not referenced to the Venus equator.

Although this does not influence the magnitude of the Newton's acceleration or the external bodies' ones, it does influence the latitude and therefore the magnitude of the J2 perturbation, thus giving wrong results regarding Venus trajectories with enabled gravity model.

Nevertheless, on Venus the J2 term is three orders of magnitude lower than the Earth's one, explaining the small errors even though the increase in latitude between the two reference frames was of 13.86°.

The use of an atmospheric model would lead to analogous errors related to the latitude, however, as well as the J2 perturbation, the angular velocity of Venus is much smaller than Earth's one.

4.3 Parametric studies

Once the interplanetary trajectory has been determined and the ATP code has been validated, the study for the aerocapture mission can begin.

The first step of such a study is a parametric study to assess the influence of the various parameters playing a role in the trajectory and on the quantities under study, reported in Table 3.3.

The only force term not depending only on the state vector is the aerodynamic term that depends on the density and on the ballistic coefficient β; if the trajectory is ballistic just the drag will play a role, while lifting vehicles will produce lift as well, making the lift to drag ratio $\frac{C_L}{C_D}$ important as well.

The parameters of interest will therefore be: the initial state vector, the atmospheric density, the ballistic coefficient and the eventual lift to drag ratio.

4.3.1 Atmospheric model

As discussed in the previous section, the atmospheric model is a key of the propagator, as it influences highly the trajectory. Indeed, variations of the atmospheric density with the location can change the trajectory and should be taken into account on a preliminary study.

Figure 4.10 shows the used atmospheric model (Justh et al., 2021): between 250 and 150 km the

variations are in terms of SZA, as to say in terms of time of the day, while between 150 and 100 km only the difference between day and night side are considered. Lastly, small variations with the latitude are present on the lowest part of the atmosphere, but their magnitude is very low. The upper extreme corresponds to the day side, with a higher density, while the lower one is for the night side; the two curves converge at 100 km.

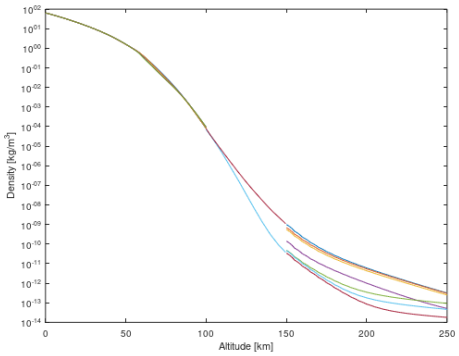

Figure 4.10: VenusGram atmospheric model.

Even though the variations for the upper atmosphere seem big, note that the scale is logarithmic and that the real values are extremely small, thus such differences are not likely to affect the trajectory so much.

What is more relevant is the homopause level (Table 2.1), that is much lower for the night side and therefore more difficult to reach. Preliminary parametric studies confirmed how the small differences between day side and night side were not justifying the choice of a night side sampling because of the reduction on the homopause level; the day side was therefore chosen as baseline for the study.

Assuming an entry in the day side, and considering that J2 perturbations, atmospheric tangential velocity effects and spatial variations of the atmospheric density are not really relevant for Venus, latitude longitude and velocity angle will not play a major role therefore at a fixed altitude the only two entry parameters relevant will be the entry velocity and the entry path angle, that are however an output of the interplanetary trajectory.

4.3.2 Ballistic coefficient and shape

The ballistic coefficient is the only parameter that can be chosen freely, as it depends only on the design.

It is given by the ratio between the mass, a design parameter, and the product between the drag coefficient C_D and the reference area S, both functions of the shape.

When designing an entry vehicle, it is good practice to choose shapes with a good heritage, in order to already have tables of aerodynamic coefficients and other useful data, limit further testing and remove associated risks. In this case the 45° sphere-cone has been chosen as it has been used in various past successful missions as Pioneer on Venus itself, Hayabusa re-entry probe or Galileo mission.

These shapes have all the same cone angle θ_{SC}, but differ between each other on the ratio between base radius and nose radius $Ra = \frac{R}{r_n}$. Moreover, defining a capsule density ρ_{SC} given by the total mass

of the entry vehicle over the volume of the sphere-cone (thus neglecting eventual back covers) one can relate the mass to the volume:

Table 4.7: Entry vehicle comparison (Takahashi and Yamada, 2018; D., 1973; Erb et al., 2020).

Capsule	Mass [kg]	θ_{SC} [°]	Nose radius r_n [cm]	Base radius R [cm]	$\frac{R}{r_n}$ Ratio	Volume V [m^3]	Density ρ_{SC} [kg/m^3]
Hayabusa	16.4	45	20	20	1	0.0073612	2227.89
Small Pioneer	63.6	45	16.7	33.65	2.015	0.0393093	1617.94
Large Pioneer	243.3	45	34.9	69.85	2.001	0.3514841	692.21
Galileo	337	44.86	22.2	63.2	2.847	0.2616916	1287.78
Average							1456.45

Of course this value serves just as rough order of magnitude and as expected is way higher than the maximum value reported for instance in Larson J. W. (1999) of 170 kg/m^3, being an entry vehicle more massive than a regular spacecraft.

As can be seen in Figure 4.11a, the sphere-cone geometry can be divided in two simpler geometries: a spherical cap and a truncated cone; the overall geometry is defined by three parameters only: the nose radius r_n, the ratio Ra and the cone angle θ_{SC}; since θ_{SC} is fixed to 45° it will just be function of r_n and Ra. It is assumed here that there is no curvature at the bottom of the conical section, and therefore the influence of this parameter has not been taken into account.

Without reporting the basic formulae of the volume of the spherical cap or of the truncated cone, the total volume of the sphere-cone can be computed as :

$$V = \frac{\pi}{3} r_n^3 \{[(1 - sen(\theta_{SC}))^2 (3Ra - 1 + sen(\theta_{SC}))] + [(Ra^3 - cos(\theta_{SC})^3) tan(\theta_{SC})]\} \tag{4.3a}$$

$$V = \frac{\pi}{3} r_n^3 (Ra^3 + (4.5 - 3\sqrt{2})Ra - 2.5 + \frac{3}{2}\sqrt{2}) \quad \theta_{SC} = 45 \tag{4.3b}$$

$$V = \pi r_n^3 (1 - \frac{\sqrt{2}}{2}) \qquad Ra = 1 \tag{4.3c}$$

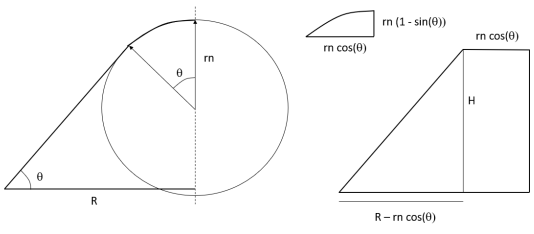

(a) Sphere cone secondary geometries.

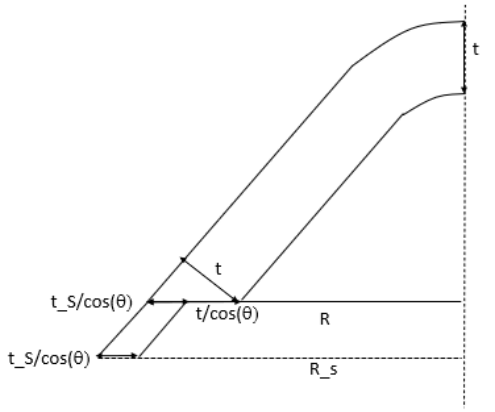

(b) TPS construction.

Figure 4.11: Sphere cone geometry and drag skirt.

Assuming that the geometries can be scaled without changing their aerodynamic coefficients that

therefore depend only on Ra, then the ballistic coefficient and the nose radius can be linked directly given such ratio and the spacecraft density.

In order to verify this assumption $Freespace$ has been used with a combination of nose radii between 0.01 and 1 m and radii ratios between 1 and 5, outputting the C_D at an altitude of 100 km giving the expected results but just with r_n higher than 0.2 m, reported in Figure 4.12a.

This can be explained considering that the C_D is a function of the shape and the regime, represented by the Knudsen number Kn. The C_D in continuum regime is just a function of Ra while in free molecular flow there are small variations of it with Kn but a correlation $C_D(H, Ra)$ could be found. The transitional C_D is instead given by a bridging function and is a function of Ra, r_n and Kn (Figure 4.13).

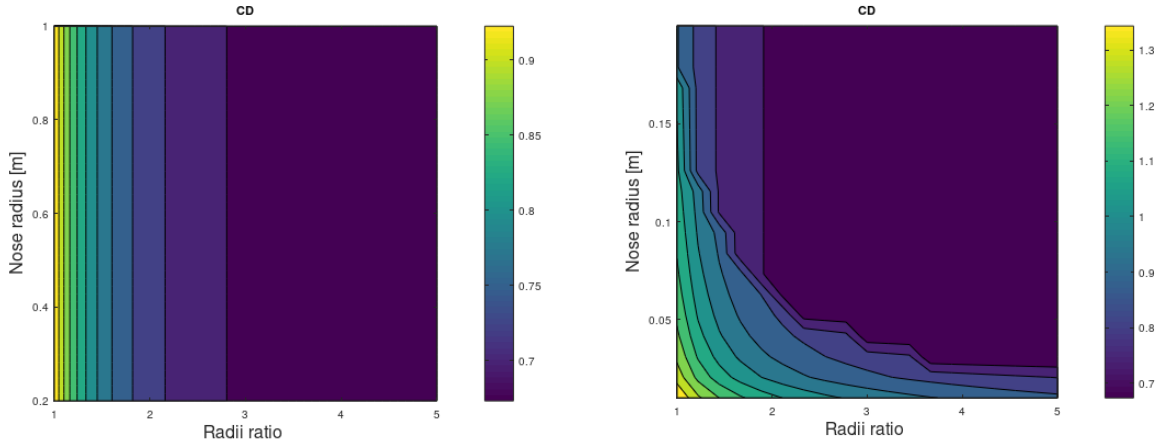

(a) 0.2 m $<$ Nose radius r_n $<$ 1 m

(b) Nose radius r_n $<$ 0.2 m

Figure 4.12: C_D in function of r_n and Ra.

The Knudsen number Kn is given by the ratio between the mean free path and the reference length of the body, that in this case is the axial height of the sphere-cone, that can be computed as $L_c = r_n(1-\sqrt{2}+Ra)$ for a 45° sphere-cone. The mean free path depends only on the atmospheric composition and therefore can be linked to the altitude.

Imposing Kn lower than 0.01, one can find the altitude representative of the onset of the continuum regime in function of the nose radius and the ratio Ra.

For a capsule with unitary ratio:

$$H = 2.9361 r_n + 99.42 \qquad r_n > 0.2 \tag{4.4a}$$

$$H = 3.8686 ln(r_n) + 105.9 \qquad r_n < 0.2 \tag{4.4b}$$

As the altitude used before for the calculations was 100 km, because representative of the usual periapsis of these trajectories, one finds a minimum nose radius of 0.1975 m. As it is shown in Figure 4.12b, increasing Ra the reference length L_c for the same nose radius increases, therefore the onset of the continuum regime is delayed.

As the continuum C_D is just function of Ra, a correlation between the two parameters has been investigated. The ratio Ra was changed between 1 and 5 with a fixed nose radius of 0.5 m first and 1 m

after.

Although the free molecular coefficient changes with Kn, the difference with respect to it within the free molecular range, is never higher than the 2%, therefore a similar methodology has been used for the free molecular flow as well leading to the following relations:

$$C_{Dco}(Ra) = 0.2855451Ra^{-2} + 0.6617892 \qquad Kn < 0.01 \tag{4.5a}$$

$$C_{Dfm}(Ra) = 0.1622506Ra^{-2} + 1.4423935 \qquad Kn > 10 \tag{4.5b}$$

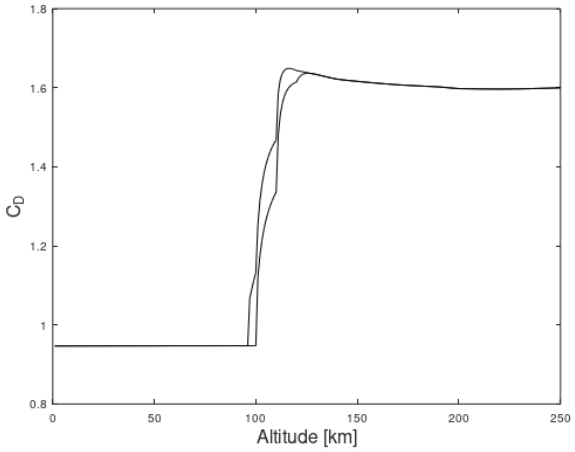

Figure 4.13: C_D in function of the altitude for different r_n but same Ra.

Note that even if the continuum regime is reached, the rest of the trajectory should have a different ballistic coefficient, however as in the free-molecular regime the density is lower, the drag should be lower as well and can, in a first approximation, be approximated with the continuum C_D. The effect of a variable C_D will be discussed in section 4.5.

Finally, using the relation $\beta = \frac{m}{SC_D}$ and substituting $m = \rho_{SC}V$ and $S = \pi r_n^2 Ra^2$ the following expression can be written for a 45° sphere-cone:

$$\beta = \frac{\rho_{SC}\frac{\pi}{3}r_n^3(Ra^3 + (4.5 - 3\sqrt{2})Ra - 2.5 + \frac{3}{2}\sqrt{2})}{\pi r_n^2 Ra^2 C_D(Ra)} \tag{4.6a}$$

$$\frac{\beta}{r_n} = f(Ra, \rho_{SC}) = \frac{\rho_{SC}}{3}\frac{(Ra^3 + (4.5 - 3\sqrt{2})Ra - 2.5 + \frac{3}{2}\sqrt{2})}{Ra^2 C_D(Ra)} \tag{4.6b}$$

This last equation reveals that higher is the ratio Ra higher is the ratio $\frac{\beta}{r_n}$, resulting in smaller nose radii for the same ballistic coefficient, while lower is the density, lower is the ratio (Figure 4.14a).

Obtaining the mass from the ballistic coefficient through $m = \beta SC_D$ one can write:

$$\frac{m}{\beta^3} = f(Ra, \rho_{SC}) = pi(\frac{\beta}{r_n})^{-2} Ra^2 C_D(Ra) \tag{4.7}$$

This equation tells how smaller ratios Ra will need greater masses to have the same ballistic coeffi-

cient, but higher capsule densities will mitigate this effect (Figure 4.14b).

Lastly, of course one can relate the last two equations to find $\frac{m}{r_n^3} = f(Ra, \rho_{SC})$: higher Ra will result in smaller nose radii for the same mass, and higher densities will help decreasing it further (Figure 4.15a).

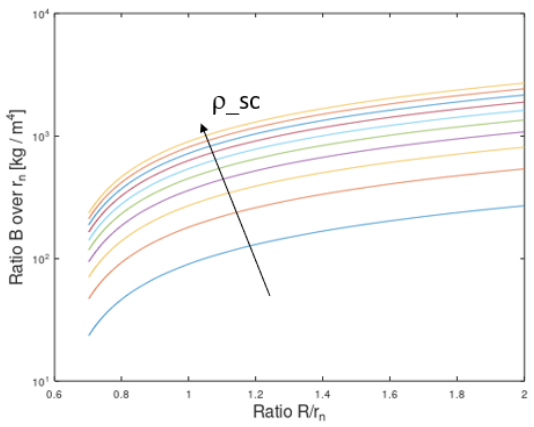

(a) Ratio β over r_n [kg/m^4].

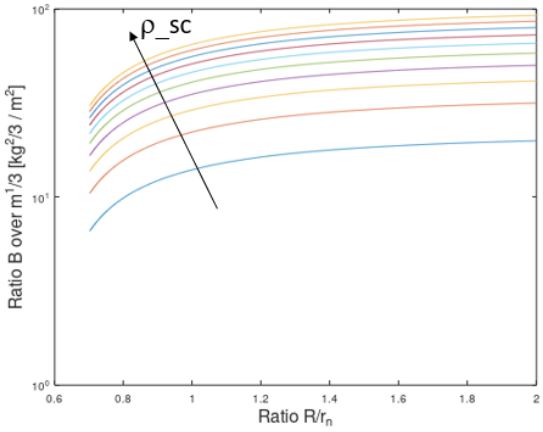

(b) Ratio β over $m^{\frac{1}{3}}$ [kg$^{\frac{2}{3}}$/m^2].

Figure 4.14: Relations between ballistic coefficient and mass or nose radius.

4.3.3 Nose radius and thermal loads

As the thermal loads are one of the drivers of an entry mission, a deep consideration should be done on the thermal design of the capsule. Assuming the use of an ablative TPS, the type of used material will depend on the peak heat flux, while the thickness of the shield will depend on the total heat load.

Since the heat fluxes are related to the nose radius, it is really important to adjust it to the expected environment. Looking at Equation 3.37 (assuming it can be used in free molecular flow as well) and Equation 3.38 it is easy to see how the convective heat fluxes depend on $r_n^{-0.5}$ while the radiative ones depend on $r_n^{0.49}$: if the convective fluxes will be predominant, a bigger nose radius is wanted, while if radiative fluxes will be higher, then a smaller radius would be more suitable. It is expected that for aerocapture manoeuvres convective heat fluxes will be predominant, and therefore bigger nose radii will be preferred.

Given a certain material of density ρ_{TPS}, the mass of the TPS will be a function of the thickness t and of the sphere-cone geometry in use; for the specific case of θ_{SC} 45°, the mass will be just a function of the thickness, the nose radius r_n and the ratio Ra.

Imposing a maximum mass fraction of the TPS over the total mass, one can therefore find the maximum thickness for a given material and shape; Wright et al. (2011) give a correlation between such mass fraction and the heat load, however the goal of this consideration is to determine the maximum allowable heat load for a given β as the same thickness for a larger capsule will result in a more massive TPS, but if compared to the higher mass, the mass fraction could be higher or lower.

Applying Equation 4.3c to a 45° sphere-cone with $r_n' = r_n - t$ and $Ra' = \frac{Ra r_n - t\sqrt{2}}{rn - t}$, (Figure 4.11b) one can compute the TPS volume as $V - V'$ and for a given TPS density ρ_{TPS} one obtains a function

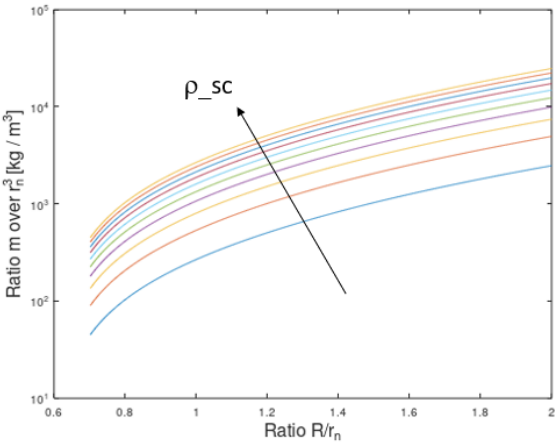

(a) Ratio β over r_n^3 [kg/m^3] .

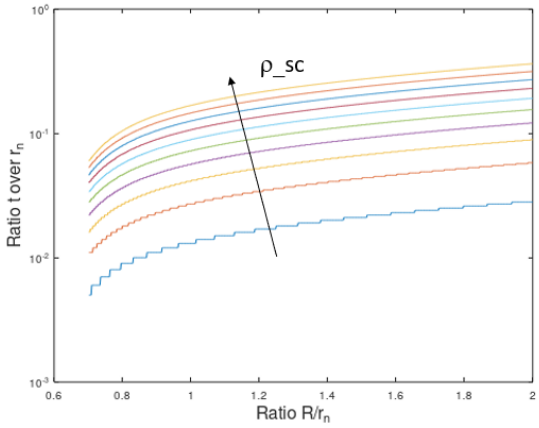

(b) Ratio t over r_n [/].

Figure 4.15: Relations between mass or thickness and nose radius.

$MF = f(Ra, \frac{t}{r_n}, \rho_{SC})$:

$$MF = 100\frac{\rho_{TPS}}{\rho_{SC}}(1 - \frac{\pi}{3}(1 - \frac{t}{r_n})^3((\frac{Ra - \frac{t}{r_n}\sqrt{2}}{1 - \frac{t}{r_n}})^3 + (4.5 - 3\sqrt{2})\frac{Ra - \frac{t}{r_n}\sqrt{2}}{1 - \frac{t}{r_n}} - 2.5 + \frac{3}{2}\sqrt{2}) \tag{4.8}$$

Of course in case different materials want to be investigated this equation can be linked to $\frac{\rho_{SC}}{\rho_{TPS}}$ instead of ρ_{SC} alone.

This equation cannot be inverted generically to obtain the mass fraction and must be solved numerically, giving a relation $\frac{t}{r_n} = f(Ra, \rho_{SC}, MF)$. Moreover, if one uses the relations of the previous section, functions $\frac{t}{\beta} = f(Ra, \rho_{SC}, MF)$ and $\frac{t}{m^{\frac{1}{3}}} = f(Ra, \rho_{SC}, MF)$ can be found.

Solving these relations numerically for a target mass fraction using the density of PICA, an ablative material that can be used for $\dot{q}$ up to 12000 kW/m^2, of ρ_{TPS} 274 kg/m^3 (Sepka and Samareh, 2015), it was noticed how lower ratios and higher densities have higher $\frac{t}{\beta}$ for every mass fraction, meaning that a capsule with the same ballistic coefficient allows a higher TPS thickness although keeping the same ratio between the TPS mass and the total mass (Figure 4.16a).

In an analogous way, higher ratios and higher densities will have higher $\frac{t}{r_n}$ and therefore should be preferred for the thermal design as the same r_n will give the same HL but a higher t could be achieved with the same mass fraction (Figure 4.15b).

When considering however the function $\frac{t}{m^{\frac{1}{3}}} = f(Ra, \rho_{SC}, MF)$, it was noticed that the curve did not have a general increasing or decreasing trend but had a maximum, depending on the three variable of interest (Figure 4.16b and Figure 4.17a).

Using different target mass fractions, the optimal Ra for different $\frac{\rho_{SC}}{\rho_{TPS}}$ have been found and plotted. The result showed how the optimal Ra was lower for lower densities ratios and lower target mass fractions, near a value around 1.3 – 1.4 for all the mass fractions below 5% (Figure 4.17b).

Therefore, higher ratios will help to achieve higher ballistic coefficients with the same mass and therefore lower mass fraction for the same thickness, however $\frac{t}{m^{\frac{1}{3}}}$ will have an optimum and therefore

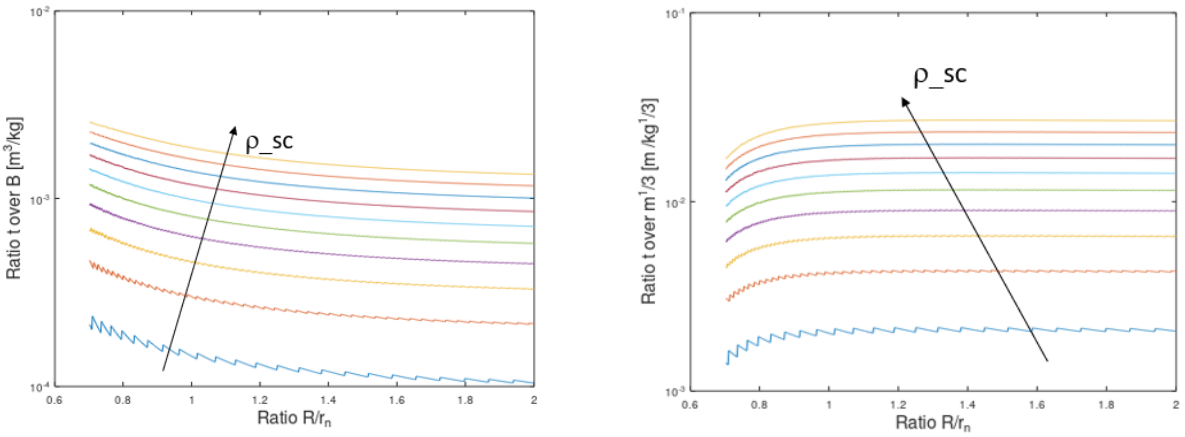

(a) Ratio t over β [m^3/kg] .

(b) Ratio t over $m^{\frac{1}{3}}$ [m/kg$^{\frac{1}{3}}$].

Figure 4.16: Relations between thickness and ballistic coefficient or mass.

increasing Ra too much could lead to a lower thickness for the same mass.

Most important, higher ratios and higher β will reduce the nose radii and therefore one must be careful with the associated heat fluxes: pushing the ratio too much might result in an increase of the heat fluxes not justified by the gain in thickness.

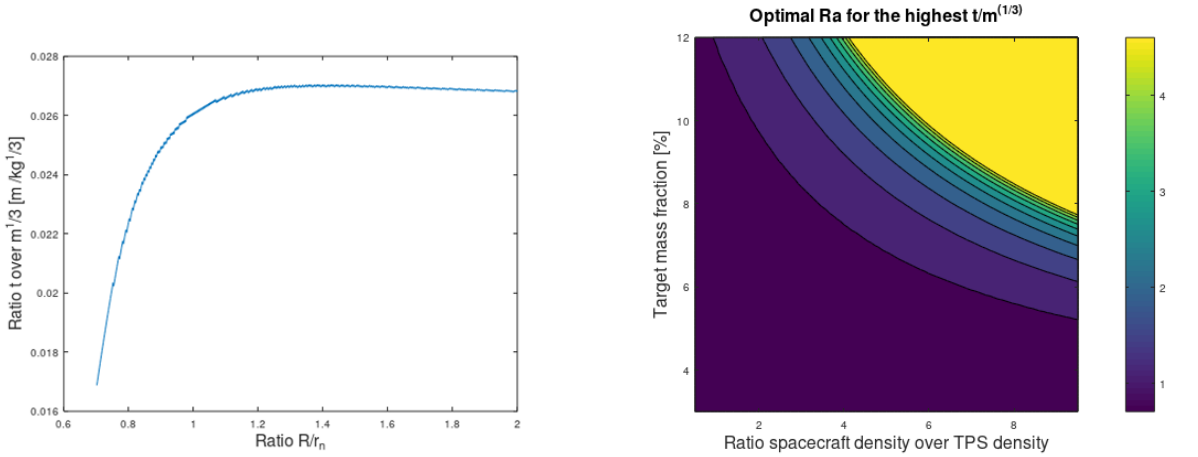

(a) Ratio t over $m^{\frac{1}{3}}$ [m/kg$^{\frac{1}{3}}$].

(b) Optimal ratio Ra for the highest ratio of thickness over mass.

Figure 4.17: Relations between thickness and mass.

Sepka and Samareh gives correlations between the thickness and the ratio of heat load over squared entry velocity $\frac{HL}{v_0^2}$, therefore with a given entry velocity, there will be a direct correlation between heat loads and TPS thickness t.

The question arises naturally: can one relate the nose radius and the heat load? The heat load is the integral of the heat fluxes over time and can therefore be written as:

$$\text{HL} = \int_{t_0}^{t_{ex}} k_1 V(t)^3 \rho(t)^{0.5} r_n^{-0.5}\, dt + \int_{t_0}^{t_{V<V_x}} k_2 V(t)^{18} \rho(t)^{1.2} r_n^{0.49}\, dt + \int_{t_{V<V_x}}^{t_{ex}} k_3 V(t)^{7.9} \rho(t)^{1.2} r_n^{0.49}\, dt \quad (4.9)$$

where for Venus k_1 is 1.896e-7, k_2 is 8.497e-66 and k_3 is 2.195e-25 (to have the HL in kJ/m^2) and V_x is 10.028 km/s.

As the integrals depend on the evolution of the trajectory in time, and therefore on entry conditions, ballistic coefficient, atmospheric model, eventual lift or drag modulations, etc. they cannot be determined a priori and can just be computed from simulated trajectories. Once a trajectory has been computed, the nose radius, constant in time, can be taken out of the integral and a relation $HL = f(r_n)$ can be derived for each specific trajectory.

Computing the derivative of the equation above and making it equal zero, one find the optimal nose radius for a specific trajectory as:

$$r_{n_{Opt}} = \left(\frac{1.0204 k_1 \int_{t_0}^{t_{exit}} V(t)^3 \rho(t)^{0.5}\, dt}{k_2 \int_{t_0}^{t_{V=10.028}} V(t)^{18} \rho(t)^{1.2}\, dt + k_3 int_{t_{V=10.028}}^{t_{exit}} V(t)^{7.9} \rho(t)^{1.2}\, dt}\right)^{0.99} \tag{4.10}$$

Lastly, using the correlation of Sepka and Samareh (2015) one obtain for v_0 10.856 km/s:

$$t = 0.029676 HL^{0.1873} \tag{4.11}$$

where HL is in kJ/m^2 and t in m.

Note that this correlation has been derived for Earth and therefore is not totally suitable for Venus as the different external conditions and atmospheric compositions may cause different effects on the TPS even with the same heat loads.

However, once the shield starts ablating, an exiting mass flow rate of ablated material will begin: it can be assumed that the external conditions will be just a function of the TPS itself and therefore that it will behave similarly on different atmospheres as well.

In order to use PICA, all the trajectories with $\dot{q}$ higher than 12000 kW/m^2 will be discarded to avoid using heavier TPS. Note that lighter TPS materials exist, but are suitable for applications with much lower peak heat fluxes, as the after-body of the capsule (section 4.4.1).

To summarize, given a 45° sphere-cone geometry, one can find relations between the nose radius, the ballistic coefficient and the spacecraft mass in function of the spacecraft density and the ratio Ra. Moreover, these quantities can be related to the TPS thickness to find its mass related to the overall mass.

Higher ratios will result, for the same ballistic coefficients, in smaller nose radii but lower thickness for the same TPS mass fraction, however to achieve such ballistic coefficients a smaller mass will be needed: an optimum cannot be found as all the parameters influence each other and a direct correlation between nose radius and heat fluxes cannot be achieved as the integrals in its computation depend on the specific trajectory.

However, the trajectory calculation depend only on the entry conditions and the ballistic coefficient and can therefore be made without such correlations.

For a given trajectory one can have $HL = f(r_n)$ and $t = f(r_n)$ resulting in $\frac{t}{r_n} = f(r_n)$; moreover, as the trajectory depends on β, a given trajectory will have a given β and therefore: $m = f(Ra, \rho_{SC})$, $r_n = f(Ra, \rho_{SC})$, resulting in $\frac{t}{r_n} = f(Ra, \rho_{SC})$ and therefore $MF = f(Ra, \rho_{SC})$.

Once the trajectory is computed, changing Ra and ρ_{SC} one can find the mass of the spacecraft and its nose radius, thus post-processing heat loads and heat fluxes obtaining the needed TPS thickness that can be related to the found geometry and mass to find the TPS mass fraction.

Limiting the total mass of the spacecraft and its density, one can find a range of these quantities that allow the selected ballistic coefficient, the maximum MF and maximum peak heat flux.

4.3.4 Constraints

Several constraints were put on the trajectories in order to delineate a frame of validity on the obtained results. The following trajectories were discarded:

- Entry trajectories, as aerocapture manoeuvres are wanted.
- Trajectories with the periapsis higher than H_{max}, due to scientific limitations.
- Trajectories with ΔV lower than ΔV_{min}, in order to be captured.
- Trajectories with peak heat flux $\dot{q}$ higher than $\dot{q_{max}}$ for TPS limitations.
- Trajectories with heat load HL higher than HL_{max} for TPS limitations.
- Trajectories with peak deceleration acc higher than acc_{max} for structural limitations.

The values of H_{max} and ΔV_{min} have already been discussed and are respectively 107 km and 800 m/s.

The value of $\dot{q_{max}}$ has already been reported and is equal to 12000 kW/m^2. The heat load will be a function of the selected maximum MF and will be related to the spacecraft density and ratio used, varying for each ballistic coefficient.

According to Wright et al. the TPS mass fraction for Pioneer Venus was around 11-12%, while almost no mission had fractions higher than 20%. However, one must keep in mind that those were all entry missions and more severe thermal environments are expected in those cases: a mass fraction of 5% was arbitrarily chosen for this study.

The value of acc_{max} cannot be related to the structural mass fraction, since it is very difficult to find correlations between the structural loads and the structure thickness or weight. As the maximum quasi static load of the launcher is 6 g according to Laiger (2021) and the spacecraft will be dimensioned for this value anyway, it can give a lower bound of the maximum allowable deceleration. An arbitrary value of 10 g has been selected as acc_{max}.

Note that while the limitations on periapsis, ΔV and avoidance of entry trajectories are necessary for the mission concept, all the other ones are just arbitrary design choices and could be changed making different choices as a different TPS technology or allowing higher TPS mass fractions or higher structural loads. The ΔV as well could be reduced assuming a propulsive subsystem is present after the manoeuvre in order to compensate for the missing ΔV, however it would reduce the advantages of an aerocapture.

4.3.5 Parametric simulations

As it is impossible to find the optimal ratio Ra and spacecraft density ρ_{SC} before computing the trajectories, a unitary ratio and the average density in Table 4.7 have been used to derive relations between β and r_n and the maximum heat loads for each ballistic coefficient. The heat load and heat fluxes limitations will be reported as well to give an idea of their influence on the results, although they will change modifying the ratio Ra and the spacecraft density.

In case of unitary ratio, for a 45° sphere-cone $C_{Dco}(1)$ 0.9473 and using ρ_{SC} 1455 kg/m^3 one obtains $\beta \simeq 450 r_n$ and $m \simeq 1340 r_n^3$.

It is unbelievable to have a ballistic coefficient higher than 500 kg/m^2 for an unmanned mission as the mass would probably be too high, a value that has been selected arbitrarily as upper bound for β.

The following simulations have been done in terms of ballistic coefficient and entry angle: the initial entry angle was set as $\pm$ 1° with steps of 0.1° from the arrival value while the ballistic coefficient was set to vary between 0 and 500 kg/m^2 with steps of 50 kg/m^2 (the first value was replaced with 1 kg/m^2). The 5th order embedded method has been used, and the accuracy was set to 1e-6 as in this case computational speed is preferred over results precision and the results will be post-processed with greater accuracy.

For the first simulation, only a ballistic trajectory has been considered, without drag modulation and with null $\frac{C_L}{C_D}$; the ballistic coefficient was considered constant along the whole trajectory. Since the solutions were very different and no succeeded solution was achieved, the first value (1 kg/m^2) was excluded for the following simulations.

The first noticeable output was that no trajectory succeeded with an entry angle rotation of -0.4° or lower, corresponding to an entry angle of $\sim$ -9.52°.

The constraint on the ΔV was added to the results, revealing how all the trajectories with angle rotations higher than 0° had ΔV too small to be captured. The simulation was therefore repeated within these angles with steps of 0.02°.

Again no trajectory with rotations of -0.38° or lower succeeded, but now a better view of the corridor was achieved. The corridor had a width of 0.1° for every ballistic coefficient, but with different extremes: for instance at β 50 kg/m^2 the corridor was between -0.06° and -0.16° while at β 500 kg/m^2 it was comprised between -0.26° and -0.36°.

Note that imposing the periapsis limitation corresponding to the night sampling (101 km) 10/58 solutions would have been excluded, reducing the corridor of lower ballistic coefficientsThe limitation of 107 km did not exclude any solution.

When including the limitation on the maximum heat load, all the solutions with β 50 or 100 kg/m^2 were discarded, while the 150 kg/m^2 corridor was reduced to a single solution.

Entry Velocity scale factor

As the entry velocity determines the initial energy of the entry vehicle, one can expect that an acceleration at the atmosphere top would result in a corridor increase as some trajectories falling to the

ground would now manage to escape the planet. A factor of 1.01 has been imposed to the entry velocity, corresponding to a ΔV of $\sim$ 100 m/s and the simulation has been repeated. The limit ΔV_{min} has been increased of 100 m/s, while the heat load limitation was not changed.

After readjusting the angles similar results were found: again the initial corridors were of 0.1°, but were now even steeper, with an increase of 0.1° for each value. To compare with the previous ones, at β 50 kg/m^2 the corridor is between -0.16° and -0.26° while at β 500 kg/m^2 it is comprised between -0.36° and -0.46°. Now, only 9 solutions were above 101 km. When the extra limitation on the ΔV was added, three more solutions were excluded; again the effect of the heat load limitation was the same but excluding some solutions up to 200 kg/m^2.

Apparently the hypothesis of steeper trajectories now managing to escape the planet was right, but some of the trajectories that were captured before, have now too high exit velocities, thus basically not changing the corridor width. Moreover, the extra ΔV required excluded more solutions, reducing even more the corridor width.

A scale factor of 0.99 was tried as well, with the idea of reducing the velocities and therefore heat fluxes, heat loads, and the needed exit ΔV. Indeed, the solutions were better than the previous ones as some trajectories with β 150 kg/m^2 now succeed, however the corridor width for higher β did not change.

Lifting trajectory

A non-null $\frac{C_L}{C_D}$ ratio has been given to the probe as it helps to exit the planet providing lift, hoping to increase the corridor width. A low and mid $\frac{C_L}{C_D}$ have been imposed, fixed along the whole trajectory, equal to 0.3 and 0.5 reference values taken by Gong et al. (2020) that classifies low ratios as 0.3 and mid ratios as 0.5-0.7.

It is assumed here that the lift can be provided without changing shape, C_D, mass and so on, keeping the same limitations in terms of structural and thermal loads. Of course, this is unrealistic because a lifting vehicle will have stricter limitations in terms of loads if lifting elements as flaps are used. Moreover, the drag coefficient would change, as well as making useless all the correlations obtained above for 45° axisymmetric sphere-cones, especially in case instead of lifting elements, lift is provided through an off-set of the centre of pressure, achievable only without an axisymmetric shape.

Interesting results were found when lift was introduced: the initial corridor was much wider for both solutions, around 1° for $\frac{C_L}{C_D}$ 0.5 and around 0.4° for $\frac{C_L}{C_D}$ 0.3.

The peak heat fluxes and heat loads are now smaller, but why? If one imagines the velocity vector and the aerodynamic forces, introducing lift one should have higher velocities along the whole trajectories as the perpendicular component of the aerodynamic force will increase the velocity in respect to the only drag situation; higher velocities should give higher heat fluxes and therefore higher heat loads (assuming the duration of the trajectories is comparable).

Indeed, comparing solutions with the same β and same γ, but with $\frac{C_L}{C_D}$ respectively 0 and 0.5, the ΔV is more than 2 km/s lower for the lifting vehicle. However, the periapsis, in this case, is more than 3 km above, and therefore with a lower density.

Considering just convective heat fluxes, from Equation 3.37 since K and r_n are equal, in order to

have lower peak heat fluxes one can impose:

$$\sqrt{\rho_1}V_1^3 > \sqrt{\rho_2}V_2^3 \Rightarrow \frac{V_2}{V_1} < \frac{\rho_1}{\rho_2}^{\frac{1}{6}} \tag{4.12}$$

and, substituting the densities of the two periapsis one find that the velocity is the second case should be 1.17 times higher than the first one, while it is only 1.12 times higher. Doing the same for radiative heat fluxes, the ratio should be higher than 1.15 therefore explaining the lower peak heat fluxes.

With $\frac{C_L}{C_D}$ 0.3 the heat fluxes are even lower, increasing for instance the corridor at β 150 kg/m^2 from 0.04° ($\frac{C_L}{C_D}$ 0.5) to 0.12°.

The major limitation in this case is indeed the maximum acceleration. When introducing it, the corridor widths were reduced to 0.32° for β 350 kg/m^2 and 0.36° for β 500 kg/m^2 for both $\frac{C_L}{C_D}$. Although a higher lift increased the corridor even up to 1°, it induced of course higher loads on the spacecraft, thus leading to similar corridors for this design choice.

Of course, removing the limitation on the deceleration and therefore allowing for higher loads and heavier structures, the corridor width can be increased a lot providing lift. Imposing a maximum deceleration of 15 g, the corridor width was 0.6°for $\frac{C_L}{C_D}$ 0.5.

Using the mid lift to drag ratio, two more simulations have been done using it just before (from the top of the atmosphere) the altitude of 105 km or just after (until the exit of the atmosphere).

The case with lift just before 105 km showed results very similar to the basic case, with higher periapses and lower thermal loads, but much lower ΔV.

The case with lift just after 105 km had basically the same corridor widths as the case with lift along the whole trajectory but, comparing the same entry conditions, had lower periapsis and therefore higher decelerations, peak heat fluxes, heat loads, but with greater ΔV. Some solutions not acceptable before because of the ΔV were now acceptable, while some of the steepest ones had now decelerations too high to be acceptable.

Pushing the altitude to 100 km, again similar corridor widths were found at the higher β, while the heat load limitation reduced the width at lower β.

Drag Modulation

A modern concept in aerocapture studies is the drag modulation: dropping the back part of the capsule, called “drag skirt” in the middle of the trajectory will reduce the reference area thus reducing the drag letting more trajectories exit the atmosphere and reducing structural loads.

This can be modelled easily, increasing the ballistic coefficient at a certain point of the trajectory through a ratio $\frac{\beta_2}{\beta_1}$.

At first, it was imposed a ratio of 2, at the periapsis, however the results were similar to the situation without drag modulation: the trajectories falling before were falling now too as no periapsis was reached, some actually managed to perform the modulation and escape but some of the ones with smaller angles had now less drag and therefore less ΔV. The corridor widths were basically the same, slightly milder heat loads were present.

The event was now set to be activated at the altitude of 105 km. Again a similar corridor was achieved, with smaller decelerations, all the other parameters were similar.

Decreasing the altitude to 100 km, more trajectories fell, thus reducing the corridors.

The ratio was increased to 5 and 10 keeping the altitude of 105 km, resulting in smaller corridors because of the too small ΔV; with the ratio of 10 no trajectory succeeded.

Mixed trajectories

The two events have now been mixed together in order to try to take the advantages of both.

The lift was increasing a lot the corridor width and decreasing the heat loads, however the structural loads were huge and therefore limiting the applications of this technology, although the best one in terms of corridor width; the ΔV was reduced.

The drag modulation helped with some steeper trajectories, but reduced also the decelerations, because of the greater ballistic coefficients, in this case again the ΔV was reduced.

Mixing the two technologies, one could have wider corridors because of the smaller decelerations, but even smaller ΔV limiting this application. Moreover, keeping the same lift to drag ratio, but doubling the ballistic coefficient, will result in less drag and therefore in less lift.

At the beginning, the lift was induced ($\frac{C_L}{C_D}$ 0.5) from the top of the atmosphere, imposing the drag modulation at 105 km first and 100 km after.

Compared to the solution with only lift, the deceleration were now lower, but so were the ΔV thus not changing much the corridor. Now at higher β problems related to the peak heat flux arose: both the lift and the drag modulation increase the periapsis velocity, thus resulting in higher heat fluxes.

The solution with modulation at 100 km has slightly lower heat fluxes and decelerations.

As the two events might be related, imagine instead of dropping a part of the capsule, to rotate it around one of the transversal axis, and therefore have a second configuration with lift and a different C_D, or a mix of the two technologies: first a rotation and then a drop. The lift imposing and the drag modulation have been done again at the same altitudes of 105 and 100 km. The solutions with one at 100 and the other at 105 km have been tried as well.

It was noticed that all the simulations had similar corridors, however the simulations with lift induced later had a lower periapsis and therefore higher fluxes. Regarding the simulations with lift at 105 km, again it was confirmed that later drag modulation was better.

Compared to the only lift simulation, at low β the heat loads were higher and reducing the corridor, while at higher β the same problem was showing in terms of peak heat flux. At mid β the thermal loads were still acceptable and the decrease in deceleration was actually slightly increasing the corridor.

To avoid the decrease in lift due to the drag modulation now the simulation has been repeated with $\frac{C_L}{C_D}$ 0.5 before 105 km and 1 after, and then with $\frac{C_L}{C_D}$ 0.3 before and 0.6 after 100 km. Again, at higher ballistic coefficients, the only lift case was better because of the even higher heat fluxes. At medium ballistic coefficients, the corridor was slightly wider for both $\frac{C_L}{C_D}$ ratios.

The drag modulation has been pushed even more to 95 km for both ratios, as it seems that the later it is done, the better it is for the peak deceleration and thermal loads. The corridor increased for every

ballistic coefficient. Now at β 200 kg/m^2 some solutions have been found with corridors of respectively 0.24° and 0.36°.

The ratio $\frac{\beta_2}{\beta_1}$ has now been increased to 3, keeping the same lift conditions.Now the corridor for the lower lift has decreased at higher ballistic coefficients because of the heat fluxes, while it increased slightly at β 250 and 300 kg /m^2. The high lift now causes ΔV problems at higher β while increases further the corridor at mid β.

Lastly, a factor of 0.99 has been imposed again to the entry velocity to reduce thermal and structural loads and to reduce the required ΔV. The corridors at low and mid ballistic coefficients increased again, while the same ΔV problems happened at higher ballistic coefficients.

The last simulation was done with $\frac{C_L}{C_D}$ of 0.5, but just above 105 km, for both the descending and ascending part of the trajectory, in order to avoid the peak decelerations around the periapsis, but a lot of trajectories were now falling.

All the simulations conditions are summarized in Table C.1 in Appendix C, where also all the obtained results are reported for the test cases of β 350 and 500 kg/m^2 (Table C.2 and Table C.3).

Mixing technologies as lifting vehicles and drag modulation, the corridor width was increased from 0.1° for the default trajectory to 0.72° for β 300-350 kg/m^2 using a $\frac{C_L}{C_D}$ of 0.5 before 105 km and 1 after, while the drag modulation is performed at 95 km with a ratio $\frac{\beta_2}{\beta_1}$ of 3 (Figure 4.18).

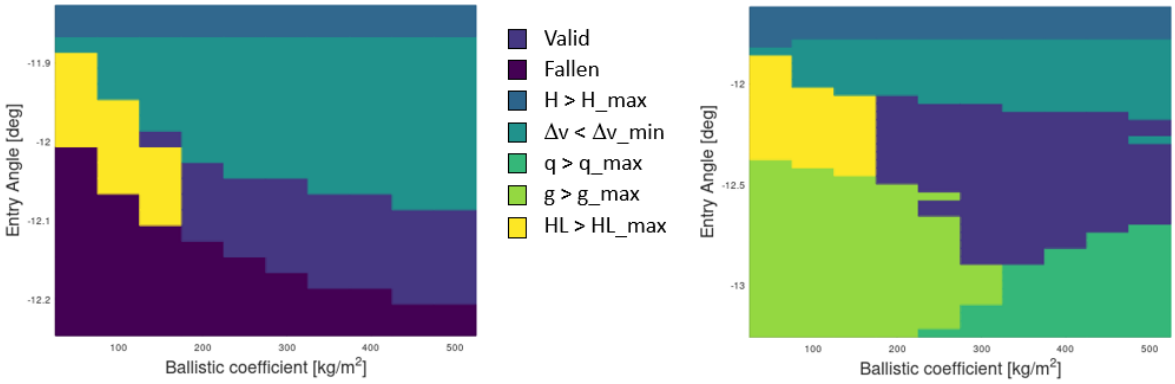

Figure 4.18: Comparison between simulations 1 (left) and 27 (right) (Table C.1).

The results of this study can be summarized as:

- An acceleration prior entering seems advantages-less.
- A deceleration can instead mitigate thermal and structural loads. Fuel is required though, while an aerocapture is supposed to avoid it.
- Providing lift increases the corridor saving falling trajectories.
- Too much lift will cause less ΔV and therefore higher periapsis velocities, resulting in higher thermal and structural loads.
- The lift increases the periapsis altitude, thus mitigating the effects of the previous point.

- Drag modulation reduces structural loads if performed before the periapsis, but reduces the ΔV as well.
- High drag modulation ratios cause too small ΔV.
- Using drag modulation and lift at the right time can reduce loads, while maintaining acceptable ΔV.

Note that this is a parametric study and its purpose was to evaluate the effect of the different parameters influencing the trajectories. Many assumptions have been made on these choices, that should be investigated further and validated or constrained – relations between $\frac{C_L}{C_D}$ and C_D, position of stagnation point with a non-null angle of attack, additional thermal and structural constraints, relations between $\frac{\beta_2}{\beta_1}$ and $\frac{C_L}{C_D}_2 / \frac{C_L}{C_D}_1$, etc – together with the feasibility of the involved technologies – how such high $\frac{C_L}{C_D}$ can be provided, how it can be changed in the middle of the trajectory, how difficult is to have both technologies – and the related uncertainties.

Moreover, this study has been conducted strictly for 45° sphere-cones with a density of $\sim$ 1450 kg/m^3 and a ratio Ra of 1 and arbitrary constraints; the influence of the density and the ratio will be investigated in the next section, while the angle will not be changed.

4.4 Post-processing and nominal design

As already mentioned, the thermal constraints of the previous section were based on specific choices that were needed just to visualize the influence of the thermal loads on the solutions and will change, modifying the spacecraft density and ratio Ra.

If one wants to use drag modulation, as already mentioned a portion of capsule will be dropped to decrease the reference area, thus increasing the ballistic coefficient. However, if one designs the capsule using the correlations above, will make an error as the skirt will indeed change the Ra, S and the C_D, but it should not be related to the overall volume, and therefore mass, nose radius and so on.

The problem is inverted, the design should be related to the capsule with the higher ballistic coefficient and then the reference area should be increased to decrease the ballistic coefficient on the higher part of the trajectory.

However taking the last results, that used a $\frac{\beta_2}{\beta_1}$ of 3, the optimal ballistic coefficient of 300 kg/m^2 is in reality 900 kg/m^2: with the used Ra and ρ_{SC} this would take a mass of more than 10000 kg: clearly unfeasible. Even pushing to Ra 3 and ρ_{SC} 3000 kg/m^3 the mass would be higher than 740 kg.

The mass drops to 215 kg when the target ballistic coefficient is 600 kg/m^2, thus making more realistic the solutions with $\frac{\beta_2}{\beta_1}$ of 2 or the solution with lower β.

Looking at simulations 22 to 27 one can notice that too small β have too high decelerations at steeper angles, reducing their corridor widths. Lower lift to drag ratios move the optimal corridor width to lower ballistic coefficients, and for instance at simulation 26 a corridor of width 0.72° is achieved at β 250 kg/m^2 (750 kg/m^2 for the design). The corridor drops to 0.64° at simulation 24 for the same β because

no deceleration is done before entering the planet. Looking at simulation 22 – drag modulation ratio of 2 – a corridor of 0.6° is achieved at β 250 kg/m^2 (500 kg/m^2 for the design).

Moreover, it is unlikely to have technologies to perform both lift modulation and drag modulation, therefore the lift to drag coefficient has been fixed along the trajectory.

Selecting ballistic coefficients between 440 and 560 kg/m^2, lift to drag ratios between 0.3 and 0.7 and drag modulation ratios between 1.4 and 2.6 the simulations have been run again in order to find the best combination of these parameters. In order to avoid iterating also around the height of the drag modulation, it has been imposed its activation as soon as a deceleration higher than 8 g is reached.

The first iterations showed how low lift to drag ratio, if kept constant along the trajectories, had overall lower periapses and therefore higher decelerations, thus reducing the corridor widths. The same was happening with high drag modulation ratios as the event was activated before, and therefore less lift was present along the trajectory. Low ratios were excluded as well as the capsule was not decelerating enough before the event. Note that the drag modulation ratio is still $\frac{\beta_2}{\beta_1}$ therefore a higher ratio means a lower β and therefore a higher drag in the first part of the trajectory.

The bigger corridors were between 480 and 540 kg/m^2, but the differences were not discriminant: the iterations have been repeated for β 500 kg/m^2, lift to drag ratios between 0.5 and 0.7 and drag modulation ratios between 1.8 and 2.2, with angles steps of 0.01°. The new results showed an unequivocal increase at $\frac{C_L}{C_D}$ 0.6; the best corridor was achieved for $\frac{\beta_2}{\beta_1}$ 2.1, but the results were similar for other ratios. The achieved corridor was 0.59°.

Now that the optimal ballistic coefficient has been found, the results can be post-processed varying the spacecraft density and the ratio Ra to find a range of masses, TPS mass fractions and peak heat fluxes allowable.

The maximum chosen density was 3000 kg/m^3, while the maximum ratio Ra was set to 5; the mass fraction has been limited to 5% as already mentioned, and the total spacecraft mass was limited to 300 kg.

The steepest trajectory has been taken as it is expected it will have the most extreme thermal conditions and the integrals in Equation 4.9 are computed. The optimal nose radius obtained through Equation 4.10 is 4.7279 m; as it was expected, radiative heat fluxes are milder than convective ones and therefore bigger nose radii are more suitable.

From Figure 4.19a one can notice how the three limits reduce to a narrow region the combination of densities and ratios available. Choosing a Ra of 2 to have Pioneer heritage or 1 to have Hayabusa's one, no solution is found. The maximum density is increased to 4000 kg/m^3 and now solutions with Ra 1 are found: the range of densities available is between 3600 and 4000 kg/m^3, corresponding to masses of 300 and 243 kg, and mass fractions of 3.43% and 3.38%; the nose radius will range between 0.45 and 0.40 m.

In light of what has been said regarding the optimal $\frac{t}{m^{\frac{1}{3}}}$ around Ra 1.4, selecting this Ra the range of densities available is between 2520 and 3800 kg/m^3, corresponding to masses of 300 and 131 kg, and mass fractions of 4.41% and 4.15%. The nose radius would range between 0.35 and 0.23 m, leading to higher heat loads and peak heat fluxes.

The minimum thickness reported by Sepka and Samareh (2015) for PICA is 3.27 cm, while all of the above solutions would result in a thickness greater than 5 cm.

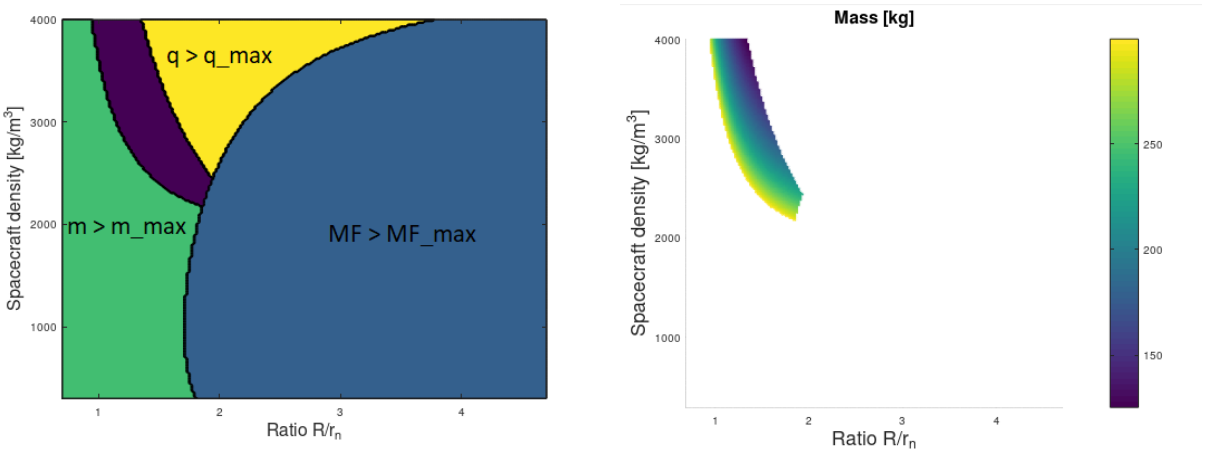

(a) Constraints and range of validity.

(b) Mass variations.

Figure 4.19: Post process of the steepest trajectory with β 500 kg/m^2 varying ρ_{SC} and ratio Ra.

4.4.1 Back cover

The density gives just an idea on how much mass should be fit in the same volume, as to say, to achieve a higher density one should be able to fit the same mass in a smaller volume. This is limited to the densities, shapes, and configuration limitations of the single components and therefore gives an idea of the complexity of the design as the higher it is, the more difficult it will be to fit all the components in a tinier space.

Although the density is something that is usually derived from the design and not one of its drivers, the correlations above showed how for an atmospheric flight the relations between the shape and the mass concur in the definitions of the parameters of interest as the nose radius and the ballistic coefficient and cannot be treated separately.

An expedient used in the design of entry vehicles to reduce the overall density without changing the ballistic coefficient is to design an after-body or back cover: a portion of capsule on the back of the sphere-cone in “shadow” from the upstream flow; with the assumption of a null angle of attack this part of the capsule will not contribute to the aerodynamic coefficients of the body being on the Leeward side (confirmed also through $Freespace$ that uses the 70% vacuum rule) and will not change the reference area, still increasing the volume.

Keeping the same angle of 45° also for the back cover, one can obtain the additional volume as $V_{BF} = \frac{\pi}{3}(R^3 - r_b^3)$ where r_b is the back radius and R is the base radius.

As the total mass will not change, the ratio between the densities will be $\frac{\rho_1}{\rho_2} = \frac{V_2}{V_1} = 1 + \frac{V_{BF}}{V_1}$.

Of course, additional portions of spacecraft will result in additional TPS mass: the back TPS volume can be computed as $V_{BF} - V'$ where V' is computed through the equation above with $R' = R - t_b\sqrt{2}$ and $r'_b = r_b - (\sqrt{2} - 1)t_b$ (Figure 4.20a).

Through the material's density, one can then compute the back TPS mass and therefore the new mass fraction $MF_2 = \frac{mMF_1 + m_{BFtps}}{m} = MF_1 + \frac{m}{m_{BFtps}}$.

It is clear that the thermal loads will be much lower on this side of the body: typically it is assumed that just the 5–10% of the peak heat fluxes will be present on the back cover. Sepka and Samareh (2015) assumes 5% but in order to be conservative, the 10% has been used in this work.

The much lower heat fluxes might justify the use of a lighter TPS, as Acusil 2, SIRCA or SLA-561V, whose maximum allowable heat flux is 1000 kW/m^2 (Sepka and Samareh, 2015). As the maximum peak heat flux allowed was set to 12000 kW/m^2 because of PICA, this would result in 1200 kW/m^2 on the after-body, thus making these materials unsuitable.

Increasing the peak heat flux limitation to 10000 kW/m^2 the yellow region in Figure 4.19a is pushed to the right, limiting the valid region to an even more narrow portion. Now no solution is available for Ra 1.4 thus leaving Ra 1 as the only choice.

Given the ratio Ra, a smaller density will result in a higher mass, lower TPS thickness but higher mass fraction. Regarding the back cover, a higher r_b will result in a smaller decrease in density, but also a smaller increase of the TPS mass fraction.

If one sets a target final density, a smaller initial density will mean that a higher back radius will be enough and the TPS MF will increase less, but starting from a higher initial MF_1,

For the range of initial densities available for Ra 1, a final density of 2000 kg/m^3 has been imposed and the back radius to achieve it for each starting density has been obtained. The three after-body materials have been tried together with PICA and their thickness and mass have been obtained for the aforementioned back radii.

The results showed how SIRCA was the best choice for each case as it was the material increasing less the mass fraction for the given heat loads, followed by PICA, Acusil 2 and lastly SLA-156V, whose results were much higher than the other ones (as it is more suitable for lower heat loads applications). Moreover, it was noticed that lower initial densities were resulting, for the same final density of 2000 kg/m^2, in lower mass fractions.

In light of the fact that lower densities were more suitable and that PICA was still the second-best choice, the results for Ra 1.4 were tried in the same way but only with PICA, however the minimum mass fraction was still more than 1% higher than the SIRCA one both because of higher thermal loads and higher starting mass fraction, thus justifying the previously imposed limit and the choice of Ra 1.

Lastly, a spherical back cover has been tried as well with the same methodology, where the volume of the spherical cap is computed through $V_{BF} = \frac{\pi}{6} h(3R^2 + h_c^2)$ where h_c is the height of the spherical cap, iterated between 0 and R. To compute the TPS volume, the same equation can be applied using $h_c' = h_c - t_b$ and $R' = R - \sqrt{t_b^2 - h^2 - 2R_c(t_b - h)}$ with $R_c = \frac{R^2 + h_c^2}{2h_c}$ (Figure 4.20b).

It revealed how spherical back covers allows obtaining greater ratios $\frac{\rho_2}{\rho_1}$ but with higher TPS mass fractions; moreover also lower ratios not available for the conical back covers are now possible.

The conical back cover has been kept because of the lower final mass fraction for the desired density ratio.

To conclude, with Ra 1 the lowest allowable density is 3611.5 kg/m^3, corresponding to a mass of

298.38 kg, and a mass fraction of 3.4258%. The nose radius will be 0.4478 m and so will be the base radius. To achieve a final density of 2000 kg/m^3 a back radius of 0.2972, for a ratio $\frac{R}{r_b}$ of $\sim$ 1.5, the final mass fraction is 5.3286%. The front-body TPS thickness is 5.3387 cm, while the after-body one is 3.1535 cm.

The minimum mass fraction possible is 5.03%, but giving a final density of 2946 kg/m^3.

Note that the density has been assumed as referred to the whole capsule, and not only to the mass without TPS over the inner volume, however this was assumed also in the derivation of the densities in Table 4.7: the knowledge of their TPS mass and volume, and the total volume including the back covers, would give more useful values.

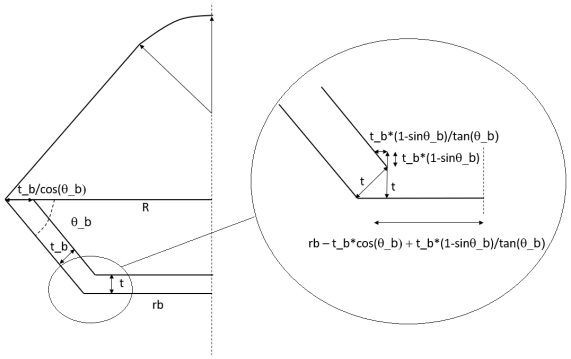

(a) Conical Back-face TPS construction.

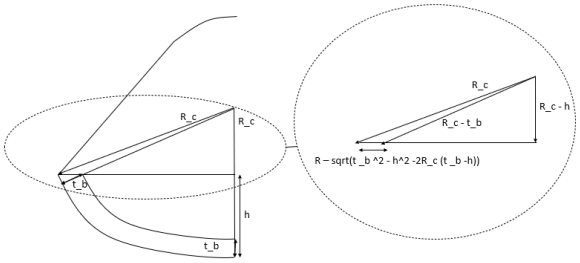

(b) Spherical Back-face TPS construction.

Figure 4.20: Back-faces.

4.4.2 Drag skirt

The selected concept includes a drag modulation ratio $\frac{\beta_2}{\beta_1}$ of 2.1. To achieve that a drag skirt can be included at the end of the sphere-cone to increase the surface and therefore decrease the ballistic coefficient however, its addition will of course increase the total mass, thus increasing β (Figure 4.11b)

The ratio $\frac{\beta_1}{\beta_2}$ can be written as:

$$\frac{\beta_1}{\beta_2} = \frac{m_2 + m_S}{m_2}\frac{S_2 C_{D2}}{S_1 C_{D1}} = (1 + \frac{m_S}{m_2})(\frac{R}{R_s})^2 \frac{C_{D2}}{C_{D1}} \tag{4.13}$$

where the subscript 1 is referred to the capsule with the skirt, and 2 without it.

As the drag modulation event is set to be activated when the deceleration hits 8 g, it will happen late on the trajectory and therefore this portion will be subjected to high thermal loads as well. For the steepest trajectory considered along this section, the event occurs at an altitude of $\sim$ 94 km, and the heat load at that point of the trajectory is $\sim \frac{1}{3}$ of the total one, with heat fluxes up to 6600 kW/m^2: the use of PICA for this part seems unavoidable.

The equation above $V_{BF} = \frac{\pi}{3}(R^3 - r_b^3)$ can be used in this frame as well since the angle is fixed to 45°. Defining the thickness t_s as the total thickness of this component, computed through the correlations used above for the heat loads accumulated up to the drop of the skirt, the values of R and r_b in the equation will be substituted respectively by $R_s - t\sqrt{2}$ and $R - t\sqrt{2}$ (Figure 4.20b).

Moreover, the use of this component just on the upper part of the atmosphere means that it will be for most of its time in the free-molecular regime, whose onset will be just around 100 km, therefore the C_{D1} in the equation above will be computed through Equation 4.5b.

This helps a lot as the ratio between free molecular and continuum C_D is already $\sim$ 1.6 for a given ratio, and will therefore reduce the dimensions of the skirt.

The obtained thickness is 4.36 cm while the radius of the skirt will be 0.5052 m, as to say 1.13 times the base radius; the overall weight of the skirt will be less than 1 kg.

Note that the back cover of the previous section has been dimensioned using as initial radius the base radius, however considering the presence of the skirt it should be recomputed using $R - t_s\sqrt{2}$.

Lastly, note that the maximum deceleration this portion will be subjected to will be up to 8 g, and therefore very high structural loads will be applied to it; the absence of a cover on the bottom will subject it to bending, although it will be limited by the shortness of the skirt ($\sim$ 6 cm).

The final shape will have therefore a diameter of $\sim$ 1 m, much lower than the Ariane 6 short fairing's total diameter of 4.6 m.

4.5 Nominal trajectory

These dimensions have been normalized to $r_n = R$ 0.45 m, R_s 0.52 m, r_b 0.3 m, with m_1 301 kg and m_2 300 kg.

The C_D is now computed at each step through the Newton theory to take into account its changes with Kn. According to Li et al. (2021) the C_L does not vary much with Kn: since it was defined with respect to the continuum C_D the ratio $\frac{C_L}{C_D}$ is now updated to $0.6\frac{C_{D_{co}}}{C_D(H)}$ to keep the C_L constant.

The accuracy was now set to 1e-8 and the complete software was run.

The corridor's extremes obtained before are of course not valid any more and have been obtained again through trials and errors: it is now comprised between -0.44° and -1.06°, for a width of 0.62°.

The obtained values of peak heat fluxes and heat loads are now different as well, however prior to iterating again the capsule's components, it is good practice to introduce an uncertainty on the atmospheric density, usually of the 20% to account for inaccuracies on the atmospheric model.

With a scale factor of 0.8, the lowest angle has been tried giving now a ΔV too small to capture the spacecraft; it has been iteratively increased until -0.47° that gave a ΔV of 0.82 km/s.

With a scale factor of 1.2 the steepest angle has been tried as well, and reduced to -1.05° to have a deceleration lower than 10 g. When this angle has been tried with scale factor 0.8 however a problem arose, the skirt was now dropped later, resulting in a decrease of the periapsis and therefore an increase of the thermal loads, with a peak heat flux now higher than 10000 kW/m^2.

The method of the previous section was applied to these new results, however not giving any result for the selected limits, the angle was therefore reduced, and the method applied again until the angle -0.97° gave a peak heat flux lower than 10000 kW/m^2; all the angles between the two gave no results with Ra 1.

As the decrease in the corridor width would be of 0.08°, in order to choose between the two options the TPS of each component has been dimensioned again for both cases.

Moreover, as in the second case the skirt is dropped almost at the periapsis, it was noticed that the accumulated heat loads are much higher than the previous result: this could happen for entry angles lower than the steepest one as well, and therefore it was decided to dimension the skirt TPS using the periapsis heat load of the steepest case in order to be conservative: respectively 226.29 MJ/m^2 for -1.05° and 213.42 MJ/m^2 for -0.97°.

The skirt was dimensioned first now, giving a $t_s\sqrt{2}$ of 0.0705 m for the trajectory of -1.05° and 0.06974 m for -0.97°, thus resulting in similar external diameter and total mass.

The back cover has been now dimensioned taking into account the presence of the skirt: the final density of 2000 kg/m^3 was now impossible to achieve with the conical back cover.

For the steeper trajectory only PICA was available: through a conical back cover the maximum final density was 2146 kg/m^3 with a total TPS mass fraction of 5.35%, while the spherical cap would allow the final density of 2000 kg/m^3 but with a mass fraction of 9.02%.

For the other case all the materials were available for the back cover; SIRCA was again the best choice, but the results were similar, 2140 kg/m^3 was the maximum final density of the conical back cover with a mass fraction of 5.17%, while the spherical mass fraction would be 8.69%.

In this frame the final density of $\sim$ 2150 kg/m^3 can be accepted as more refined design will probably improve these values, therefore the conical back cover has been kept. Regarding the angles, an increase of mass fraction of just 0.18% is totally acceptable in order to have a bigger corridor, thus justifying the choice of PICA for the back cover as well, moreover more detailed analyses of the fluxes will probably reveal lower stagnation loads and even lower back cover loads, allowing for the use of SIRCA anyway.

To obtain this final density, however, a back radius of 0 m should be used. It is clear that this does not make sense as there will be a value over which the additional volume will be more TPS than available volume, thus reinforcing the idea of referring the density to the inner mass and volume. This might as well lead to the selection of denser TPS but with a lower thickness.

Looking at the ratio of $\frac{\rho_1}{\rho_2}$ over MF_2 one can find a maximum, where additional portions of back cover will increase too much the TPS mass without increasing enough the volume.

The final obtained dimensions are $r_n = R =$ 0.45 m, the TPS thickness is 5.5122 cm, resulting in a MF of 3.5159% over a $m_2 =$ of 300 kg. The skirt radius is $R_s =$ 0.52 m, with a TPS t_S of 4.9602 cm, resulting in a mass $m_1 =\sim$ 301 kg. Lastly, the back radius r_b is 0.063119 m, the thickness t_b will be 3.5833 cm, leading to a total mass fraction of 5.3332% and a final density of 2148 kg/m^3. The total height of the probe will be 0.6503 m. A $\frac{C_L}{C_{Dco}}$ of 0.6 has been assumed.

Note that the angles are rotation around the entry angle: with an uncertainty of 20% on the atmospheric density, a corridor of 0.58° comprised between -9.585° and -10.165° has been found. The central value of -0.76° has been taken as target to guarantee a margin of $\pm$ 0.29° and the results in Table 4.8 have been obtained. In order to achieve this angle without changing the entry velocity a burn of $\sim$ 150 m/s should be needed, however the interplanetary trajectory can be computed again aiming for a lower periapsis in order to have a steeper entry angle, the whole calculations should be iterated again

with the new velocity.

Table 4.8: Trajectory characteristics.

Rotation angle [°](ρ SF)	-0.76 (1)	-0.76 (0.8)	-0.76 (1.2)	-0.47 (0.8)	-1.05 (1.2)	-1.05 (0.8)
Periapsis [km]	93.6379	93.0508	94.1238	96.6837	91.7532	90.5174
ΔV [km/s]	1.6594	1.5971	1.7113	0.8176	2.3230	2.2334
Peak $\dot{q}$ [kW/m^2]	7319.5908	8185.0111	6725.2651	5285.4638	8606.0750	10715.3267
Total heat load [MJ/m^2]	285.5926	320.8346	258.2850	262.1825	298.8622	377.2887
Peak deceleration [g]	6.7711	6.4293	7.0223	2.5382	9.9019	9.2480
Trajectory time [s]	222	246	230	373	378	386
R_a [km]	28984.7260	31306.7610	27267.0530	291826.5133	15330.0868	16656.8091
V_a [km/s]	1.9782	1.8436	2.0913	0.2092	3.4763	3.2368
ΔV_{ap} [m/s]	22.6081	21.1991	23.6842	7.7354	37.4834	35.2942

Below are reported some figures showing the trend of the most important quantities along the atmospheric flight for the case with entry angle of -9.875° (Rotation of –0.76°) and unitary density scale factor. As in Figure 4.21a it is clear how the drag skirt is not dropped as the peak deceleration is lower than 7g. The total heat load is $\sim$ 286 MJ/m^2 while the skirt was dimensioned for 226.29 MJ/m^2, a value that would be reached shortly after the periapsis (Figure 4.21b): a more detailed analysis of what would happen is needed in those cases as the heat loads will keep increasing up to the exit of the atmosphere. It can be assumed in a first approximation that for steeper angles, even if it ablates completely it would not cause any ΔV problem because of the high decelerations and therefore already high ΔV, while for more gentle angles the heat loads will be much lower, and therefore it will not ablate completely.

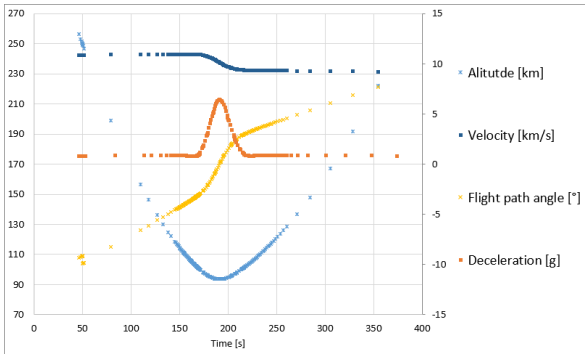

(a) Atmospheric flight overview.

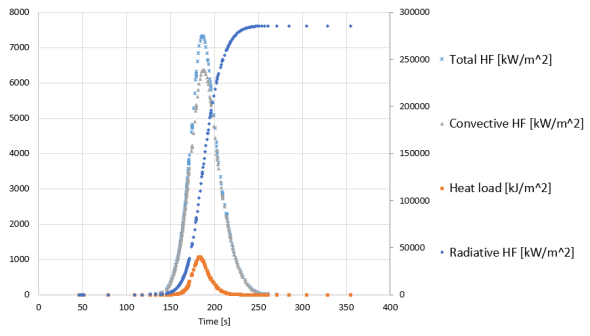

(b) Thermal loads.

Figure 4.21: Aerocapture manoeuvre for entry angle -9.875° and unitary density scale factor.

In order to achieve an orbit around the planet, a burn must be done at the apoapsis to increase the periapsis up to a level outside the atmosphere to avoid a second atmospheric passage that might lead to an entry trajectory because of the low entry speed.

With the apoapsis distance R_a and the velocity V_a, the following relations can be applied (Curtis,

2008):

$$R_a = (1+e)a \tag{4.14a}$$

$$V_a = \sqrt{\frac{(1-e)\mu}{(1+e)a}} = \sqrt{\frac{(1-e)\mu}{R_a}} \tag{4.14b}$$

$$R_p = (1-e)a \tag{4.14c}$$

where e is the eccentricity of the orbit, a is the semi-major axis and R_p is the periapsis distance.

Therefore, setting R_p at the limit of the atmosphere (250 + 6051.8 km As in Table 3.2) one can find the ΔV needed to raise the periapsis outside the atmosphere:

$$\Delta V_{ap} = V_a - \sqrt{\frac{2\mu R_p}{R_a^2 + R_a R_p}} \tag{4.15}$$

For the central case with unitary ratio, the eccentricity is 0.6508, the semi-major axis is 17557.4831 km resulting in a period of $T = 2\pi\sqrt{\frac{a^3}{\mu}}$ 25646.3799 s, as to say slightly more than 7 hours.

Line of Sight with the Earth is granted for 22113 s, $\sim$ 86% of the total period, slightly more than 6 hours, while LoS with the Sun is 24360 s: $\sim$ 95% of the time, resulting in eclipses of $\sim$ 20 minutes.

4.6 Concurrent design

One should however keep in mind that the presented design is just an example thought to investigate the main parameters playing a role in the mission analysis and guide the preliminary phases of a more complete design.

Indeed, although a generic design has been obtained, a set of arbitrary constraints had been selected, whose influence might be investigated studying additional options within the CDF model as for instance the allowance of higher structural loads might give considerable benefits to the corridor, maintaining still an acceptable structural mass and volume.

Moreover, here is presented just an iteration of the whole process, that in a CDF environment will be followed by specific analyses of the heat fluxes, TPS behaviour and design, thermal control system, overall configuration and so on, leading to new requirements for instance in terms of volume or mass. Moreover, the found mass of 300 kg might be too big for the mission to be accepted and as decreasing mass is one of the main driver of a mission design, a complete and further optimized design might have a much lower mass and therefore the whole approach should be iterated as well, aiming for instance to lower ballistic coefficients or allowing higher loads or TPS mass fractions.

In the concurrent design process, the whole methodology presented above should therefore be iterated with the new set of parameters provided by the other specialists to converge in a multidisciplinary coherent design, and more options should be examined.

Nevertheless, a lot of useful knowledge has been achieved along the study, to be used as starting point of new concepts: lift has been found to be crucial to achieve a wide corridor, however, the initial

design concerned just an axisymmetric probe, that can provide only limited lift through offset of the centre of gravity. Further studies or CDF options should consider providing lift from the first phases of the design, driving the shape optimization and accounting for the related requirements and constraints.

This mission has been studied at the Institute for Plasmas and Nuclear Fusion Concurrent Design Facility “Laica”. The facility has been developed in parallel with this thesis, using this mission as an example study mission.

Its development involved the procurement of existing tools (as GMAT) or the creation of tools as the ATP code to be used by the specialists. Along the creation of the whole software architecture needed for the process, the study in depth of the mission has been performed, providing a complete multidisciplinary design of the spacecraft described in Lino da Silva et al. (2022). The problematic involved in the creation of the facility and the software used are reported as well in Lino da Silva et al. (2022), which gives an overview of the whole process and of the mission concept and subsystems.

Many aspects have been accounted for in the complete design, as the relation between the Attitude and Orbit Control System (AOCS) and the interplanetary trajectory inaccuracies, deriving uncertainties on the entry conditions, proper thermal and structural designs, as well as the relations between the sampling conditions and time required for the sampling process and the corresponding data budget, resulting in the selection of a telecommunication system able to send all data back to Earth considering the achieved orbit and the attitude pointing. AOCS and manoeuvres ΔV have been used to derive a ΔV budget and therefore to dimension the propulsion system and the fuel mass. Detailed mass and power budgets have been obtained, as well as a nominal configuration of the spacecraft and its bus.

Chapter 5

Conclusions

In the frame of developing a phase 0 conceptual study for a Venus atmospheric sample analysis, a literature survey of the current knowledge and unknowns about the planet was necessary to identify the possible sampling targets and their location.

As this study was conducted in a Concurrent Design Facility, the concepts and ideas of the concurrent design have been applied to make a first round of trade-offs between different possibilities to collect and analyse the samples, setting already some constraints and assumptions on which the whole design would have been based on as the aerocapture concept or the minimum altitude for sample collection.

The first step of the mission definition has been the derivation of the interplanetary trajectory. Analytical methods have been applied to have a theoretical starting point and their outputs have been implemented on GMAT where an iterative process led to a precise trajectory including gravity models, external gravity perturbations and precise celestial bodies' positions.

The method however assumed an initial parking orbit with arbitrary radius and inclination, just taking into account the launcher's escape velocity limitation. Moreover, it did not include perturbations as the launcher de-pointing, solar radiation pressure, AOCS inaccuracies, etc. The obtained outputs were still precise enough to be used as starting point for the atmospheric flight propagation.

The code developed in the scope of this thesis for atmospheric flight propagation, and specifically aerocapture manoeuvres was validated successfully against GMAT giving acceptable relative errors in the order of 1e-5, proven to be numerical inaccuracies deriving from the use of an atmospheric model. Errors of this order of magnitude were present also within GMAT, when used with different accuracies, confirming the hypothesis of numerical errors related to double precision floating point.

The implementation of the developed software in the new CDF facility at Instituto Superior Técnico (IST) allowed to perform a conceptual design, providing the mission analysis, requirements, configuration, main budgets and initial payload of a Venus Atmospheric Sample Analysis Probe.

Although validated, the code is not yet a solid and powerful tool as its capabilities are limited: the main limitation is definitely the computational speed, limiting its application in parametric studies or Monte Carlo simulations.

Monte-Carlo analyses have been performed, and the correct implementation of the method has been

verified, however due to the slow computational speed of the code and the machine running it, just a limited amount of trajectories could be simulated, and with accuracies resulting on errors of the order of 10^1, thus the choice of not reporting the results here.

Moreover, the database should be upgraded to include other celestial bodies, more precise gravitational models, different shapes and correlations, etc. The ephemerides should be also available for the bodies of interest and for a wide range of dates, instead of needing an external software to download them. This would lead to the possibility to include gravitational perturbations of more external bodies as well as their eventual shadow.

The Monte Carlo method developed for uncertainties propagation could be extended to a design version, in order to simulate all the parameters influencing the trajectory and find different optimal values for given constraints.

Moreover, using correlations for the recession of the TPS, the effect of the mass loss on the shape and on the total mass could be investigated updating the ballistic coefficient with the TPS ablation.

Lastly, the code could be evolved to a six Degrees of Freedom version in order to take into account moments and stability of the probe, as well as making it possible to see the effect of the angle of attack and the relations between lift and drag.

However, the code has been thought as a design tool for the use in a CDF and therefore its simplicity has been useful to consider more aspects of the design concurring in the mission analysis. Indeed, a system-focused methodology has been applied for the design, taking into account several quantities at the same time as the relations between total mass and density on the ballistic coefficient as well as on the shape, and therefore on thermal loads and so on.

For the given arbitrary design choices in terms of limitations, a good corridor width has been found including margins on the atmospheric density, resulting in a low TPS mass fraction and with acceptable structural loads for a given limit mass of 300 kg, and total density of 2150 kg/m^3.

It has been found that lift is required for having an acceptable entry corridor width however, the main limitation of this study is exactly that lift has been introduced without analysing the impact of this choice on the other parts of the design. This is of course a very coarse assumption, and should be studied as a further option of the CDF study, in terms of requirements, shape, location of the centre of gravity, configuration, TPS, etc.

Lastly, more detailed analyses should be carried out on the thermal loads: the used correlations are built to be conservative and therefore useful during early design phases, however Computational Fluid Dynamics simulations will be needed to assess more realistic stagnation heat fluxes and their distribution along the shape leading to an adjustable TPS thickness. More detailed analyses of the TPS thickness will be needed for the specific trajectory and taking into account the external conditions of Venus. Analyses of this type could help outline as well the range of validity of the used correlations and the development of similar correlations for other planets beside the Earth.

References

F. Albarede, M. Gargaud, R. Amils, J. C. Quintanilla, H. J. Cleaves, W. M. Irvine, D. L. Pinti, and M. Viso. *Hydrodynamic Escape*. Springer Berlin Heidelberg, Berlin, Heidelberg, 2011.

J. D. Anderson. *Hypersonic and High Temperature Gas Dynamics, Second Ed.* American Institute of Aeronautics and Astronautics, 2006.

K. H. Baines, S. K. Atreya, M. A. Bullock, D. H. Grinspoon, P. Mahaffy, C. T. Russell, G. Schubert, and K. Zahnle. *The Atmospheres of the Terrestrial Planets: Clues to the Origins and Early Evolution of Venus, Earth, and Mars*. University of Arizona Press, 2013. ISBN 978-0-8165-3059-5. doi: 10.2458/azu_uapress_9780816530595-ch006. URL http://muse.jhu.edu/books/9780816599752/9780816599752-13.pdf.

W. Bains, J. J. Petkowski, P. B. Rimmer, and S. Seager. Production of ammonia makes venusian clouds habitable and explains observed cloud-level chemical anomalies. *Proceedings of the National Academy of Sciences*, 118(52), Dec 2021a. ISSN 0027-8424, 1091-6490. doi: 10.1073/pnas.2110889118.

W. Bains, J. J. Petkowski, S. Seager, S. Ranjan, C. Sousa-Silva, P. B. Rimmer, Z. Zhan, J. S. Greaves, and A. M. S. Richards. Phosphine on Venus Cannot be Explained by Conventional Processes. *Astrobiology*, 21(10), Oct. 2021b. ISSN 1531-1074, 1557-8070. doi: 10.1089/ast.2020.2352. URL http://arxiv.org/abs/2009.06499.

M. Bandecchi, B. Melton, and F. Ongaro. Concurrent engineering applied to space mission assessment and design. *concurrent engineering*.

J. O. Cappellari, C. E. Velez, and A. J. Fuchs. *Mathematical theory of the Goddard trajectory determination system*, volume 71106. Goddard Space Flight Center, 1976.

E. Chassefière, R. Wieler, B. Marty, and F. Leblanc. The evolution of venus: Present state of knowledge and future exploration. *Planetary and Space Science*, 63–64, Apr 2012. ISSN 00320633. doi: 10.1016/j.pss.2011.04.007.

COMET. User guide: http://cdp4docs.rheagroup.com/, 2018.

G. E. Cook. Luni-solar perturbations of the orbit of an earth satellite. *Geophysical Journal of the Royal Astronomical Society*, 6(3), Apr 1962. ISSN 00168009. doi: 10.1111/j.1365-246X.1962.tb00351.x.

H. D. Curtis. *Orbital mechanics for engineering students*. Elsevier Aerospace engineering series. Elsevier Butterworth Heinemann, 1. ed., reprinted edition, 2008. ISBN 978-0-7506-6169-0.

D. S. D. Final report system design of the pioneer venus spacecraft. 1, Jul 1973.

L. R. Dartnell, T. A. Nordheim, M. R. Patel, J. P. Mason, A. J. Coates, and G. H. Jones. Constraints on a potential aerial biosphere on venus: I. cosmic rays. *Icarus*, 257, 2015. ISSN 0019-1035. doi: https://doi.org/10.1016/j.icarus.2015.05.006. URL https://www.sciencedirect.com/science/article/pii/S0019103515002080.

J. R. Dormand and P. J. Prince. A family of embedded runge-kutta formulae. *Journal of Computational and Applied Mathematics*, 6(1), 1980. ISSN 0377-0427. doi: https://doi.org/10.1016/0771-050X(80)90013-3. URL https://www.sciencedirect.com/science/article/pii/0771050X80900133.

A. J. Erb, T. K. West, and C. O. Johnston. Investigation of galileo probe entry heating with coupled radiation and ablation. *Journal of Spacecraft and Rockets*, 57(4), Jul 2020. ISSN 0022-4650, 1533-6794. doi: 10.2514/1.A34751.

B. Fegley. Atmospheric evolution on venus. 2004.

B. Fritsche, G. Koppenwallner, and M. e. a. Ivanov. Advanced model for spacecract disintegration during atmospheric re-entry, executive summary. 2000.

E. M. Gaposchkin. Atmospheric superrotation? *Planetary and Space Science*, 51(6), May 2003. ISSN 00320633. doi: 10.1016/S0032-0633(03)00021-7.

D. GEGOUT. Interface to easily download jpl ephemerides. https://www.mathworks.com/matlabcentral/fileexchange/52428-interface-to-easily-download-jpl-ephemerides, 2022.

R. C. Ghail, M. S. Gilmore, S. E. Smrekar, A. H. Treiman, and C. F. Wilson. The exploration of venus: current understanding and open questions. (2132), 2019.

C. Gillmann, G. J. Golabek, and P. J. Tackley. Effect of a single large impact on the coupled atmosphere-interior evolution of venus. *Icarus*, 268, Apr 2016. ISSN 00191035. doi: 10.1016/j.icarus.2015.12.024.

GMAT. User guide: http://gmat.sourceforge.net/docs/r2018a/help-letter.pdf, 2020.

Y. Gong, Y. Guo, G. Ma, and M. Guo. Mars entry guidance for mid-lift-to-drag ratio vehicle with control constraints. *Aerospace Science and Technology*, 107, 2020. ISSN 1270-9638. doi: https://doi.org/10.1016/j.ast.2020.106361. URL https://www.sciencedirect.com/science/article/pii/S1270963820310439.

J. S. Greaves, A. Richards, W. Bains, P. B. Rimmer, D. L. Clements, S. Seager, J. J. Petkowski, C. Sousa-Silva, S. Ranjan, and H. J. Fraser. Re-analysis of phosphine in venus' clouds. *arXiv preprint arXiv:2011.08176*, 2020a.

J. S. Greaves, A. M. S. Richards, W. Bains, P. B. Rimmer, H. Sagawa, D. L. Clements, S. Seager, J. J. Petkowski, C. Sousa-Silva, S. Ranjan, E. Drabek-Maunder, H. J. Fraser, A. Cartwright, I. Mueller-Wodarg, Z. Zhan, P. Friberg, I. Coulson, E. Lee, and J. Hoge. Phosphine gas in the cloud decks of venus. *Nature Astronomy*, 5(7), Sep 2020b. ISSN 2397-3366. doi: 10.1038/s41550-020-1174-4.

S. Gruchola, A. Galli, A. Vorburger, and P. Wurz. The upper atmosphere of venus: Model predictions for mass spectrometry measurements. *Planetary and Space Science*, 170, Jun 2019. ISSN 00320633. doi: 10.1016/j.pss.2019.03.006.

A. E. Hedin. Extension of the msis thermosphere model into the middle and lower atmosphere. *Journal of Geophysical Research: Space Physics*, 96(A2), Feb 1991. ISSN 01480227. doi: 10.1029/90JA02125.

Horizon. Ephemeris system: https://ssd.jpl.nasa.gov/horizons/app.html, 2022.

T. Imamura, J. Mitchell, S. Lebonnois, Y. Kaspi, A. P. Showman, and O. Korablev. Superrotation in planetary atmospheres. *Space Science Reviews*, 216(5), Aug 2020. ISSN 0038-6308, 1572-9672. doi: 10.1007/s11214-020-00703-9.

A. Izidoro and S. N. Raymond. Formation of terrestrial planets. *arXiv:1803.08830 [astro-ph]*, 2018. doi: 10.1007/978-3-319-55333-7_142.

S. A. Jacobson, D. C. Rubie, J. Hernlund, A. Morbidelli, and M. Nakajima. Formation, stratification, and mixing of the cores of earth and venus. *Earth and Planetary Science Letters*, 474, Sep 2017. ISSN 0012821X. doi: 10.1016/j.epsl.2017.06.023.

G. James, D. Burley, D. Clements, P. Dyke, and J. Searl. *Modern engineering mathematics*. Pearson Education, 2008.

H. L. Justh, A. M. D. Cianciolo, and J. Hoffman. Venus global reference atmospheric model (venus-gram): User guide. 2021.

N. H. Kemp and F. R. Riddell. “heat transfer to satellite vehicles re-entering the atmosphere. *Journal of Jet Propulsion*, 1957.

D. J. Kinney, J. V. Bowles, . H. L Yang, and C. D. Roberts. Conceptual design of a ’sharp’-ctv. 2001.

R. Laiger. Ariane 6 user’s manual, issue 2 revision 0, 2021.

H. Lammer, A. L. Zerkle, S. Gebauer, N. Tosi, L. Noack, M. Scherf, E. Pilat-Lohinger, M. Güdel, J. L. Grenfell, M. Godolt, and A. Nikolaou. Origin and evolution of the atmospheres of early venus, earth and mars. *The Astronomy and Astrophysics Review*, 26(1), Nov 2018. ISSN 0935-4956, 1432-0754. doi: 10.1007/s00159-018-0108-y.

G. A. Landis. Colonization of Venus. In *AIP Conference Proceedings*, volume 654, Albuquerque, New Mexico (USA), 2003. AIP. doi: 10.1063/1.1541418. URL `http://aip.scitation.org/doi/abs/10.1063/1.1541418`.

W. R. J. Larson J. W. *Space mission analysis and design*. Space technology library. Microcosm; Kluwer, El Segundo, Calif.: Dordrecht; Boston, 3rd ed edition, 1999. ISBN 978-0-7923-5901-2.

Y. J. Lee, A. García Muñoz, A. Yamazaki, M. Yamada, S. Watanabe, and T. Encrenaz. Investigation of uv absorbers on venus using the 283 and 365 nm phase curves obtained from akatsuki. *Geophysical Research Letters*, 48(7), Apr 2021. ISSN 0094-8276, 1944-8007. doi: 10.1029/2020GL090577. URL https://onlinelibrary.wiley.com/doi/10.1029/2020GL090577.

L. Lees. Laminar heat transfer over blunt nosed bodies at hypersonic speeds. *Journal of Jet Propulsion*, 1956.

H. Legge. Hypersonic approximations for heat transfer and shear stress applied to continuum and rarefied plume impingement. 1987.

J. Li, D. Jiang, and J. Geng, X.and Chen. Kinetic comparative study on aerodynamic characteristics of hypersonic reentry vehicle from near-continuous flow to free molecular flow. 2021.

M. Lino da Silva, L. Marraffa, G. Musso, H. Neiva da Silva, M. Azevedo Ferreira, Y. Jeyagobi, M. Pavanello, L. Lemos Alves, and B. M. Soares Gonçalves. A new concurrent design facility at tecnico lisbon. In *10th International systems concurrent engineering for space applications conference (SECESA 2022)*, Oct 2022.

M. A. P. Lino da Silva. Freespace manual. can be found at http://esther.ist.utl.pt/freespace/manual.pdf, 2020.

Y. Marcq, C. D. Yung, and K. L. Parkinson. Atmospheric chemistry on venus: an overiview of unresolved issues. *50th Lunar and Planetary Science Conference 2019 (LPI Contrib. No. 2132)*, 313, 2019. ISSN 00191035. URL https://www.hou.usra.edu/meetings/lpsc2019/pdf/2374.pdf.

M. Y. Marov and S. I. Ipatov. Delivery of water and volatiles to the terrestrial planets and the moon. *Solar System Research*, 52(5), Sep 2018. ISSN 0038-0946, 1608-3423. doi: 10.1134/S0038094618050052.

G. Micela. Evolution of Stellar Coronal Activity on the Main Sequence. In B. Montesinos, A. Gimenez, and E. F. Guinan, editors, *The Evolving Sun and its Influence on Planetary Environments*, volume 269 of *Astronomical Society of the Pacific Conference Series*, Jan. 2002.

A. Morbidelli and B. Wood. Late accretion and the late veneer. *arXiv:1411.4563 [astro-ph]*, Sep 2015. doi: 10.1002/9781118860359.ch4.

D. Nikolić, S. M. Madzunkov, and M. R. Darrach. Response of qit-ms to noble gas isotopic ratios in a simulated venus flyby. *Atmosphere*, 10(5), Apr 2019. ISSN 2073-4433. doi: 10.3390/atmos10050232.

J. E. Owen, I. F. Shaikhislamov, H. Lammer, L. Fossati, and M. L. Khodachenko. Hydrogen dominated atmospheres on terrestrial mass planets: Evidence, origin and evolution. *Space Science Reviews*, 216(8), Dec 2020. ISSN 0038-6308, 1572-9672. doi: 10.1007/s11214-020-00756-w.

M. R. Patel, J. P. Mason, T. A. Nordheim, and L. R. Dartnell. Constraints on a potential aerial biosphere on venus: Ii. ultraviolet radiation. *Icarus*, 373, 2022. ISSN 0019-1035. doi: https://doi.org/10.1016/j.icarus.2021.114796. URL https://www.sciencedirect.com/science/article/pii/S0019103521004449.

J. Rabinovitch, A. Borner, and M. A. Gallis. The cupid's arrow mission concept: hypervelocity sampling in the upper atmosphere of venus. In *16th International Planetary Probe Workshop*, volume 2019, 2019a.

J. Rabinovitch, A. Borner, M. A. Gallis, and C. Sotin. Hypervelocity noble gas sampling in the upper atmosphere of venus. In *AIAA Aviation 2019 Forum*. American Institute of Aeronautics and Astronautics, Jun 2019b. ISBN 978-1-62410-589-0. doi: 10.2514/6.2019-3223. URL https://arc.aiaa.org/doi/10.2514/6.2019-3223.

M. Redmond and A. J. Mastropietro. Thermophysical and optical properties of materials considered for use on the ldsd test vehicle. 2015.

P. B. Rimmer, S. Jordan, T. Constantinou, P. Woitke, O. Shorttle, R. Hobbs, and A. Paschodimas. Hydroxide salts in the clouds of venus: Their effect on the sulfur cycle and cloud droplet ph. *The Planetary Science Journal*, 2(4), Aug 2021. ISSN 2632-3338. doi: 10.3847/PSJ/ac0156.

J. A. Samareh. A multidisciplinary tool for systems analysis of planetary entry, descent, and landing (sape). 2009.

B. J. Sandor and R. Todd Clancy. First measurements of clo in the venus atmosphere – altitude dependence and temporal variation. *Icarus*, 313, Oct 2018. ISSN 00191035. doi: 10.1016/j.icarus.2018.04.022.

S. A. Schaaf and P. L. Chambre. Flow of rarefied gases. *Princeton Aeronautical Paperbacks 8*, 1958.

S. Sepka and J. A. Samareh. Thermal protection system mass estimating relationships for blunt-body, earth entry spacecraft. In *45th AIAA Thermophysics Conference*, Dallas, TX, Jun 2015. American Institute of Aeronautics and Astronautics. ISBN 978-1-62410-361-2. doi: 10.2514/6.2015-2507. URL https://arc.aiaa.org/doi/10.2514/6.2015-2507.

K. Sutton and R. A. Graves. A general stagnation-point convective-heating equation for arbitrary gas mixtures. 1971.

A. Sánchez-Lavega, S. Lebonnois, T. Imamura, P. Read, and D. Luz. The atmospheric dynamics of venus. *Space Science Reviews*, 212(3–4), Nov 2017. ISSN 0038-6308, 1572-9672. doi: 10.1007/s11214-017-0389-x.

Y. Takahashi and K. Yamada. Aerodynamic-heating analysis of sample-return capsule in future trojan-asteroid exploration. *Journal of Thermophysics and Heat Transfer*, 32(3), Jul 2018. ISSN 0887-8722, 1533-6808. doi: 10.2514/1.T4837.

M. E. Tauber, G. E. Palmer, and D. Prabhu. Stagnation point radiative heating relations for venus entry. 2012.

D. Titov, N. Ignatiev, K. McGouldrick, V. Wilquet, and C. Wilson. 11 2018.

R. Van Der Hilst. Essentials of geophysics. https://ocw.mit.edu/courses/12-201-essentials-of-geophysics-fall-2004/resources/ch2/, 2004.

A. C. Vandaele, O. Korablev, D. Belyaev, S. Chamberlain, D. Evdokimova, T. Encrenaz, and L. Esposito. Sulfur dioxide in the venus atmosphere: I. vertical distribution and variability. *Icarus*, 295, Oct 2017. ISSN 00191035. doi: 10.1016/j.icarus.2017.05.003.

G. Villanueva, M. Cordiner, P. Irwin, I. de Pater, B. Butler, M. Gurwell, S. Milam, C. Nixon, S. Luszcz-Cook, C. Wilson, V. Kofman, G. Liuzzi, S. Faggi, T. Fauchez, M. Lippi, R. Cosentino, A. Thelen, A. Moullet, P. Hartogh, E. Molter, S. Charnley, G. Arney, A. Mandell, N. Biver, A. Vandaele, K. de Kleer, and R. Kopparapu. No evidence of phosphine in the atmosphere of venus by independent analyses. *Nature Astronomy*, 5(7), Jul 2021. ISSN 2397-3366. doi: 10.1038/s41550-021-01422-z.

M. J. Way, Anthony, and D. Del Genio. Venusian habitable climate scenarios: Modeling venus through time and applications to slowly rotating venus-like exoplanets. *Journal of Geophysical Research: Planets*, 125(5), May 2020. ISSN 2169-9097, 2169-9100. doi: 10.1029/2019JE006276. URL `http://arxiv.org/abs/2003.05704`.

D. Williams. Planetary fact sheets. can be found at: https://nssdc.gsfc.nasa.gov/planetary/planetfact.html, 2016.

R. G. Wilmoth, R. A. Mitcheltree, and J. N. Moss. Low density aerothermodynamics of the stardust sample return capsule. *Journal of Spacecraft and Rockets*, 1999.

C. F. Wilson, T. Widemann, and R. Ghail. Venus: key to understanding the evolution of terrestrial planets. *Experimental Astronomy*, Jun 2021. ISSN 0922-6435, 1572-9508. doi: 10.1007/s10686-021-09766-0. URL `https://link.springer.com/10.1007/s10686-021-09766-0`.

M. M. Woolfson. The Solar - Origin and Evolution. , 34, Mar. 1993.

M. Wright, I. Cozmuta, B. Laub, Y. K. Chen, and W. H. Wilcoxson. Defining ablative thermal protection system margins for planetary entry vehicles. In *42nd AIAA Thermophysics Conference*, Honolulu, Hawaii, Jun 2011. American Institute of Aeronautics and Astronautics. ISBN 978-1-62410-146-5. doi: 10.2514/6.2011-3757. URL `https://arc.aiaa.org/doi/10.2514/6.2011-3757`.

Appendix A

Runge-Kutta tableaus

Table A.1: Coefficients for the 8th order RK propagator (Cappellari et al., 1976).

i	a_i	b_{i1}	b_{i2}	b_{i3}	b_{i4}	b_{i5}	b_{i6}	b_{i7}	b_{i8}	b_{i9}	
1	0										
2	4/27	4/27									
3	2/9	1/18	3/18								
4	1/3	1/12	0	3/12							
5	1/2	1/8	0	0	3/8						
6	2/3	13/54	0	-27/54	42/54	8/54					
7	1/6	389/4320	0	-54/4320	966/4320	-824/4320	243/4320				
8	1	-231/20	0	81/20	-1164/20	656/20	-122/20	800/20			
9	5/6	-127/288	0	18/288	-678/288	456/288	-9/288	576/288	4/288		
10	1	1481/820	0	-81/820	7104/820	-3376/820	72/820	-5040/820	-60/820	720/820	
	A	c_1	c_2	c_3	c_4	c_5	c_6	c_7	c_8	c_9	
	1/840	41	0	0	27	272	27	216	0	216	41

Table A.2: Coefficients for the 5th order RK propagator (Dormand and Prince, 1980).

i	a_i	b_{i1}	b_{i2}	b_{i3}	b_{i4}	b_{i5}	b_{i6}	b_{i7}
1	0							
2	1/5	1/5						
3	3/10	3/40	9/40					
4	4/5	44/45	-56/15	32/9				
5	8/9	19372/6561	25360/2187	64448/6561	212/729			
6	1	9017/3168	355/33	46732/5247	49/176	5103/18656		
7	1	35/384	0	500/1113	125/192	2187/6784	11/84	
	A	c_1	c_2	c_3	c_4	c_5	c_6	c_7
	1	35/384	0	500/1113	125/192	2187/6784	11/84	0
	1	5179/57600	0	7571/16695	393/640	92097/339200	187/2100	1/40

Appendix B

Validation results

Table B.1: Maximum relative errors for different comparisons.

Simulation (step size)	Altitude	Fixed velocity	Inertial velocity	Acceleration
Only Newton (1 s)	1.7151e-13	2.3101e-8	4.9121e-13	3.4077e-13
Only Newton (0.1 s)	7.6522e-15	2.3101e-8	1.5130e-14	1.6675e-14
Newton + J2 (1 s)	6.6355e-10	2.5017e-8	1.9040e-9	5.6676e-9
Newton + J2 + External (1 s)	7.2353e-10	2.5198e-8	2.0866e-9	5.8427e-9
Atmospheric model				
Different atmosphere (1 s)	6.2209e-4	7.3712e-1	6.8564e-1	1.5063e-0
Ad-Hoc atmosphere (1 s)	8.6029e-5	3.0432e-2	6.3220e-3	2.1833e-2
Ad-Hoc atmosphere at each step (1 s)	8.3246e-5	4.7485e-2	1.8943e-2	1.8526e-2
Ad-Hoc atmosphere at each step (0.1 s)	8.4351e-5	4.8397e-2	1.9023e-2	1.8533e-2
Polar trajectories				
Newton + External + Atmosphere (1 s)	5.5971e-10	9.2604e-7	9.2604e-7	7.1953e-5
Newton + External + Atmosphere (0.01 s)	1.3896e-9	9.8900e-7	9.8900e-7	2.3246e-5
Dormand-Prince				
GMAT (1e-10) vs GMAT (0.01 s)	-2.4960e-8	-7.4168e-6	-7.4168e-6	4.6062e-5
GMAT (1e-10) vs code (1e-10)	-1.2079e-9	-1.7919e-7	-1.7919e-7	-4.6191e-5
GMAT (1e-10) vs code (1e-8)	-8.6095e-8	2.567e-05	2.5607e-5	-1.3106e-5
GMAT (1e-10) vs GMAT (1e-12)	3.2619e-9	6.3595e-7	6.3595e-7	5.9065e-6
Venus				
Only Newton (0.1 s)	1.7046e-12	3.5630e-14	3.5646e-14	3.4063-12
Newton + External (0.1 s)	1.5831e-12	3.0673e-11	3.0676e-11	1.6661e-10
Newton + J2 + External (0.1 s)	9.0248e-11	3.7105e-9	3.7119e-09	4.8580e-6

Appendix C

Parametric simulations results

Table C.1: Simulations' conditions.

N. Sim.	SF_{Vel}	$\frac{C_L}{C_D}$	$H_{\Delta C_L}$	$\frac{\beta_2}{\beta_1}$	$H_{\Delta B}$	N. Sim.	SF_{Vel}	$\frac{C_L}{C_D}$	$H_{\Delta C_L}$	$\frac{\beta_2}{\beta_1}$	$H_{\Delta B}$
1	1	0	0	0	0	15	1	0.5	250	2	100
2	1.01	0	0	0	0	16	1	0 / 0.5	105	2	105
3	0.99	0	0	0	0	17	1	0 / 0.5	105	2	100
4	1	0.3	250	0	0	18	1	0 / 0.5	100	2	105
5	1	0.5	250	0	0	19	1	0 / 0.5	100	2	100
6	1	0 / 0.5	105	0	0	20	1	0.3 / 0.6	105	2	100
7	1	0.5 / 0	105	0	0	21	1	0.5 / 1	105	2	100
8	1	0 / 0.5	100	0	0	22	1	0.3 / 0.6	105	2	95
9	1	0	0	2	Per.	23	1	0.5 / 1	105	2	95
10	1	0	0	2	105	24	1	0.3 / 0.6	105	3	95
11	1	0	0	2	100	25	1	0.5 / 1	105	3	95
12	1	0	0	5	105	26	0.99	0.3 / 0.6	105	3	95
13	1	0	0	10	105	27	0.99	0.5 / 1	105	3	95
14	1	0.5	250	2	105	28	1	0.5 / 0 / 0.5	105	2	95

Table C.2: Simulations' outputs for β 350 kg/m^2.

N. Sim.	Corridor [°]	Periapsis [km]	ΔV [km/s]	HL [MJ/m^2]	Peak $\dot{q}$ [kW/m^2]	Peak decel. [g]
1	-0.34 / -0.24	93.90 / 98.46	3.60 / 0.99	378.90 / 210.43	4801.31 / 3272.42	5.49 / 2.23
2	-0.42 / -0.34	94.45 / 97.96	3.02 / 1.11	347.86 / 227.63	4915.28 / 3575.81	5.14 / 2.44
3	-0.24 / -0.14	94.18 / 98.75	3.35 / 0.91	353.92 / 201.07	4496.82 / 3049.89	5.16 / 2.07
4	-0.6 / -0.28	91.82 / 98.21	3.13 / 0.87	273.55 / 184.96	6594.36 / 3405.07	9.64 / 2.25
5	-0.68 / -0.32	92.39 / 97.84	2.41 / 0.87	239.47 / 180.37	6709.28 / 3579.15	9.61 / 2.54
6	-0.68 / -0.32	92.30 / 97.20	2.45 / 1.01	243.33 / 204.59	6770.69 / 3928.30	9.81 / 3.03
7	-0.32 / -0.24	95.30 / 98.79	2.35 / 0.88	300.95 / 195.57	4300.17 / 3146.76	4.32 / 2.10
8	-0.64 / -0.28	92.42 / 97.83	2.40 / 0.88	246.30 / 190.64	6706.66 / 3578.13	9.58 / 2.55
9	-0.34 / -0.24	93.90 / 98.36	2.78 / 0.86	371.18 / 209.74	4801.12 / 3268.09	5.49 / 2.24
10	-0.4 / -0.28	91.37 / 96.72	3.54 / 0.81	553.19 / 272.80	7317.22 / 4358.78	5.44 / 1.87
11	-0.38 / -0.3	92.30 / 95.91	2.75 / 1.07	477.24 / 310.97	6690.30 / 4691.50	4.54 / 2.10
12	-0.44 / -0.36	89.91 / 93.53	1.97 / 0.83	747.77 / 472.35	11677.04 / 7868.98	3.54 / 1.78
13	/	/	/	/	/	/
14	-0.76 / -0.4	89.68 / 95.02	2.45 / 0.95	367.61 / 275.68	10671.07 / 5756.59	9.59 / 2.73
15	-0.76 / -0.4	89.77 / 95.32	2.44 / 0.94	364.40 / 270.30	10490.06 / 5420.87	9.34 / 2.52
16	-0.76 / -0.36	89.54 / 95.55	2.50 / 0.87	372.13 / 270.76	10783.80 /5258.01	9.90 / 2.35
17	-0.76 / -0.36	89.64 / 95.66	2.48 / 0.87	369.29 / 267.76	10571.10 /5089.80	9.60 / 2.28
18	-0.72 / -0.36	89.73 / 95.38	2.43 / 0.91	375.18 / 280.69	10614.42 /5389.39	9.48 / 2.48
19	-0.72 / -0.36	89.77 / 95.40	2.45 / 0.92	369.03 / 273.22	10387.21 /5311.75	9.36 / 2.44
20	-0.8 / -0.4	89.90 / 95.54	2.24 / 0.86	345.67 / 255.55	10547.82 / 5258.97	9.42 / 2.44
21	-0.88 / -0.48	90.94 / 95.24	1.59 / 0.80	291.21 / 231.41	10112.11 /5646.38	9.50 / 3.14
22	-0.88 / -0.32	89.83 / 98.01	2.36 / 0.81	330.94 / 172.50	9879.91 / 3537.01	9.47 / 2.48
23	-1.04 / -0.44	90.80 / 96.92	1.74 / 0.89	276.54 / 165.82	9485.68 / 4216.99	9.62 / 4.03
24	-0.88 / -0.32	89.14 / 97.98	2.18 / 0.81	404.45 / 173.43	10941.56 / 3547.82	7.63 / 2.48
25	-1.12 / -0.44	89.37 / 96.94	1.75 / 0.89	349.43 / 166.59	11821.94 /4221.33	9.08 / 4.05
26	-0.88 / -0.24	88.12 / 97.80	2.43 / 0.84	408.63 / 169.74	11899.23 /3451.72	9.25 / 2.58
27	-1.04 / -0.32	89.35 / 97.31	1.75 / 0.82	334.68 / 157.32	11003.37 / 3798.51	8.95 / 3.58
28	-0.38 / -0.26	92.48 / 97.91	3.00 / 1.11	446.28 / 217.91	5590.25 / 3401.93	5.70 / 2.43

Table C.3: Simulations' outputs for β 500 kg/m^2. *Simulation 25 has a gap at 0.56° and 27 at 0.36° - 0.4° because of too small ΔVs.

N. Sim.	Corridor [°]	Periapsis [km]	ΔV [km/s]	HL [MJ/m^2]	Peak $\dot{q}$ [kW/m^2]	Peak decel. [g]
1	-0.36 / -0.26	93.14 / 97.62	3.00 / 0.87	369.14 / 205.26	5179.34 / 3394.01	5.03 / 2.01
2	-0.46 / -0.36	92.77 / 97.14	3.39 / 0.98	399.75 / 230.55	5677.87 / 3801.23	5.52 / 2.26
3	-0.26 / -0.16	93.40 / 97.84	2.79 / 0.80	349.63 / 199.17	4765.72 / 3056.11	4.68 / 1.87
4	-0.64 / -0.32	90.39 / 96.68	3.18 / 0.93	305.41 / 206.58	7695.82 / 3922.36	9.97 / 2.38
5	-0.72 / -0.36	90.99 / 96.41	2.43 / 0.92	266.30 / 196.91	7866.25 / 4119.82	9.82 / 2.63
6	-0.68 / -0.32	91.22 / 96.81	2.35 / 0.83	271.28 / 203.82	7679.91 / 3913.96	9.29 / 2.39
7	-0.36 / -0.28	93.46 / 97.05	2.75 / 1.02	346.40 / 221.59	5075.84 / 3638.28	4.77 / 2.28
8	-0.68 / -0.32	91.11 / 96.54	2.39 / 0.89	273.48 / 210.82	7758.05 / 4055.79	9.54 / 2.55
9	-0.38 / -0.28	92.18 / 96.76	3.13 / 0.90	420.91 / 236.58	5504.56 / 3720.22	5.93 / 2.41
10	-0.4 / -0.32	91.57 / 95.20	2.22 / 0.90	501.62 / 326.07	7721.05 / 5284.75	4.02 / 1.95
11	-0.42 / -0.34	90.60 / 94.20	2.97 / 1.15	562.19 / 353.98	8154.52 / 5702.02	4.81 / 2.32
12	-0.42 / -0.4	90.86 / 91.76	1.09 / 0.85	648.29 / 585.70	11547.99 / 10248.54	2.28 / 1.90
13	/	/	/	/	/	/
14	-0.68 / -0.4	89.49 / 94.44	2.04 / 0.81	415.29 / 293.08	11645.51 / 6094.60	7.27 / 2.22
15	-0.72 / -0.4	89.11 / 94.63	2.18 / 0.81	417.09 / 282.77	11939.40 / 5824.38	7.95 / 2.13
16	-0.68 / -0.4	89.37 / 94.24	2.09 / 0.86	416.24 / 304.74	11711.41 / 6195.92	7.54 / 2.32
17	-0.68 / -0.4	89.33 / 94.49	2.11 / 0.84	420.67 / 295.58	11675.31 / 5920.97	7.58 / 2.21
18	-0.68 / -0.4	89.27 / 93.89	2.13 / 0.91	422.64 / 317.70	11829.44 / 6498.27	7.73 / 2.51
19	-0.68 / -0.4	89.18 / 94.02	2.18 / 0.92	422.51 / 309.05	11576.15 / 6261.31	7.82 / 2.41
20	-0.72 / -0.44	89.64 / 93.96	1.89 / 0.89	392.15 / 292.60	11622.12 /6358.72	7.42 / 2.52
21	-0.84 / -0.52	90.11 / 93.68	1.47 / 0.82	336.76 / 266.79	11919.67 /6921.53	8.12 / 3.27
22	-0.84 / -0.36	89.01 / 96.61	2.17 / 0.84	378.87 / 189.66	11291.89 /4039.73	8.40 / 2.58
23	-1.04 / -0.44	89.38 / 96.16	1.71 / 0.81	329.64 / 174.58	11855.88 /4397.73	9.63 / 3.38
24	-0.72 / -0.36	89.46 / 96.60	1.65 / 0.84	452.01 / 186.87	11683.60 /4051.36	5.19 / 2.57
25*	-0.88 / -0.4	89.83 / 96.77	1.34 / 0.72	384.06 / 168.97	11812.64 / 4 071.98	5.98 / 2.92
26	-0.64 / -0.24	89.29 / 97.25	1.68 / 0.73	435.35 / 171.28	10890.82 /3491.76	5.26 / 2.17
27*	-0.84 / -0.32	89.36 / 96.56	1.42 / 0.74	376.31 / 162.45	11634.61 / 3915.58	6.37 / 3.00
28	-0.42 / -0.3	90.74 / 96.16	3.04 / 1.29	523.10 / 245.58	7138.75 / 3989.50	4.61 / 2.68